



**Politecnico
di Torino**

POLITECNICO DI TORINO

Master's Degree in Biomedical Engineering

Master's Degree Thesis

Development of a microfluidic alveolus-on-chip supporting epithelial-endothelial cells co-culture and air-liquid interface implementation for the modelling of the physiological alveolar-capillary barrier

Supervisors:

Matteo Cocuzza
Gianluca Ciardelli
Simone Marasso
Chiara Tonda Turo

Candidate:

Martina Cicolini
277404

Ay 2021/2022

Table of contents

List of figures

Abstract

1. Introduction	11
1.1 The human respiratory system	11
1.2 Lung models	16
1.3 Alveolus-on-chip: background works	39
2. Aim of the work	43
3. Materials and methods	45
3.1 3D printing	45
3.2 Replica molding	51
3.3 Electrospinning	52
3.4 Device assembling	56
3.5 Cell culture	57
4. Results and discussion	65
4.1 Design-experiment cycle: the iterative process towards the final device	65
4.2 Tesla valve-design validation	73
5. Conclusions	79
6. Appendix	83
7. Bibliography	89

List of figures

Figure 1. Left: SEM image of the human alveolar barrier and TEM image of alveolar epithelium (EP), capillary endothelium (EN), basement membranes (BM) [4]. Right: cell types constituting the alveolar-capillary membrane. AT I cell: alveolar epithelial type I cell. AT II cell: alveolar epithelial type II cell [10].	12
Figure 2. Percentage of type II alveolar epithelial cells (ATII) that respond to stretch under monoculture (ATII) or co-culture conditions (ATII (+ wt) or ATII (+ cav ^{-/-})). [9]	14
Figure 3. Alveolar level changes in the lung caused by SARS-CoV-2 infection. [7]	16
Figure 4. Left: number of animals used for scientific purposes in the EU in 2017. Right: number of animals used for scientific purposes in the EU by species in 2017. [18]	19
Figure 5. Lung model up to the 16th generation: blue color part obtained from CT, yellow color representing the ideal part. [25]	21
Figure 6. Human airway epithelial cells (hAECs) culture protocol for implementation of air–liquid interface (ALI). Figure created with BioRender.com (accessed on 28 April 2021). [27]	23
Figure 7. Comparison of qRT-PCR assay transcripts of key genes of interest in A549 cell air-liquid interface (ALI) cultures. [28]	23
Figure 8. Electrical resistance (left) and FITC-dextran permeability assays (right) performed on inserts with poly(trimethylene carbonate) (M3) or poly(ethylene terephthalate) (PET) membranes containing either no cells, Calu-3 cells, LMVECs, or co-cultures. Capped lines depict significant differences, P < 0.05. [30]	24
Figure 9. Efficacy and toxicity curves for imatinib and MPA in organoids after the infection with a vesicular stomatitis ΔG-luciferase virus pseudotyped with the SARS-CoV-2 spike protein (SARS-CoV-2-entry virus). [35]	27
Figure 10. a) Schematic representation of preparation of porous PLGA microspheres [38]. b) SEM image of porous PLGA microspheres based on ratio of porogen (mg) to PLGA (mg) used in the formulation 6:50 [41].	29
Figure 11. Comparative in vitro screening of anti-cancer drugs on monolayers and scaffold-based co-cultures. Significance was analyzed by Student’s t-test (*p < 0.001, #p < 0.01). [41]	30
Figure 12. Confocal laser scanning microscopy images of the alveolar–capillary barrier established on 2 μm PCL nanofibrous meshes and control (PET membranes) and their cross-sections (C, F). In red, endothelial cell-specific marker (CD31-red), in green, epithelial adherens junction (E-cadherin-green), in blue, cell nucleus (DAPI-blue). Scale bar: 50 μm. [40]	32
Figure 13. Illustration and photograph of the modular multi-tissue organ-on-a-chip hardware system. (d) Lung models consist in layers of cells over porous membranes within microfluidic devices. TEER (trans-endothelial	

[or epithelial] electrical resistance) sensors allow monitoring of tissue barrier function integrity over time. [47].....	37
Figure 14. (c–e) Cardiac organoid beating plots on day 9. (h,i) Assessment of inflammatory factors following bleomycin administration on day 3. (j) IL-1 β effect on beating rate. [47]	38
Figure 15. The human alveolus chip is exposed to SARS-CoV2 on the epithelial layer (blue), and human immune cells are infused into the bottom vascular channel (red) during the progression of virus infection. [48].....	39
Figure 16. Selective etching of the membrane in the channels produces two side chambers for the application of vacuum that causes mechanical stretching of the central PDMS membrane (scale bar, 200 μ m). (E) View from above of a lung-on-a-chip. [50]	40
Figure 17. Fabrication steps of honeycomb microframe. [51]	41
Figure 18. On the left. (a-d) Scanning electron microscopy (SEM) images of 24 honeycomb microframes and of a suspended monolayer of gelatin electrospun nanofibers. On the right. The chip allows the application of air pressure from apical channels and liquid flow from basal channels. [51]	41
Figure 19. Laplace’s equation for the calculation of the displacement of the monolayer at the air-liquid interface. γ is the liquid surface tension equal to 72.8 mN/m for water, and R1 and R2 are the two principal radii of curvature. [51].....	42
Figure 20. On the left, top view (a) and front view (b) of the CAD model of the master of the bottom layer. On the right, front view (c) and perspective view (d) of the CAD model of the master of the plug for the conic inlets. Dimensions are expressed in millimeters.	46
Figure 21. Top view (a) and perspective view (b) of the CAD model of the top layer master. Dimensions are expressed in millimeters.....	48
Figure 22. On the left, top view (a) and perspective view (b) of the CAD model of the reservoir master. On the right, front view (c) and perspective view (d) of the CAD model of the master of the plug for the central upper hole. Dimensions are expressed in millimeters.....	49
Figure 23. ChiLab OBJET30 Stratasys 3D printer.	50
Figure 24. Free monomers and photo-initiator molecules inhibit the curing of PDMS; UV and thermal treatments of the molds avoid the interaction of these molecules with the catalyst [61].	51
Figure 25. Chemical structure of polydimethylsiloxane	52
Figure 26. Influence of solution and process parameters on the morphology of the electrospun fibers [68].	53
Figure 27. Novaspider V5 elettrospinning instrument in Polito ^{BIO} Med Lab.	54
Figure 28. Chemical structure of (3-Glycidyloxypropyl) trimethoxysilane (GPTMS).....	55
Figure 29. ChiLab Atto plasma system by Diener electronic.	57
Figure 30. Timeline for the cell seeding and co-culture experiments. Created with BioRender.com	60

Figure 31. Time points for the cell fixation for the evaluation of the optimal co-culture protocol. Created with BioRender.com	60
Figure 32. Chemical structure of (a) FITC-phalloidin and (b) DAPI.....	61
Figure 33. The work cycle, from design to cells experiments, whose reiteration led to the final device configuration. Created in BioRender.com.....	65
Figure 34. CAD model (a), detail of the culture chamber of the 3D-printed mold (b) and the resulting replica (c, d) of the first design of the bottom layer realized in this work, whose lack of functional pillars led to dimensional modifications.	66
Figure 35. Section of the microfluidic serpentine of a PDMS replica obtained from a mold of the first design, having nominal dimensions of width, height and reciprocal distance of 500 μm	67
Figure 36. Staining with DAPI of HULEC-5a. Evaluation of cell adhesion on the electrospun membrane 4 hours after seeding, using two different seeding approaches. a) Seeding performed introducing 100 μL of cell suspension in the microfluidic channels through the lateral inlet. b) Seeding performed introducing 10 μL of cell suspension in the culture chamber through the central inlet directing accessing the membrane.....	69
Figure 37. a, b) Section of complete PDMS devices in correspondence to their culture chamber and suspended membrane, in absence (a) and presence (b) of support pillars, after a microfluidic test with blue food dye. c, d) One of the devices subjected to the microfluidic test, before (a) and after (b) the 24 hours incubation..	70
Figure 38. Confocal laser scanning images of HULEC-5a (A-F) and A549 (G-I), in one-serpentine-device, after fixation and staining with DAPI (A, D, G) and phalloidin (B, E, H). The images of both color channels and their merge (C, F, I) is shown. Scale bar is 20 μm	72
Figure 39. a) Section of the bottom layer replica in correspondence to its culture chamber, showing two of the four support pillars. b Section of the bottom layer replica in correspondence to the microfluidic serpentine, having nominal dimensions of 600 μm width, 600 μm height and reciprocal distance of 700 μm	73
Figure 40. On the left: evaluation of the quality of the plasma-bonding between bottom and top layer, using a micropipette and food dye diluted in water. On the right: a complete device (bottom, top and reservoir layers) with its sealing plugs inserted in the inlets, before (upper image) and after (lower image) a 24 hours incubation with cell medium, in an oven at 37°C.....	74
Figure 41. SEM images of a sample of membrane treated at 70°C for 10 minutes after the plasma-bonding.	74
Figure 42. Confocal laser scanning images of HULEC-5a (A-F), in Tesla valve-devices, after fixation and staining with DAPI (A, D) and phalloidin (B, E). The images of both color channels and their merge (C, F) are shown. Scale bar is 20 μm	75

Figure 43. Confocal laser scanning images of A549 (A-F), in Tesla valve-devices, after fixation and staining with DAPI (A, D) and phalloidin (B, E). The images of both color channels and their merge (C, F) are shown. Scale bar is 20 μm 76

Figure 44. Comparison between apparent permeability (cm/s) of A549 cells and HULEC-5a cells co-cultures and PCL/Gel (no cells) after 7 days at ALI..... 77

Figure 45. Immunofluorescence staining for E-cadherin in A549 cells (a) and ZO-1 in A549 cells (b) and in HULEC-5a after (c) 7 days at ALI in co-culture. Scale bar is 20 μm 78

Abstract

The respiratory system, being the largest interface with the external environment, is constantly exposed to harmful substances reaching the lungs by inhalation, other than via the blood stream. The alveolar-capillary barrier, that constitutes the functional interface between air and blood and mediates the gas exchange in the lung, plays a fundamental role in the defence against pathogens and xenobiotics. Diseases associated with alveolar-capillary barrier dysfunction include asthma, idiopathic pulmonary fibrosis (IPF) and Coronavirus disease 2019 (COVID-19), caused by the RNA virus SARS-CoV-2: studying the role of alveolar-capillary barrier in pulmonary homeostasis may help to understand the pathophysiology of diseases and to discover new therapeutic targets. In this respect, in vitro models are useful alternatives to animal models, that present limiting species-specific differences in organogenesis, tissue organization and susceptibility to diseases, to study the mechanisms underlying the functions of a tissue and to develop personalized treatments for different pathological conditions. Organ-on-Chip are high-throughput in vitro models that strive to mimic the architecture, functionality, and mechanical and chemical cues of the physiological environment at a miniaturized scale, processing microscale fluids in channels that range in size from tens to hundreds of microns. The aim of the present work was the realization of an alveolus-on-chip that would face the challenge of developing a device able to support both the presence of an air-liquid interface (ALI) in the apical compartment of the device and the implementation of a mechanical stimulation of the barrier model, that would recapitulate the effects of the breathing motion on the physiological tissue. The device consists of a polydimethylsiloxane (PDMS) microfluidic platform able to embed a nanofibrous scaffold, hosting an alveolar-capillary barrier model. The model is a co-culture of epithelial (A549 cell line) and human lung microvascular endothelial cells (HULEC-5a) on the two sides of an electrospun bioartificial membrane, mimicking the human alveolar wall. Each of the three PDMS layers of the device was designed using the software Rhinoceros and fabricated using the replica molding technique, by casting PDMS in 3D printed molds obtained with a Poly-Jet 3D printer. The nanofibrous scaffold was fabricated electrospinning a blend solution of polycaprolactone (PCL) and gelatin, and its morphology was analysed through scanning electron microscopy. The cellular adhesion on the two sides of the electrospun membrane was evaluated performing the

staining of the nuclei, with DAPI, and the actin filaments, with phalloidin, of A549 and HULEC-5a at different time points, before and after the implementation of the ALI condition. Immunostaining and permeability tests were performed to evaluate the barrier function of the model. At seven days after air-liquid interface implementation, the epithelial layer appears confluent and homogeneous over the nanofibrous membrane. The endothelial cells reach confluence as well and show a spread cytoskeleton. Results suggest that the design of the PDMS bottom layer impacts on the ability of the endothelial cells to reach confluence and long-term viability. The pattern of each component was therefore optimized to minimize the impact on cell migration and not to obstruct medium passage, crucial for cells survival.

1. Introduction

1.1 The human respiratory system

The process of respiration serves the purpose of supplying cells with oxygen, needed for aerobic cellular respiration, thanks to inhalation, and removing the carbon dioxide produced by cells, along with xenobiotics, through exhalation. The vehicle transporting the gases in every tissue of the body is blood, whose pH is also maintained thanks to respiration [1].

The respiratory system can be divided in two functional zones: the conducting zone, from the nose to the bronchioles, that allow the conduction of inhaled and exhaled gases, and the respiratory zone, including the lungs and its respiratory bronchioles, alveolar ducts and alveoli, where the gas exchange across the alveolar-capillary barrier takes place [1].

1.1.1 The functional unit of the lung

The larynx transmits air from oropharynx and nasopharynx to trachea. The trachea then divides into the two primary bronchi, that branch out, in their turn, into five secondary lobar bronchi: three of them enter the right lung, the other two the left lung. The ramification of the conducting pipes continues in the lungs, where the lobar bronchi generate the bronchioles, which are in turn divided into progressively smaller airways. The 16th generation gives rise to the acinus, the actual gas exchange unit of the lung. In the acinus, the distal ends of alveolar ducts open into the alveolar sac, which is made up by alveoli, each having a diameter of 200-300 μm and surrounded by capillaries [1].

1.1.2 The alveolar-capillary barrier

The gas exchange in the alveolar sac is made efficient by the combination of a large surface of contact between air and blood (the total surface area of the alveoli can reach 150 m^2) and an extremely thin barrier (less than 1 μm) that allows the rapid diffusion of gases while physically protecting the tissues from atmospheric dangerous substances [2]. The flat thin epithelial layer is guaranteed by the morphological characteristics of alveolar epithelial cells and by their compression during inhalation.

In particular, the mature alveolar epithelium consists of type I and type II alveolar epithelial cells (AECIs and AECIIs, also called type I and type II pneumocytes), which occupy about 96% and 4% respectively of the surface [3]. AECIs, which are membranous flat cells, provide the thin surface of the alveolus; AECIIs are large cuboidal cells located in the alveolar corners able to pre-pack the surfactant in the lamellar bodies, until their secretion into the airspaces. The surfactant, a complex mixture of lipids (90%) and proteins (10%), contributes to the alveolar stability during breathing [3]. The transepithelial paracellular passage of molecules between the alveolar space and the interstitium compartment, containing fibroblasts, is controlled by tight junctions, multiprotein complexes that ensure the barrier integrity, while various pumps and channels regulate the flux of fluid, allowing the epithelial continuum to maintain the air interface [3].

A basement membrane composed by fibrils of type IV collagen and elastin, with a thickness of about 50 nm, supports the thin alveolar membranes and protects against cell damage, while dividing the luminal epithelium from the capillary endothelial cells that form the vascular network surrounding the alveoli [4].

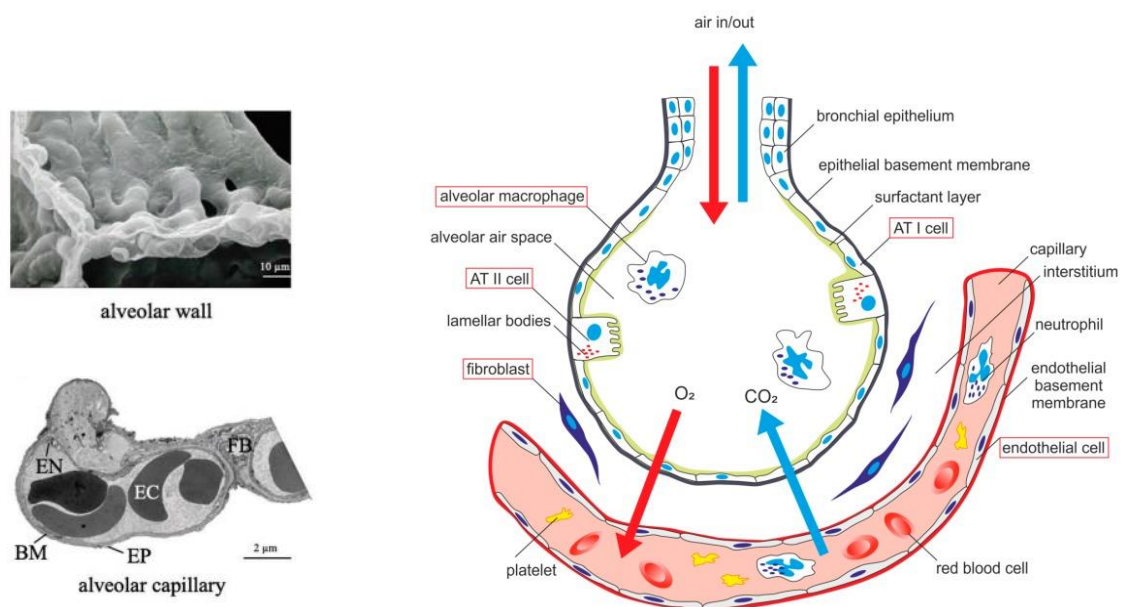


Figure 1. Left: SEM image of the human alveolar barrier and TEM image of alveolar epithelium (EP), capillary endothelium (EN), basement membranes (BM) [4]. Right: cell types constituting the alveolar-capillary membrane. AT I cell: alveolar epithelial type I cell. AT II cell: alveolar epithelial type II cell [10].

A negative pressure system and the contraction of muscles are involved in pulmonary ventilation. The internal pressure of lungs at rest, that is slightly lower than that of the atmosphere, allows air to follow the pressure gradient and passively fill the lungs [5]. Inhalation happens when the internal pressure matches the atmospheric pressure, and the contraction of the diaphragm that forms the floor of the thorax allows the expansion of the thoracic cavity, pulling air into the lungs. Relaxation of the diaphragm and contraction of the internal intercostal muscles reduce the volume of the thorax: the pressure gradient is reversed, resulting in the exhalation of air until the internal and atmospheric pressures are equal. At this point, the lungs recoil back to their resting volume, restoring the negative pressure gradient present before inhalation [5].

Pulmonary ventilation consequently implies the cyclic compression of the alveolar epithelium by the inhaled air, with a tidal volume of about 500 mL and a frequency of 0.2 Hz. The expansion of the lungs and the compression of the epithelium results in the stretching of the basement membrane, that must withstand a linear strain of about 4% (about 12% during a physical effort, up to 20% in an unhealthy lung) [4]. This is made possible by the surfactant system and by the properties of the membrane, consisting of a network of elastin and collagen fibers, that together ensure the mechanical stability of the alveolus [6]. In particular, the surfactant lowers the surface tension and the collapsing pressure on the epithelium. The elastin fibers exhibit linear elastic stress-strain relationship and can deform up to two times in length: they are responsible for the elastic recoil of the lung. Unlike elastin, collagen fibers show a nonlinear elastic stress-strain relationship: at lower volumes of inhaled air, the fibers appear crimped in a heterogeneous network, but at higher volumes the fibers stretch out limiting the expansion (apparent tissue stiffening) [7]. The Young's elastic modulus of a healthy alveolar tissue is about 1-2 kPa, but it can reach 16.5 kPa in a pathological condition, as in the case of idiopathic pulmonary fibrosis (IPF) [4].

1.1.4 The influence of mechanical stimuli on cells

Mechanical stretch has been shown to modify cell proliferation, differentiation, surfactant secretion, and migration through regulation of specific signalling pathways [4]. Mechanoreceptor proteins, such as stretch activated (SA) channel, integrin proteins and the platelet endothelial cell adhesion molecule-1 (PECAM), allow the

mechanotransduction, that is the detection of the stretching stimulus and its translation into changes in gene expression and protein synthesis, thanks to biochemical signals' cascades in the cells. Mechanical stimuli may therefore promote processes such as angiogenesis, proliferation, inflammation, apoptosis, vascular tone and cell survival [4].

Stretch applied to endothelial cells induces the formation of bundles of actin filaments, known as stress fibers, which contribute to resistance against the applied stress and transmit mechanotransduction in non-muscle cells [8]. The applied stimulus also determines extracellular matrix (ECM) remodelling, stimulates the secretion of angiogenic factors, and causes changes in cell's structure and morphology, determined by the cytoskeleton and focal adhesion complexes: cells become elongated and oriented perpendicularly to the stretch direction, which minimizes the tension endured by the cell [8].

The expansion of alveoli is also the strongest stimulus for surfactant secretion [9].

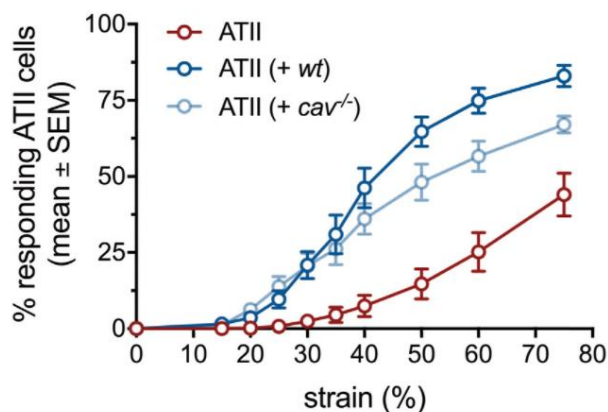


Figure 2. Percentage of type II alveolar epithelial cells (ATII) that respond to stretch under monoculture (ATII) or co-culture conditions (ATII (+ wt) or ATII (+ cav^{-/-})). [9]

To prove that, it has been demonstrated that the stretch of AECIs triggers strain-induced Ca²⁺-entry, and the resulting rise in intracellular Ca²⁺ levels is transmitted to AECIIs via gap junctions (figure 2). AECIIs consequently respond with lamellar bodies exocytosis and surfactant secretion: this means that AECIs can act as mechanosensors in the alveoli and stimulate surfactant secretion from AECIIs in a paracrine way [9].

1.1.5 Pathological conditions

The respiratory system, being the largest interface with the external environment, is constantly exposed to harmful substances (e.g., chemical pollutants, viruses) entering the lungs by inhalation, other than via the blood stream. For this reason, in order to maintain pulmonary homeostasis, along with the mucus-secreting goblet cells and the ciliated cells involved in the mucociliary escalator mechanism in the conducting tract, the alveolar-capillary barrier must contribute as well to the defence against pathogens. For example, the alveolar epithelium, together with the local alveolar macrophages, actively participates in the transmigration of neutrophils within the lung, supporting the process of phagocytes' migration toward the site of inflammation [3].

Diseases associated with alveolar epithelium dysfunction include asthma and idiopathic pulmonary fibrosis (IPF), which seem to be related to AEC dysfunction, abnormal repair capacity and fibrosis. AECs from fibrotic lung show deregulated cellular pathways, including altered expression of tight junction and adherens junction proteins such as claudins and β -catenin [3]. The barrier integrity is also dependent on the state of the surfactant: altered surfactant metabolism, resulting from genetic disorders and from environmental stressors, can lead to direct lung injury, after toxic inhalation, bacterial and viral infection, aspiration, indirect lung injury (sepsis, haemorrhage)[3].

The barrier function is influenced by capillary permeability as well. Inflammatory factors (e.g., histamine or platelet activating factor) increase endothelial permeability and allow substances like plasma proteins to enter alveoli: an increased capillary permeability is one of the major pathological characteristics of acute lung injury [10].

Coronavirus disease 2019 (COVID-19) is caused by the RNA virus SARS-CoV-2. It is a systemic disease associated with vascular inflammation and endothelial injury, where severe forms of infection induce acute respiratory distress syndrome (ARDS) [11]. Once it reaches the alveoli of the lung, the SARS-CoV-2 virus is able to directly infect the type I and type II alveolar epithelial cells through the angiotensin converting enzyme 2 (ACE2) receptor. Infection leads to cell death, with loss of the epithelial layer, diffused alveolar and capillary damage that causes fluid accumulation and intra-alveolar hemorrhage [7]. These microlevel alterations, together with surfactant dysfunction, lung inflammation, and focal fibrotic remodeling, act as stress concentrators, which are areas of focal lung

injury that can cause excessive mechanical loading in the surrounding tissues, potentially contributing to further injury progression [7].

In inflammatory states such as chronic obstructive pulmonary disease (COPD), the lung microenvironment displays features that may support carcinogenesis [12]. Also, local pre-existing inflammation in the lung caused by exposure to cigarette smoke may contribute to increased metastasis from extrathoracic malignancies, including breast, skin and colon cancer, which secrete factors and extracellular vesicles that systemically reprogramme the lung microenvironment to generate pre-metastatic niches [12].

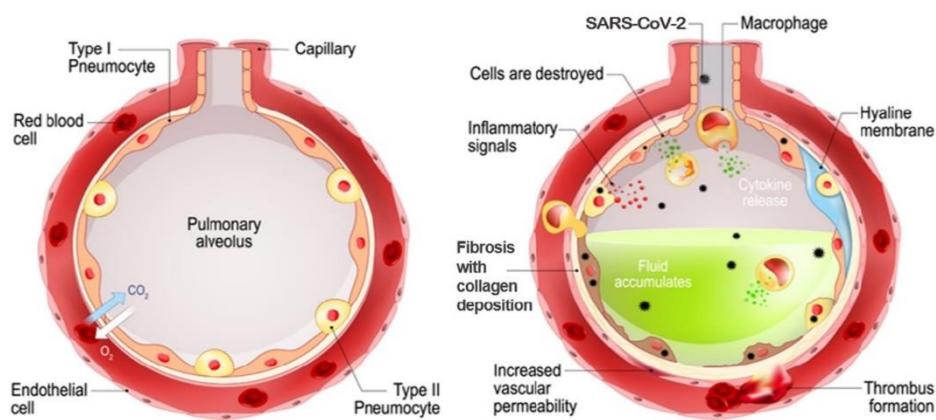


Figure 3. Alveolar level changes in the lung caused by SARS-CoV-2 infection. [7]

1.2 Lung models

The following sections will be dedicated to a comparison between the main types of models used in biomedical research, with a focus on lung and alveolar-capillary barrier models.

Since a model always approximates reality, the aim of the research is to look for the best possible approximation, in order to mimic the human system in a way as faithful as possible, to study the mechanisms underlying the functions of a tissue or organ and the pathophysiology of a disease, and to discover new therapeutic targets and the consequences of treatments.

Ultimately, different models may be used in a synergic way in different stages of a study, in order to fill each other's gaps and weaknesses, by optimizing the research process.

1.2.1 Animal models

Animal species are selected as models according to their degree of resemblance with humans' physiology and pathophysiology, their response on certain substances and their ability to reproduce the disease or condition that is examined, but also depending on their size and availability [13].

Mouse is mostly chosen as a model system because it represents the species with the lowest possible position in the evolutionary scale while still being compatible with a good degree of similarity with the human species (figure 4): the protein-coding regions of the mouse and human genomes are about 90% identical and 98% of human genes have a mouse homologue derived from a common ancestral gene [14]. In particular, genetically modified mice are widely used because they allow to evaluate the physiological function of specific genes and have therefore been used extensively in the study of inflammatory processes in the lungs [15].

For example, SARS-CoV-2 binds to alveolar epithelial cells thanks to the interaction of the viral spike protein with human angiotensin-converting enzyme 2 (hACE2), but the mouse ortholog of ACE2 is incompatible with the spike protein of the virus: for this reason, typical inbred mouse strains do not support viral replication. Since pre-clinical vaccines, anti-viral and therapeutic monoclonal antibody testing are usually performed in mice, due to the availability of reagents for immunological studies, this genetic limitation requires heterologous expression of human ACE2 in mice [16]. Mouse models for human ACE2 expression have been developed, including transgenic strains, with hACE2 expression under the control of human promoters, knock-in strains, using CRISPR/Cas9 knocking technology [17], and viral vector-mediated delivery of hACE2 using adeno-associated virus or adenovirus [16].

1.2.1.1 The 3Rs' principles

The directive 86/609/EEC, formally applied across the European Union on 1 January 2013, is the EU legislation "on the protection of animals used for scientific purposes", and its measures epitomize the principles defined for the first time by Russell and Burch in 1959, which are today named "the 3Rs' principles": they are refinement, reduction, and replacement.

Refinement

One of the main advantages in the use of animal models is represented by the possibility of performing tests on complex biological systems, where the effects of a drug or other kinds of treatments can be seen on a systemic level as well as in the target tissue. However, the complexity of *in vivo* models is also an experimental concern: the higher the number of variables in the system, the most difficult to isolate the results owed to the human tests. Therefore, housing the animals in a controlled and clean environment, using appropriate anaesthesia and analgesia to minimise pain, and training animals to cooperate with procedures to minimise any distress is needed in order to obtain reproducible and reliable testing conditions, since stress levels and suffering can alter animals' behaviour, physiology and immunology affecting the experimental outcomes [14], [17]. Together with the ethical urge of reducing the pain endured by the animals, these are the reasons behind the need for the refinement of the animal welfare. An example of the application of this principle could be the measure by radio-operated implants of blood pressure, heart rate and activity levels, so that animals do not have to be repeatedly caught or restrained [17].

Reduction

Reduction means using fewer animals to obtain the same – or more – research information [18]. Improving animal welfare positively reflects on the number of needed animals for each experiment. Inbred animals kept in clean environments get fewer secondary infections or illnesses, which might interfere with studies and require the repetition of the experiment. Good experimental design, correct choice of the model and statistical analysis ensure that researchers use the optimum number of animals. In fact, reduction must be compatible with the need for statistical significance of the data: otherwise, the experiment wouldn't be robust enough and the animal lives would be wasted.

Lung ultrasound, for instance, may reduce the number of experimental small animal models of pulmonary edema, due to the possibility of serial evaluations in the same animal as compared with traditional end-point measurements [19].

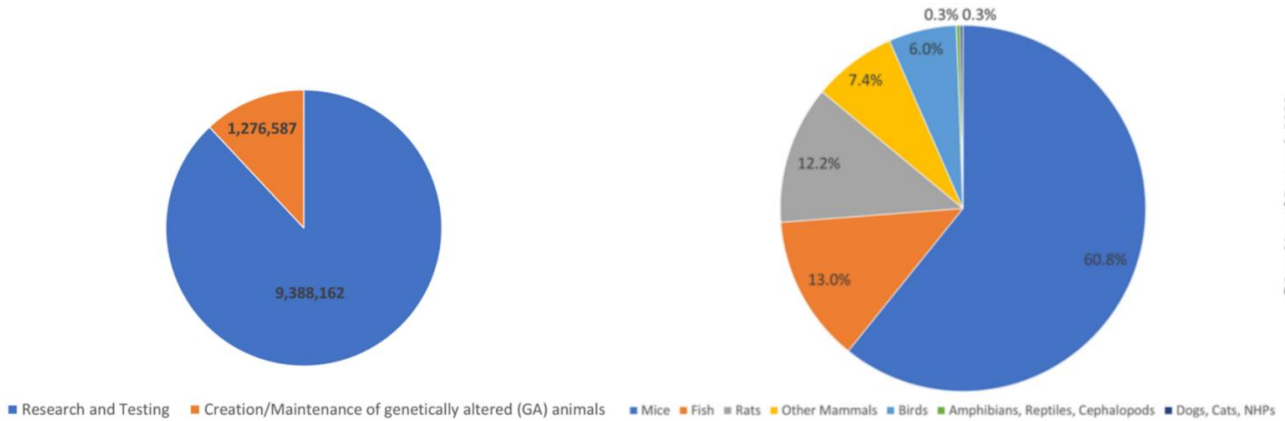


Figure 4. Left: number of animals used for scientific purposes in the EU in 2017. Right: number of animals used for scientific purposes in the EU by species in 2017. [18]

Replacement

Full replacement of animal models includes the use of human volunteers, tissues and cells, mathematical and computer models, and established cell lines. *Partial replacement* involves the use of animals that, based on current scientific thinking, are not considered capable of experiencing suffering: this includes invertebrates such as *Drosophila*, nematode worms and social amoebae, and immature forms of vertebrates [14].

1.2.1.2 Animal models' limitations

Despite animals' relevant role in biomedical research, there still are limiting species-specific differences in organogenesis, tissue organization and susceptibility to diseases. For instance, while it is known that in conditions of adult lung homeostasis, cell turnover is normally very low and the existing airway progenitor cells are quiescent in humans, numerous animal studies on mice have shown that progenitor cells have the capacity to proliferate and differentiate into one or more cell types in response to injuries such as exposure to infectious agents, tobacco smoke, high levels of oxygen and the chemotherapy drug bleomycin [20], [21]. This led to the research for drugs able to activate progenitor cells *in vivo* or establish cell-based therapies for the treatment of

patients suffering from respiratory disease arising from lung injury or ageing [21]. However, the poor results obtained in humans are probably due to unknown differences in lung anatomy and physiology between mice and humans.

Overall, non-animal models have the potential to provide powerful, scalable screening platforms to test pharmaceuticals. Their use in preclinical trials may allow to reduce costs and failure rate of drug testing in rodent models that usually precedes human clinical trials [22].

1.2.2 *In silico* models

In silico medicine, or ‘computational medicine’, can be defined as the use of modelling and simulation technologies to directly contribute to the prevention, diagnosis, prognosis, and treatment planning of diseases [23]. Computational methods can provide subject-specific predictions of physical quantities that are difficult or impossible to measure directly, but which are relevant for the comprehension of the functioning of an organ or the progression of a disease. Modelling and simulation can also facilitate biomedical devices development and design optimization, supplement testing, support post-market design changes and failure assessment: the term “*in silico* trials” refers to the use of modelling and simulation in both the preclinical and clinical evaluation of a new medical product [23].

As far as the acinar region is concerned, its complex, micrometric and inaccessible geometry makes it difficult to study in a detailed way the fluid-particle dynamics *in vivo*. Nevertheless, the prediction of airflow and particle deposition in the alveolar region is necessary to understand the outbreak of pulmonary diseases caused by inhaled toxic aerosols and to perform therapeutic drug targeting of the lungs [24].

In order to address these issues, Kolanjiyil *et al.* recently simulated the alveolar fluid flow by solving the 3D Navier–Stokes equations on a moving mesh using an unsteady incompressible laminar flow solver [24]. The aim of the work was to develop a model of the acini to analyse particle and aerosols deposition in the alveoli, whose expansion and contraction were also simulated according to different breathing modes [24]. A single alveolus was modeled as a partial spheroid, with a neck assembled on the surface of a cylindrical duct. Four parameters were used to describe the alveoli: alveolus radius, neck

radius, alveolus depth, and the duct diameter. The non-linear behaviour of the alveolar tissue and the presence of surfactant, limiting the stretching of the alveolar walls after an initial expansion, were simulated as well by assuming that after 500 ml of tidal volume the expansion rate was reduced to half due to strain-stiffening of the biological tissue [24].

In a different study, Agujetas *et al.* developed a methodology for the creation of hybrid pulmonary geometries [25]. Computed Tomography lung images were exported to the DICOM format to be treated with a commercial software to build the patient-specific part of the model [25]. The distal terminus of each airway of this portion was extended with an idealized airway, with an intermediate solid to link the two parts together (figure 5). The results of the simulations showed that the hybrid model, combining real and idealized pulmonary models, can provide a realistic description of air flow dynamics in the lung while reducing computational costs compared to models of the full airway tree [25]. The reduction of costs also applies to the economic field: treatment of respiratory diseases, which account for one in twelve deaths in Europe, is a substantial component of health care expenses. Computational simulations of lung airflow may contribute to cost reduction and improved outcomes [25].

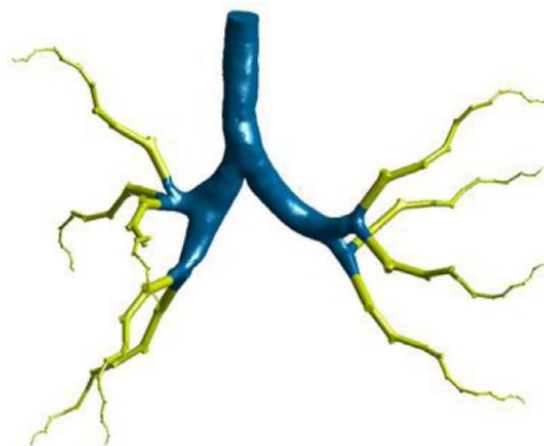


Figure 5. Lung model up to the 16th generation: blue color part obtained from CT, yellow color representing the ideal part. [25]

Developing *in silico* technologies in order to apply the 3Rs' principles in preclinical and clinical experimentation still requires the overcoming of barriers, like the needed technological knowledge and the issue of the reliability. The EU therefore sponsored the

'Avicenna Alliance', a global non-profit organization whose goal is the definition of a roadmap for clinical trials based on computational models. The most urgent gaps to fill pointed out by the initiative are the introduction of modelling and simulation in the regulatory process and the harmonization of the operating procedures in the industrial sector [26].

1.2.3 *In vitro* models

In vitro models include cell monolayers, co-cultures, tri-dimensional spheroids and organoids, microfluidic devices, and systems involving artificial or bioartificial materials in the form of membranes or scaffolds. Cells can also be supported by hydrogels or bioprinted in controlled geometries.

1.2.3.1 2D cultures

Conventional cell lines cultures in 2D monolayers are highly accessible and reproducible, and allow high-throughput screenings characterized by one-to-one interactions between cell and pathogen. Indeed, they are often used in the study of viral infections, including respiratory virus infections [27]. For instance, the most frequent cell lines utilized for SARS-CoV-2 studies include human adenocarcinoma epithelial cell lines Calu-3 and hepatocellular carcinoma Huh-7 cells, colon carcinoma cell line Caco-2, human adenocarcinoma epithelial cell lines A549 and human embryonic kidney cells HEK-293T. The latter two usually need transduction with lentivirus- or adenovirus-based vectors expressing ACE2, in order to increase their low ACE2 expression and make them compatible with SARS-CoV-2 infection [27].

However, these submerged monolayers do not reflect the cellular composition of the organ and lack the physiological conditions that allow the native tissue to specialize in its functions.

Air-liquid interface

An improvement in 2D models is represented by air-liquid interface (ALI) cultures and, in particular, primary human airway epithelial cell ALI cultures [27]. Human airway epithelial cells can be isolated from nasal brushes and biopsies, which arise the issues of limited accessibility and high donor-to-donor variability for primary cells, or obtained from commercially available cryopreserved cells; they are cultured on a porous

membrane insert (transwell), and once confluency is reached, typically after 2–4 days, differentiation is induced by removing liquid medium and exposing the cellular layer to air (figure 6). The result is a pseudostratified, polarized epithelial layer including ciliated cells, club cells, goblet cells and basal cells [27].

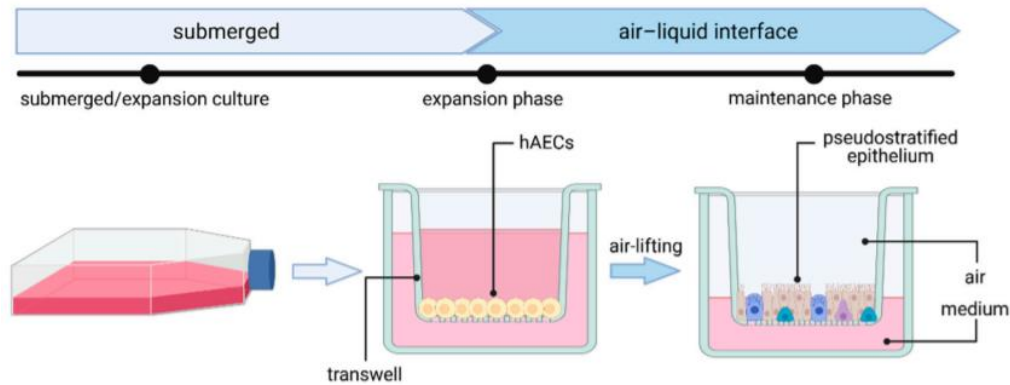


Figure 6. Human airway epithelial cells (hAECs) culture protocol for implementation of air-liquid interface (ALI). Figure created with BioRender.com (accessed on 28 April 2021). [27]

A comparison between submerged and ALI culture condition was carried out in a work by Wu *et al.* [28], where collagen coated polycarbonate membranes were seeded on the apical surface with a cell suspension of A549 lung adenocarcinoma cells, that have been used in literature to model the epithelial layer thanks to their ability to express alveolar epithelial type I cell phenotype.

To establish the ALI condition, the culture medium was removed from the apical side of the insert 24 hours after the seeding. The results showed that the expression of alveolar

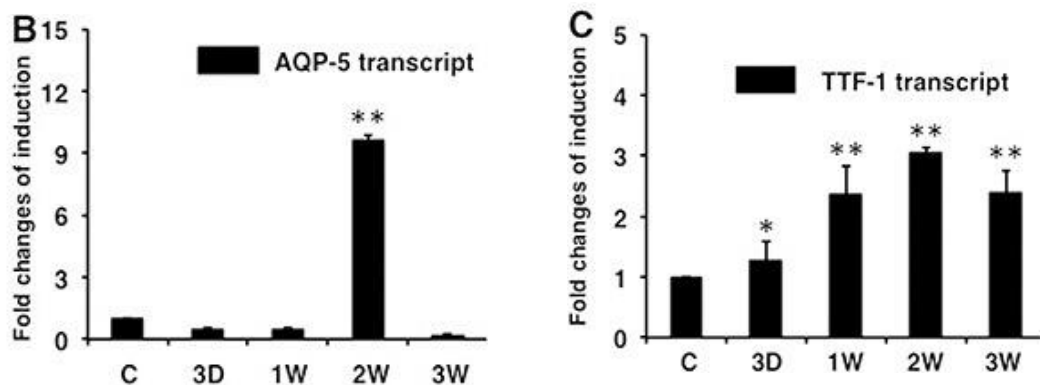


Figure 7. Comparison of qRT-PCR assay transcripts of key genes of interest in A549 cell air-liquid interface (ALI) cultures. [28]

epithelial type I cell markers AQP-5 and TTF-1 was significantly increased in ALI cultures as compared with submerged cultured A549 cells (figure 7) [28].

ALI cultures have been used to model chronic obstructive pulmonary disease (COPD), cystic fibrosis (CF), air pollutant-induced pulmonary toxicity [29] and respiratory infections, and as screening platforms to test antiviral compounds against SARS-CoV, MERS-CoV and SARS-CoV-2 [27].

Still, the complexity of *in vivo* tissue architecture, characterized by the presence of dynamic cues (osmotic and hydrostatic pressure, stress, strain, fluid flow) and tri-dimensional cell-cell and cell-ECM interactions, can't be mimicked by cell monolayers.

1.2.3.2 Co-cultures

Despite their advantages (low costs, ease of use), monocultures do not represent the complexity of the human airway architecture, whose functionality also depends on the co-presence of different cell types. The barrier function of the alveolar-capillary region is indeed achieved through cell proximity-dependent mechanisms between endothelial and epithelial cells.

To prove that, Pasman *et al.*[30] compared, as evaluation of the barrier function, the results of electrical resistance and fluorescein isothiocyanate-dextran permeability assays on inserts with porous membranes containing either no cells, Calu-3 cells (derived from human bronchial adenocarcinoma, able to model the lung airway epithelia), human lung microvascular endothelial cells (LMVECs), or co-cultures of the two, forming bi-layers. Statistical analysis showed that bi-layers are characterized by significantly

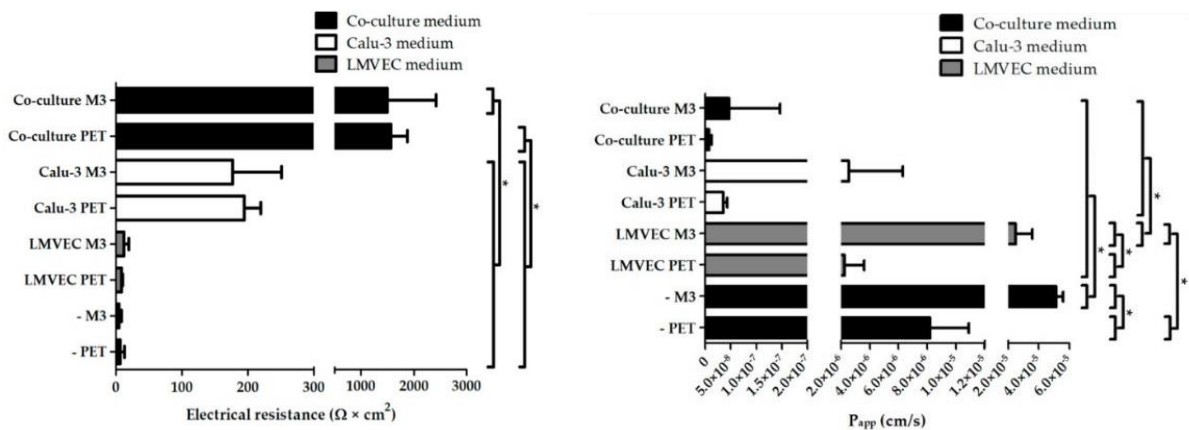


Figure 8. Electrical resistance (left) and FITC-dextran permeability assays (right) performed on inserts with poly(trimethylene carbonate) (M3) or poly(ethylene terephthalate) (PET) membranes containing either no cells, Calu-3 cells, LMVECs, or co-cultures. Capped lines depict significant differences, $P < 0.05$. [30]

lower permeability and higher electrical resistance compared to Calu-3 and LMVEC mono-cultures (figure 8) [30].

Alveolar epithelial cells (AEC) appear to mitigate the endothelial hyperpermeability also in presence of septic conditions, as in acute lung injury (ALI), characterized by pulmonary edema. Wang *et al.* [31] subjected pulmonary microvascular endothelial cells to inflammatory cytokines, and compared their septic responses in the presence/absence of co-cultured A549 epithelial cell line or primary human AEC. Results showed a protective effect not only of the presence of epithelial layer, but also of A549 cell-conditioned medium over the endothelial layer: hyper-permeability was attenuated by $39\pm 4\%$ to $100\pm 3\%$ depending on the septic stimulation ($p < 0.05$) [31].

1.2.3.3 Spheroids, organoids, assembloids

Tri-dimensional *in vitro* models can display the complex interactions in different directions between the cells and to reproduce the gradients of concentration that occur *in vivo* due to the thickness of tissues. They display physiological cell morphology, arrangement and polarization and they support long-term cultures. 3D constructs also have been proved to better mimic the resistance of *in vivo* tumor tissues to anti-proliferative drugs, which is not found in 2D cultures. On the other hand, the absence of a proper vascular network limits the maximum size of the constructs, that should be controlled and reproducible. Still, a necrotic core is usually present due to the impaired diffusive transport towards the central cells. Also, the transition from 2D to 3D drug treatment studies raises challenges in the analysis methods, since spheroids and organoids possess unique features given their heterogeneity in size, shape, and growth patterns [32].

Spheroids

Under anti-adhesive culture conditions, adherent cells tend to aggregate spontaneously forming tri-dimensional constructs, called spheroids. They can be generated from various types of cell lines or from primary cells. When matrix-free methods are adopted, ultra-low attachment surfaces or suspension cultures in media are used to allow the self-aggregation and promote the cell-cell adhesion (i.e., hanging drop technology, rotary

cultures, and bioreactors). Matrix-assisted methods involve hydrogels or scaffolds, which may model the presence of the extracellular matrix.

Spheroids represent good models for tumors. They may be obtained using more than one cell line, resulting in heterotypic models containing heterogeneous cell population of proliferating and non-proliferating cells, well-oxygenated and hypoxic cells, useful for studying the interplay between cancer cells and other cell types (i.e., immune and stromal cells) [33].

CRISPR has enabled to perform improved genetic screens to discover novel cancer drivers. Han *et al.* performed genome-wide CRISPR screens both in 2D monolayers and 3D spheroids, finding that spheroids displayed cell phenotypes more similar to those observed in tumors [32], [34].

Still, despite their advantages compared to monolayers, spheroids cannot model the organogenesis and they undergo early senescence, making extraction and maintenance of viable cells difficult.

Organoids

Organoids are tri-dimensional self-assembled constructs, able to form organ-like structures containing both stem and differentiated cell populations and multiple cell types with different functionalities. They can be established from embryonic stem cells, adult stem cells, induced pluripotent stem cells (iPSCs), or, as in the case of patient-derived tumor organoids, from patient tissue biopsies or surgically removed tumor tissues [32]. Unlike spheroids, that develop primarily via cell-to-cell adhesion, the formation of organoids is driven by internal developmental processes. For this reason, they can recapitulate histological details and simulate organogenesis, that is the process of organ development, mimicking the spatial and microenvironmental information of *in vivo* situations [32].

In a recent work [35], lung organoids were obtained from human pluripotent stem cells (hPSC) using previously established protocols, in order to evaluate if lung organoids infected by SARS-CoV-2 can serve as COVID-19 disease models and be useful as drug screening platforms to identify candidate therapeutics [35]. Quantitative PCR with reverse transcription (qRT-PCR) and RNA sequencing profiling on the organoids showed the expression of alveolar epithelial type II cell markers. Moreover, AECII-like cells showed high genetic correlation with adult AECII, and displayed the key factors involved in SARS-CoV-2 entry, such as ACE2, TMPRSS2 (a protease involved in viral entry) and FURIN (a pro-protein convertase pre-activating SARS-CoV-2) [35]. Once the permissiveness of the lung organoids to SARS-CoV-2 entry was proved, the authors performed a high-throughput screen of FDA-approved drugs, identifying several drugs that inhibit SARS-CoV-2 entry, including imatinib (a potent inhibitor of SARS-CoV and Middle East respiratory syndrome coronavirus fusion proteins) and MPA (an immunosuppressive drug used to prevent organ rejection and to treat autoimmune diseases) (figure 9) [35].

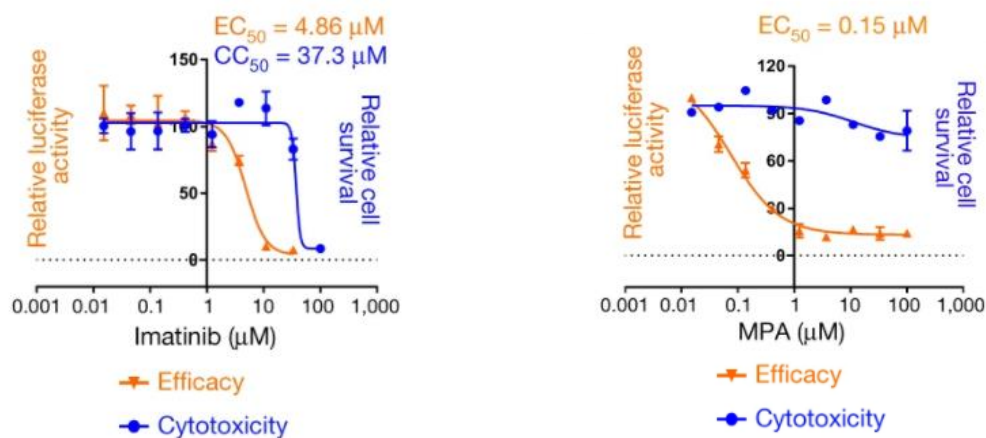


Figure 9. Efficacy and toxicity curves for imatinib and MPA in organoids after the infection with a vesicular stomatitis Δ G-luciferase virus pseudotyped with the SARS-CoV-2 spike protein (SARS-CoV-2-entry virus). [35]

Assembloids

Organoids are good models of pre-natal tissue development, but they are non-interacting and isolated constructs, being unsuitable to imitate complex pathways. Assembloids may overcome this limitation and improve the model.

Assembloids consist of two or more organoids physically in contact with each other. They can mimic the interaction between the different regions and cell lineages of an organ or a system. Once a region-specific organoid is generated, it can be assembled with other cell types, obtaining multilineage assembloids, or with morphogens or organizer-like cells, giving polarized assembloids, or again with other organoids generating multiregion assembloids with long-distance projections. They have been used in the modelling of the interactions between the different regions of the brain or to mimic the cortico-motor pathway.

Recently, Wang *et al.* [36] generated cortical organoids and assembled them with pericyte-like cells, that are perivascular cells within the brain that are proposed as SARS-CoV-2 infection points. The resulting multilineage assembloids support SARS-CoV-2 entry and replication in neural tissue [36], and allow to study virus' potential neurotropic effects. Indeed, besides prominent respiratory symptoms, COVID-19 may also cause neurological manifestations (weakness, dizziness, headache, and hyposomnia) as well as neuropsychiatric symptoms (confusion, cognitive decline, anxiety, insomnia, and depression) [37]. Assembloids may be useful to mimic the cellular heterogeneity of tissues, that implies variable expression of ACE2 and hence non-fully predictable susceptibility to SARS-CoV-2, that is able to infect cells through the ACE2 receptor.

1.2.3.4 Tissue Engineering techniques

Tissue engineering could be defined as the group of techniques “combining living cells with a natural, synthetic, or bioartificial support to develop a biological substitute or a 3D living construct that is structurally, mechanically, and functionally equal to a tissue” [38], [39]. Since “function arises from structure” [39], scaffolds act as the support that aims to replicate the architecture of the native tissue's ECM in order to promote cell adhesion, spreading, proliferation, differentiation, and maturation [38]. The composition, the mechanical properties and the surface characteristics of the biomaterial chosen for the scaffold strongly affect the cell fate: bioartificial materials often represent good compromises between the needed mechanical support and a biocompatible and bioactive surface. Also, once exposed to media and cells, a scaffold should maintain its structural integrity until the loaded cells adapt to the environment

and excrete enough extracellular matrix to compensate the degradation of the biomaterial [40].

Porous microspheres: double emulsion and porogen leaching

One of the applications of scaffold-based techniques is the analysis of cancer cell invasiveness [33] and interaction with the native ECM. For example, Dhamecha *et al.* [41] established a method to obtain porous, biodegradable poly(lactic-co-glycolic acid) (PLGA) microspheres to recreate lung cancer microenvironment. Microsphere scaffolds supply a large surface area for cell attachment and proliferation; they offer better control over the dimensions and the physical properties of constructs compared to other approaches (like matrix-free spheroids), therefore helping to obtain consistent and repeatable results during pharmaceutical drug testing [41]. In this study, alginate microspheres were formulated by water-in-oil emulsion technique. They were later used as porogen to obtain porous PLGA microspheres by double emulsion solvent evaporation technique (figure 10).

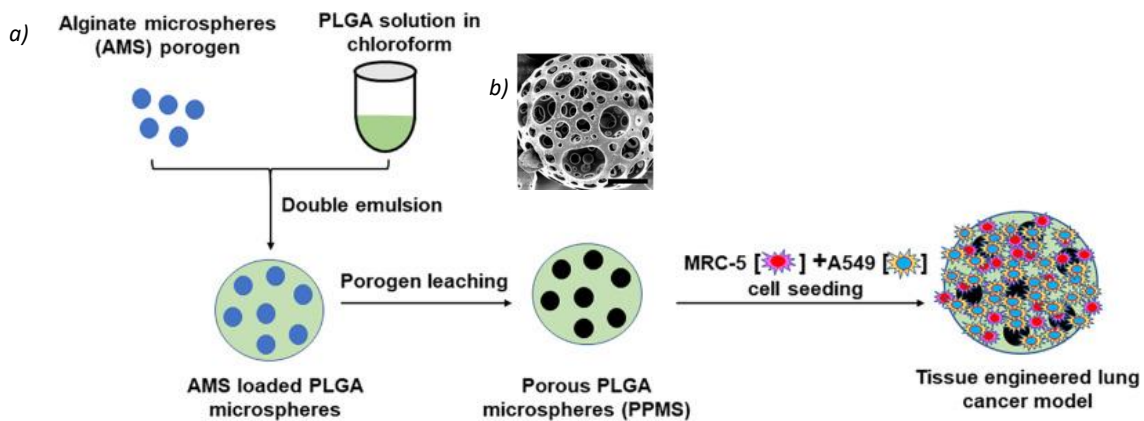


Figure 10. a) Schematic representation of preparation of porous PLGA microspheres [38]. b) SEM image of porous PLGA microspheres based on ratio of porogen (mg) to PLGA (mg) used in the formulation 6:50 [41].

The results showed that the collagen-coated porous PLGA microspheres (Col-PPMS) co-cultures are significantly more resistant to all the tested drugs when compared to the 2D monolayer co-culture (figure 11). Cancer cells show indeed the tendency to become more robust in 3D models: the greater cell-cell interaction within the 3D model and the

impaired drug diffusion to the core due to the compact arrangement of cells would better represent treatments given *in vivo* [41].

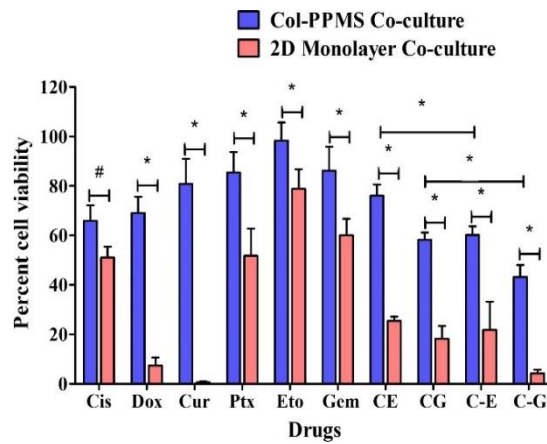


Figure 11. Comparative *in vitro* screening of anti-cancer drugs on monolayers and scaffold-based co-cultures. Significance was analyzed by Student's *t*-test (* $p < 0.001$, # $p < 0.01$). [41]

Re-endothelialized lung scaffolds

Lung transplantation represents the ultimate but necessary option for the end-stage of some chronic respiratory diseases, like interstitial lung disease, and genetic conditions, such as cystic fibrosis [42]. However, there is low availability of suitable donor lungs and the rates of acute and chronic rejection are high [42]. *Ex vivo* lung tissue engineering, involving the use of re-endothelialized biological scaffolds, may increase the success rate of lung transplantation. Biological scaffolds can be derived by decellularizing native lung tissue, that means removing the cellular and nuclear material while preserving both the micro- and macroarchitecture of the organ, the extracellular matrix (ECM) composition and tissue structure [42].

Decellularized organ scaffolds are therefore ideal for tissue engineering, because they contain organ-specific vascular and parenchymal architecture, and cells for re-endothelialization can be harvested directly from the intended transplant recipient, lowering the risk of rejection. [43]

Scarritt *et al.* [43] optimized a strategy for the re-endothelialization of decellularized rat lung scaffolds exploiting gravity with the aim of promoting widespread colonization by the cells, which is fundamental in order to prevent adverse host reaction and avoid the

scaffold to become thrombogenic after implantation. The authors found that, while perfusion pump-driven seeding causes increased cell fragmentation and death, gravity-driven seeding supported cell survival and efficient re-lining of the vascular walls [43].

Electrospun membranes

Models of the alveolar-capillary barrier often involve microporous membranes fabricated from polycarbonate (PC), polydimethylsiloxane (PDMS), or polyethylene terephthalate (PET) with track-etched pores, as in the case of commercial transwell inserts [40]. These synthetic scaffolds should mimic the natural basement membrane between the endothelial and epithelial alveolar layers, but they usually exceed the physiological thickness - which is not larger than 2 μm . Additionally, unlike the commercial membranes, the native basement membrane is characterized by a fibrous topology that imparts structural integrity, while its interconnected pores, ranging between 10 and 150 nm, allow the selective transport of solutes and proteins, paracrine signaling, as well as the transmigration of immune cells across the alveolar barrier [40]. Electrospun nanofibrous scaffolds are therefore ideal candidates to mimic the native barrier, since their thickness and porosity may be adjusted optimizing the electrospinning process' parameters.

Electrospinning is a process that allows to produce nanofibers using an electrostatic guidance system for their controlled deposition on a substrate. A high voltage is applied between the nozzle of the syringe, containing the polymer and its solvent, and a collector: after the Taylor's cone creation, the solution is extruded, thanks to the potential difference, into fibers, that solidify on the collector while the solvent evaporates.

Jain *et al.* [40] cultured human pulmonary microvascular endothelial cells (HPMEC) and human distal lung epithelial cell line NCI-H441 on 2 μm electrospun PCL membranes to establish the alveolar-capillary barrier, while 10 μm thick PET membranes with 0.4 μm pore size were used as control. To investigate the integrity and stability of cell layers, immunofluorescence staining of cell junction protein CD31 in HPMEC and junctional complexes E-cadherin in H441 cell layers was performed and analyzed using confocal laser scanning microscopy: images showed well-organized CD31 and E-cadherin and intact barrier function [40].

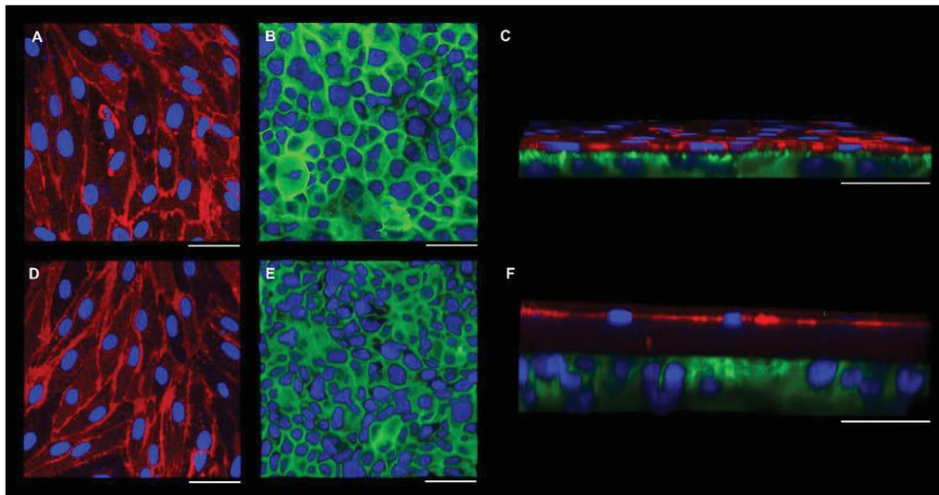


Figure 12. Confocal laser scanning microscopy images of the alveolar–capillary barrier established on 2 μm PCL nanofibrous meshes and control (PET membranes) and their cross-sections (C, F). In red, endothelial cell-specific marker (CD31-red), in green, epithelial adherens junction (E-cadherin-green), in blue, cell nucleus (DAPI-blue). Scale bar: 50 μm . [40]

Despite the thinness of the scaffold, no cell infiltration was observed (figure 12) [40]. Indeed, tight junctions between epithelial cells prevent the cytokines, toxins, and pathogens from infiltrating the epithelial layer and regulate the permeability of solutes and ions through the paracellular space. Immune-staining of cellular tight junctions (ZO-1) and transepithelial electrical resistance (TEER) measurements were performed, confirming the integrity of the formed barrier in the ultra-thin model and in the control [40].

Bioinks

Three-dimensional bioprinting is “an additive manufacturing technique to print bio-functional materials in a layer-by-layer manner” and with hierarchical architecture similar to the native tissue that is intended to be mimicked [39]. ‘Bioinks’, that are the

printed biomaterials, consist of a support material hosting living cells, characterized by mechanical and rheological properties that ensure printability, shape fidelity and cell survival. Hydrogels derived from natural polymers like alginate, agarose, collagen, are highly biocompatible and biodegradable; unlike synthetic polymers, that need functionalization, they are inherently bioactive, that is, they offer biochemical cues that favour cell adhesion (like ECM-derived proteins) [39]. On the other hand, they lack reliability due to high variability between batches and they are usually characterized by poor mechanical properties, as opposed to synthetic hydrogels, whose mechanical properties are tunable and reproducible [39].

Kang *et al.* [44] fabricated a thin, three-layered alveolar barrier model via inkjet printing of human lung cell line NCI-H1703 to model flat squamous AECI, NCI-H441 for the cuboidal AECII, endothelial HULEC-5a, and fibroblasts, in collagen ink. Endothelial cell bioink, collagen ink, fibroblast bioink and epithelial cell bioink were sequentially printed in a layer-by-layer manner in a transwell porous support [44]. The model was cultured for 14 days assuring the presence of the air-liquid interface, that is, exposing the epithelium to air. The resulting 3D construct was evaluated and compared with control models (a 3D non-structured collagen model containing a random heterogeneous mixture of all four cell types and a cell-free collagen model without cells). The TEER value of the bioprinted structured model had higher value from the day 1 and increased steadily for the following 14 days, while the permeability was significantly lower compared to that of the controls, thanks to the organized, homogeneous and dense distribution of cells, that were able to form tighter junctions than the control models [44].

1.2.3.5 Microfluidic approaches

Since the ultimate goal of tissue engineering could be found in the clinical replacement of human organs or tissues, the approaches involved usually aim to obtain replications at the original scale of the native tissue (as for decellularized scaffolds). In contrast, Organs-on-Chip strive to miniaturization, mimicking physiological architecture, functionality and biophysical cues at a smaller scale [45].

Organs-on-Chip are indeed high-throughput microfluidic devices, whose underlying principle is to precisely manipulate and process microscale (10^{-9} to 10^{-18} L) fluids, acting

primarily as a laminar flow, using channels that range in size from tens to hundreds of microns, known as a “lab-on-a-chip” [46]. Microfluidic channels therefore allow the use of low volumes of reagents, reducing costs, making the experiments easier to control and increasing the velocity of the responses. Also, the simple manipulation of flow rate, pressure, oxygen concentration, pH and other chemical parameters allow to provide controllable culture conditions reflecting *in vivo* situations [45].

Advantages

- Compared to the models previously discussed, organs-on-chip support dynamic culture conditions, similar to those found *in vivo*, where fluid shear stress induces organ polarity and signaling cascades, through micro-pump perfusion [46].
- Angiogenesis and cell migration are some of the biological phenomena driven by concentration gradients: the laminar flow in the microfluidic channels, together with the possibility of altering flow velocity and channel geometry using microvalves and micro-pumps, allow to establish stable, three-dimensional gradients of biochemical molecules, controlled both spatially and temporally, in order to mimic complex physiological processes [46].
- Incorporating scaffolds, such as porous membranes, into organ-on-chips enables the application of mechanical stimuli on cells and the modelling of tri-dimensional interactions, whose role is fundamental in cell organization and gene expression.
- Microfluidic approaches reduce the complexity of the experimental operations, reduce energy and material consumption, decreasing costs and experimental time. The small sizes allow to focus only on microscale physics, enabling parallelization, precision and automatization while resulting in high analytical throughput.

Fabrication

The material of choice for the fabrication of microfluidic devices is usually the silicon-based organic polymer polydimethylsiloxane (PDMS) [45], consisting of a polymeric chain with repeating Si-O groups and CH₃ groups on the side. It is particularly suitable for biomedical applications, since it is biocompatible, chemically inert, thermally stable

and gas permeable; it is also optically transparent and non-fluorescent, that make it compatible with monitoring techniques. PDMS is easy to handle and its production is simple and low cost compared to other materials.

PDMS microfluidic platforms can be obtained starting from molds where the pre-polymer can be poured and peeled off after reticulation. The molds are in their turn usually realized through photolithography techniques, where a pattern is transferred from a mask to a polymeric substrate, or via 3D printing.

- Soft lithography is a microfabrication method where the master, that is the mold from which the final PDMS replica will be obtained, is made of a flexible elastomeric material, which typically also is PDMS. The master is obtained through traditional lithography: during exposure, UV rays or X rays beams hit a mask and the underlying substrate, coated with a resist, a photosensitive polymer. The photo-mask contains a spatial binary information that describes the pattern: according to the type of resist (positive or negative), the exposed substrate will be reticulated or made soluble by the light, and vice versa for the parts protected by the mask. After the development, where the excess of resist is removed, the result is a wafer with a tri-dimensional pattern. In soft-lithography, this is the final desired pattern. The wafer will be used to realize a reusable PDMS master, representing the negative of the final design, and where the material chosen for the final device will be poured to obtain a chip via micro-replica molding.
- Laser ablation technique involves the writing of the wanted design on the substrate, that can be thermoset and thermoplastic polymers like PMMA, by evaporating the material at the focal point. Laser ablation is a faster and simpler method to realize masters compared to soft-lithography, but its resolution is also poorer.
- Fused deposition modelling, stereolithography and PolyJet technology are some of the additive manufacturing techniques for the realization of tri-dimensional objects based on CAD models: they represent a method to obtain molds in a fast and simple way with a good resolution, but still lower than that of photolithography masters.

To obtain microfluidic systems, the PDMS replica can be bonded on glass substrates or coupled with other layers of micropatterned PDMS to create channels for the passage of fluids or biological samples. Surface treatments like plasma oxygen can be performed in order to consolidate the bonding and obtain a tight seal.

Applications

Drug screening is a process that also includes target identification, regulatory studies, and the development processes for therapeutic agents [47]. Even though they pass the numerous and expensive pre-clinical trials, 90% of drugs that enter phase I clinical trials ultimately fail [47]. Organ-on-chips are powerful tools in drug screenings, but they still are isolated devices that can't represent the complex interactions between all the different tissues and organs in the human body: this may prevent predicting huge side effects of a compound on tissues different from the target.

In order to address this issue, Skardal *et al.* [47] designed a dynamic system with the aim of modelling the effect of a compound on different tissues able to communicate each other, eventually reducing the failure rate of drug screenings. The system includes three organ-on-chip microreactors, realized in PDMS via soft lithography and replica molding, housing liver, lung, and heart constructs (figure 13). The systems are connected serially under fluid flow controlled by a micro-peristaltic pump, and each module is a 'plug-and-play' type, meaning they can be easily and directly inserted in the circulatory system, which also supports the removal or addition of different tissues. While the heart and liver organoids were obtained by bioprinting spheroids and culturing them in suspension conditions, the lung model consists of a co-culture of pulmonary epithelial cells and pulmonary fibroblast layered on a side, and endothelial cell on the other side of a porous membrane. The epithelial surface exposed to the air-liquid interface showed a polarized phenotype, and the endothelium formed a thin vascular barrier adjacent to the liquid media [47]. The layered organoid showed an integer barrier function and is suitable for

long-term culture. Once all the constructs were mature, they were connected into the same circulatory flow to be subjected to perfusion.

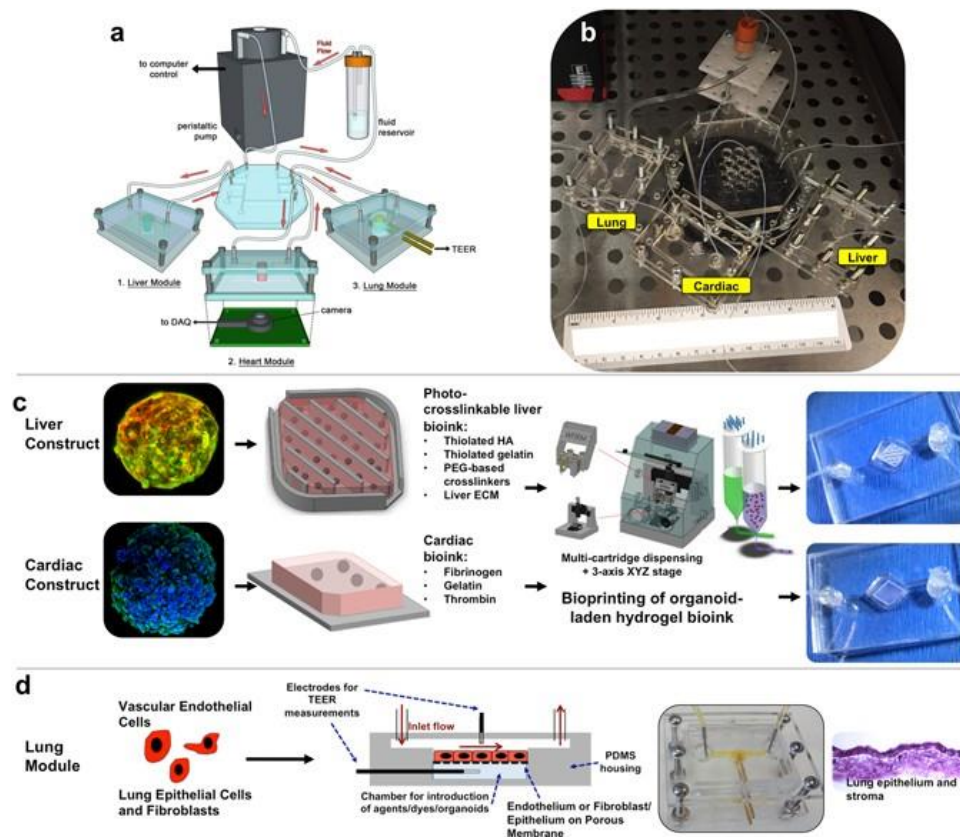


Figure 13. Illustration and photograph of the modular multi-tissue organ-on-a-chip hardware system. (d) Lung models consist in layers of cells over porous membranes within microfluidic devices. TEER (trans-endothelial [or epithelial] electrical resistance) sensors allow monitoring of tissue barrier function integrity over time. [47]

The authors' initial goal was to use bleomycin to demonstrate a specific targeted insult to the lung, while not harming the liver or cardiac organoids [47]. Bleomycin is a drug whose known effects are to cause lung fibrosis and inflammation. Bleomycin was infused on day 3 of the study, and on day 9 the study was concluded [47]. The LIVE/DEAD analysis of organoids in both the no drug control groups and the bleomycin-treated groups yielded relatively low numbers of dead cells. However, the cardiac organoids in the bleomycin-treated systems appeared to be partially disaggregated and stopped beating, as opposed to the untreated ones that showed consistent beating. Since bleomycin is not known to cause cardiotoxicity (cardiac contractility alteration), the authors did not expect these results: moreover, repeating the study on a cardiac-only system, without other tissues, bleomycin did not cause cessation of cardiac organoid beating [47]. Further analysis proved that bleomycin is not, indeed, inherently

cardiotoxic, but it does induce lung inflammation, and therefore the production of inflammatory cytokines like IL-beta1, which is instead cardiotoxic and undermines cardiac functionality (figure 14). The authors ultimately proved that the influence of each organ over the functionality of other tissues with which it communicates is a critical factor in predicting the possible negative effects of a compound on non-target tissues during preclinical trials [47].

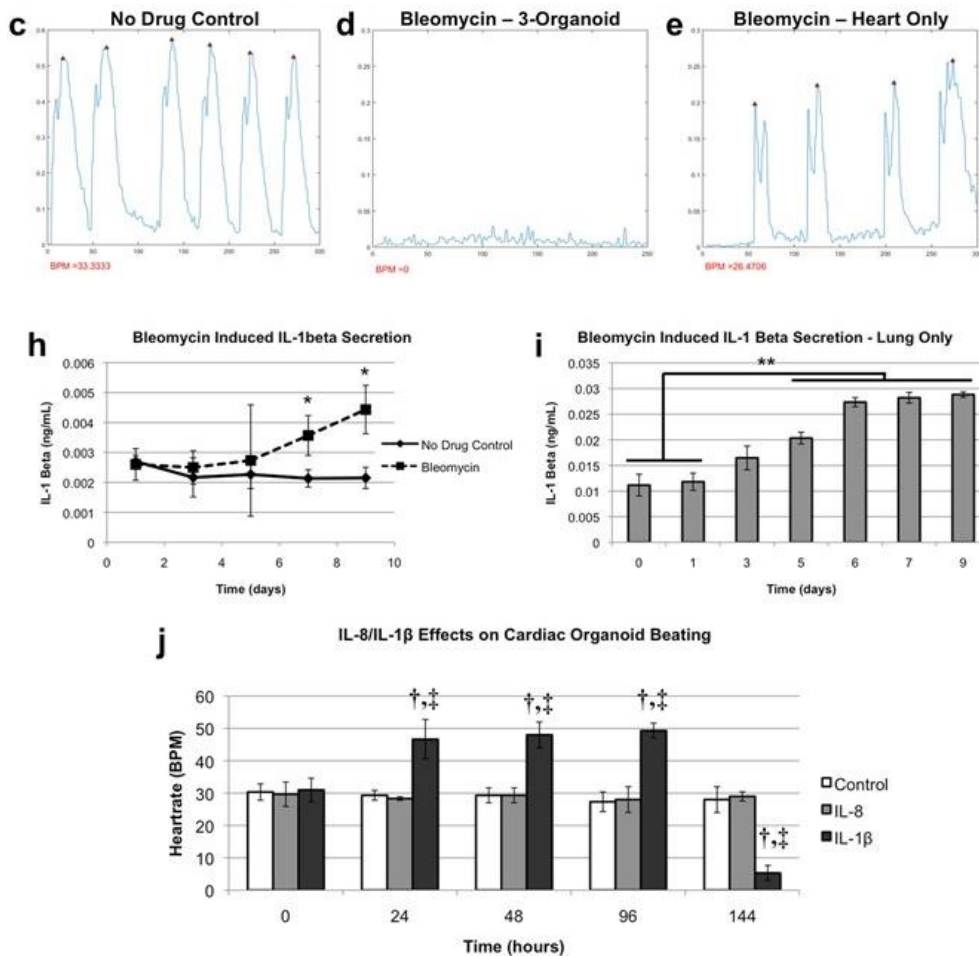


Figure 14. (c–e) Cardiac organoid beating plots on day 9. (h,i) Assessment of inflammatory factors following bleomycin administration on day 3. (j) IL-1 β effect on beating rate. [47]

Since lung-on-chip models can recapitulate many aspects of the small airways, like the alveolar–capillary interface and its complex microenvironment, they also enable the study of respiratory viral infections and other respiratory diseases such as asthma, chronic obstructive pulmonary disease, cystic fibrosis, pulmonary edema, and intravascular thrombosis [48]. For example, in their microfluidic alveolus chip model, Zhang *et al.* [48] investigated the immune response to SARS-CoV-2 infection. The device

consisted of an ECM-coated porous membrane, enabling the co-culture of human alveolus epithelial cells, pulmonary microvascular endothelial cells and immune cells between two perfused channels (alveolar lumen and vascular channels) [48] (figure 15). The top channel was used to infect the barrier model, while circulating immune cells were added in the vascular channel, in order to examine the pathological changes of epithelium–endothelium interface and inflammatory responses after virus infection [48]. At this point, the team treated the virus-infected human alveolus chip with Remdesivir, which demonstrated to be able to suppress virus replication and minimize virus-induced injury of alveolar-capillary barriers [48].

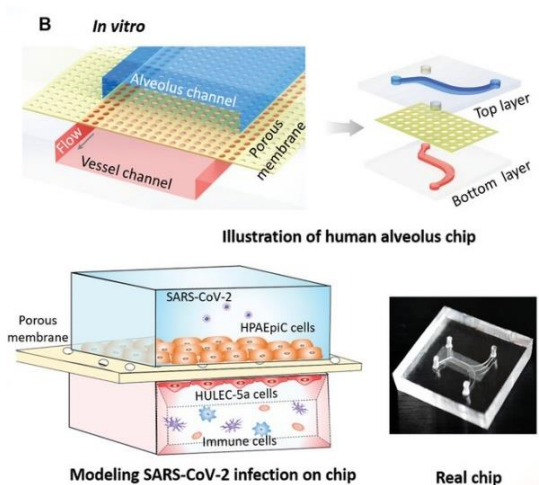


Figure 15. The human alveolus chip is exposed to SARS-CoV2 on the epithelial layer (blue), and human immune cells are infused into the bottom vascular channel (red) during the progression of virus infection. [48]

1.3 Alveolus-on-chip: background works

In vivo, the alveolus air–blood interface is an ultrathin barrier consisting of tight epithelial and endothelial cell layers supported by the elastic fibers of the extracellular matrix rhythmically expanding and contracting [49]. It represents the functional element of the lung but modelling it can be difficult and complex. The key components that should be included in accurate alveolar-capillary barrier *in vitro* models are: the co-culture of the main cell types involved in the barrier function, a stretchable substitute of the basal membrane, presence of air-liquid interface, perfusion and consequent shear stress upon the endothelium, that *in vivo* is caused by blood pressure, and cyclic mechanical stimulation mimicking respiration, that causes an average 10% deformation with a frequency of 0,2 Hz. Microfluidic devices have the potential to meet these requirements while being versatile enough to mimic different pathological conditions.

This section will focus on the description of two different approaches to the realization of the cyclic deformation: via the creation of vacuum and through the application of a positive air pressure over the cells.

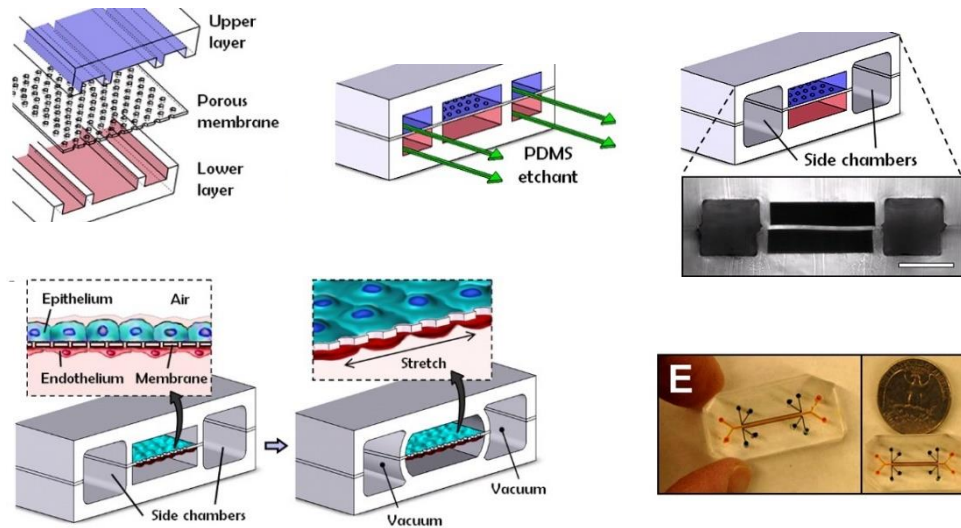


Figure 16. Selective etching of the membrane in the channels produces two side chambers for the application of vacuum that causes mechanical stretching of the central PDMS membrane (scale bar, 200 μm). (E) View from above of a lung-on-a-chip. [50]

One of the first models summarizing the main aspects of the alveolar-capillary barrier is represented by the device by Huh *et al.* [50], composed by two layers equipped with a central channel and two side channels (figure 16). The central one is divided by a PDMS porous membrane, that creates two separate chambers: the upper chamber is dedicated to air, the lower one to the medium flow. The side channels are connected by silicon tubes to a vacuum pump controlled by a software that allows the mechanical stretching of the membrane by vacuum creation at both sides of the central membrane. The porous membrane was coated with ECM in order to support a co-culture of human alveolar epithelial cells and human pulmonary microvascular endothelial cells on its opposite sides [50]. After reaching the confluence, the epithelium was exposed to air. Living *Escherichia coli* bacteria constitutively expressing green fluorescent protein was later integrated in the medium, inducing the endothelium activation [50]. Concurrently with the application of the cyclic strain, toxicology analysis was performed with silica on the epithelial side, where the cells showed an inflammatory response, further confirming the good resemblance of the model with the native tissue and its value in the evaluation of the effects of potentially damaging conditions [50].

A different approach was pursued by Radiom *et al.* [51], whose model consists of an array of hexagonal monolayers of electrospun gelatin nanofibers suspended over microframes, and integrated in a microfluidic device (figure 18).

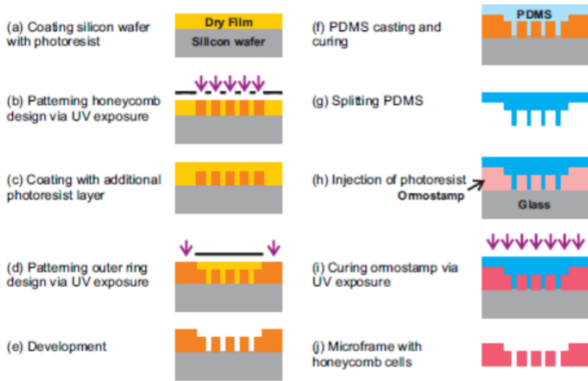


Figure 17. Fabrication steps of honeycomb microframe. [51]

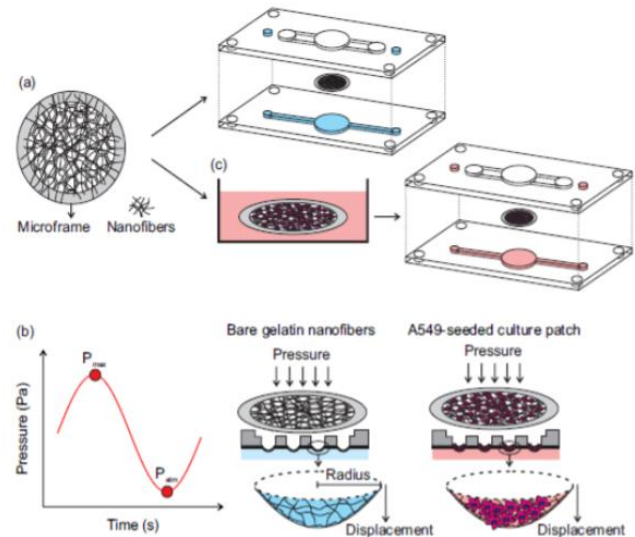
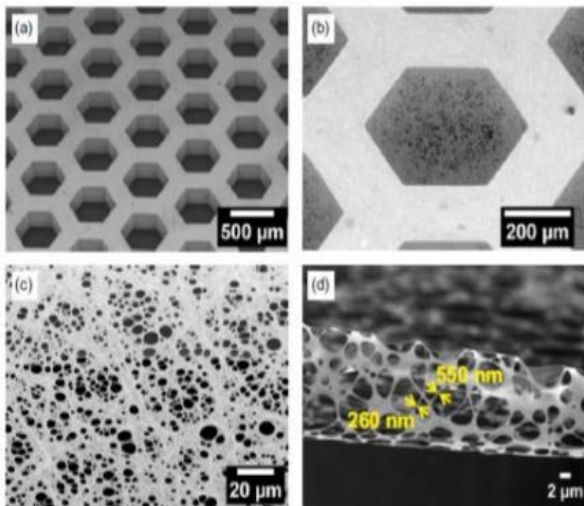


Figure 18. On the left. (a-d) Scanning electron microscopy (SEM) images of 24 honeycomb microframes and of a suspended monolayer of gelatin electrospun nanofibers. On the right. The chip allows the application of air pressure from apical channels and liquid flow from basal channels. [51]

The human alveolar air sacs can be indeed approximated to hexagons with a diameter of about 200 μm . The suspended monolayers of the described model have a diameter of 500 μm a thickness less than 1 μm , with a low elastic modulus that allows their deformability at the air-liquid interface [51]. The breathing cycle was mimicked by applying positive air pressure, in the range of 200 – 1000 Pa, with a frequency of 0.2 Hz during 1 hour, over the gelatin monolayers cultured with human lung epithelial A549, resulting in a central displacement of 40 – 80 μm (figure 19), corresponding, when compared with the surface of the substrate, to a linear strain of 2 – 10% in agreement

with the physiological deformation in the lung alveoli [51]. The authors found that the strain induced remodelling of the actin cytoskeleton: the cells appeared to be less rounded, and their distribution on the gelatin monolayer appeared more homogenous in the samples subjected to the mechanical stimuli compared to the control. This means that the periodic strain may encourage cell migration towards less covered regions of the substrate, resulting in the formation of a tighter cell layer [51]. The model is overall suitable for lung investigations, but it could be improved by adding more cell types in order to mimic the native cell population.

$$P = \gamma \left(\frac{1}{R_1} + \frac{1}{R_2} \right)$$

Figure 19. Laplace's equation for the calculation of the displacement of the monolayer at the air-liquid interface. γ is the liquid surface tension equal to 72.8 mN/m for water, and R_1 and R_2 are the two principal radii of curvature. [51]

2. Aim of the work

The aim of the present work was the realization of an alveolus-on-chip for the modelling of the alveolar-capillary barrier, which plays a fundamental role in pulmonary homeostasis and whose dysfunction is associated with various diseases. The device consists of a PDMS microfluidic platform able to embed a nanofibrous scaffold, hosting the alveolar-capillary barrier model. The model is a co-culture of epithelial (A549 cell line) and human lung microvascular endothelial cells (HULEC-5a) on an electrospun PCL/gelatin membrane, mimicking the human alveolar wall. The main challenge was to develop a device able to recapitulate the fundamental factors characterizing the physiological alveolar tissue: a multi-layered structure, the presence of an air-liquid interface (ALI) in the apical compartment of the device and the implementation of a mechanical stimulation of the barrier model.

The starting point for the development of the device was the thesis work of Eleonora Palumbo [52], where the PDMS layers constituting the alveolus-on-chip were obtained from poly(methyl methacrylate) (PMMA) molds, realized by laser ablation technique. The goal of the present work was to adapt the design to a different microfabrication technique, the Poly-Jet 3D printing, and to modify the pattern to overcome some of the device limitations reported in the cited thesis [52].

The first issue addressed during redesign phase was the position of the medium flow inlet and outlet. In the configuration designed by Palumbo, inspired by other literature works ([50], [51], [53]), inlet and outlet were positioned on the two sides of the central culture chamber, exposed to air for ALI implementation, in the upper layer of the chip, making the channels accessible from the top. During the static condition phase of the culture, inlet and outlet holes also served the role of endothelial cells medium reservoirs, and were therefore filled so that the fluid level was higher than the membrane level. This caused the medium level to rise above the central membrane, reaching the level of the fluid in the side holes. In the attempt to avoid the upper side of the membrane being wet during ALI condition due to liquid level rising, the endothelial cells medium reservoirs were removed from the upper layer, and inlet and outlet were moved to the side of the chip. At this point, the microfluidic channels of the bottom layer were designed as serpentine in order to contain a volume of medium sufficient to

compensate for the absence of top layer reservoirs. Plugs were realized to seal the microfluidic channels inlets when needed. The geometry of the microfluidic channels, the shape of the inlets and the number and dimension of the pillars supporting the membrane were optimized after various printing tests, microfluidic experiments and cell adhesion evaluation.

3. Materials and methods

The microfluidic device hosting the alveolar-capillary barrier model consists of three PDMS layers.

- The bottom layer is characterized by microfluidic serpentine and a circular culture chamber, equipped with pillars to support the membrane, and conceived for the seeding and maintenance of the HULEC-5a.
- The membrane is hold in place, suspended on the culture chamber, between the bottom and the top layer, which presents a circular hole that exposes the upper part of the membrane to air.
- The final layer serves the role of a reservoir, thanks to a hole having a wider diameter that allows the stocking of A549 epithelial cells' medium until the air-liquid interface implementation.

Each patterned PDMS layer was obtained starting from 3D-printed molds. After the assembling of the layers with the electrospun membrane, endothelial and epithelial cells were seeded on the lower and upper side, respectively, of the fibrous mat.

3.1 3D printing

3.1.1 Mold design

The CAD model of the mold for each layer was designed using the software Rhinoceros® (Robert McNeel & Associates), based on a non-uniform rational basis spline (NURBS) mathematical model that allows to represent 2D and 3D geometries. In particular, the tridimensional model was obtained starting from a 2D drawing and extruding each component as closed surface. The final CAD design represents the negative of the desired pattern of the PDMS layer.

Bottom layer

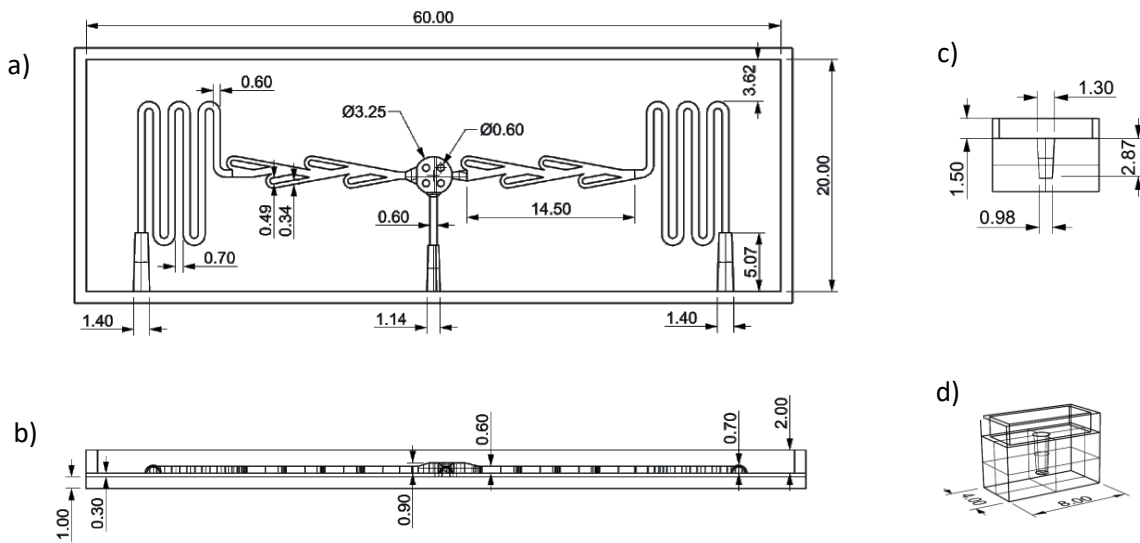


Figure 20. On the left, top view (a) and front view (b) of the CAD model of the master of the bottom layer. On the right, front view (c) and perspective view (d) of the CAD model of the master of the plug for the conic inlets. Dimensions are expressed in millimeters.

The master of each layer of the device is characterized by an external frame, 1 mm thick and 2 mm high, that contains the liquid poured PDMS during its solidification in the mold, whose internal surface has a size of 60 mm x 20 mm (figure 20, A, B). Attached to the frame of the bottom layer's mold, 2 lateral inlets shaped as semi-truncated cones give access to the two lateral sets of serpentes, having 600 μm width and 600 μm height (figure 20, A, B). The half-inlets of the bottom layer are completed by the corresponding halves in the top layer (figure 21), so that the resulting conic shape fits the micropipette tips used during the experimental phase, improving the filling process and avoiding leakages from the inlet. The microfluidic serpentes have been designed to maximize the volume of cell medium that can be stocked in the device during the static phase of the cell culture. These microfluidic channels are connected to valvular conduits, designed on the basis of Nikola Tesla's original patent (Appendix I) [54]. Once reaching the central culture chamber, the microfluidic resistance encountered by the flow in the PDMS pattern would induce the liquid level to rise above the central membrane or to flow back towards the inlet used as entry point, preventing the liquid to fill the second set of channels. To reduce the effect of these phenomena, Tesla's one-way passive valve was implemented. Thanks to its direction-dependent fluidic resistance, given by the convoluted shapes that create a preferential path [55], the valvular conduit has the purpose of facilitating the cell medium to flow towards the

desired direction (that is from the left inlet to the right outlet in figure 20, A), contrasting the liquid to flow back and to rise above the membrane during the filling of the second set of serpentes. In previous works, Tesla's valve has been studied for microfluidic applications [56] [57], where it was used in microfluidic mixer networks for the creation of gradients to obtain convective mixing of flows.

The valvular conduit leads to the central element of the master. This circular component, originating the culture chamber, is 1 mm high, with 4 holes having 600 μm diameter, which will create PDMS pillars sustaining the electrospun PCL/gelatin membrane. Before the extrusion of this central element, a closed surface including the four sides of the frame and the four central 600 μm circles was extruded towards the bottom of the model for 300 μm : this allowed the printer to anticipate the creation of the holes before completing the base of the object, compensating for the partial obstruction of the holes that occurs during the deposition of the liquid resin layers. A third central inlet, smaller than the others, directly gives access to the culture chamber through a 600 μm x 600 μm channel, and was used for the seeding of HULEC-5a.

The bottom layer is able to stock a total volume of cell medium of about 80 μL , sufficient to provide enough nourishment to the HULEC-5a in the culture chamber for at least 24 hours before the medium refill. In order to seal the central channel during the filling of the microfluidic channels, after the use of the central conic inlet for cell seeding in the lower part of the membrane, custom mold for the realization of a PDMS plug was realized (figure 20, C, D). The plug allows the fluid to flow through the first set of serpentes and the first valvular conduit, to fill the culture chamber and to move towards the second set of conduits without leaking from the central channel. The plugs are later used to seal all the three inlets during the air-liquid interface phase.

Top layer

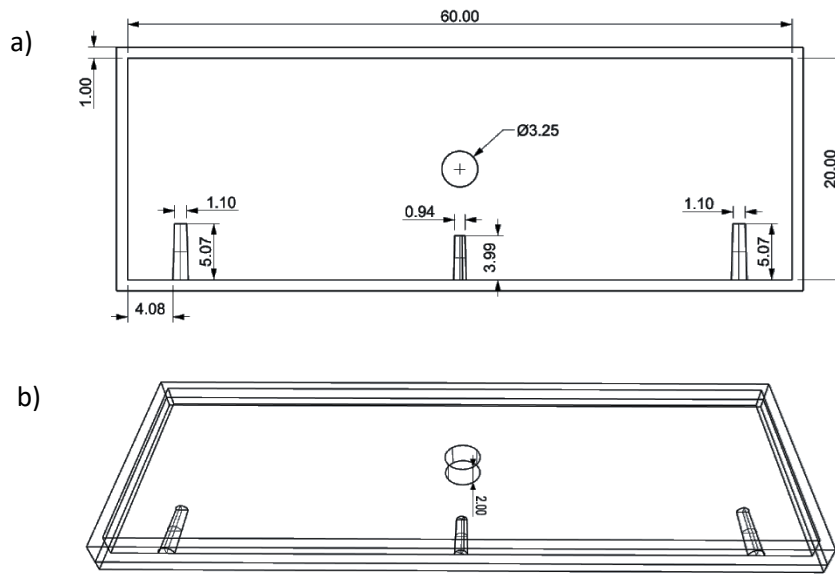


Figure 21. Top view (a) and perspective view (b) of the CAD model of the top layer master. Dimensions are expressed in millimeters.

The top layer, 2 mm thick, serves the purpose of sealing the microfluidic channels of the bottom layer, and its 3 semi-inlets complete their correspondent in the lower layer. A 2 mm high central extrusion in the CAD model of the mold (figure 21) generates a hole, having same diameter of the culture chamber below (3.25 mm), in the replica. The hole allows to expose the upper part of the membrane to air, for the implementation of the air-liquid interface condition 72 hours after epithelial cells seeding.

Reservoir

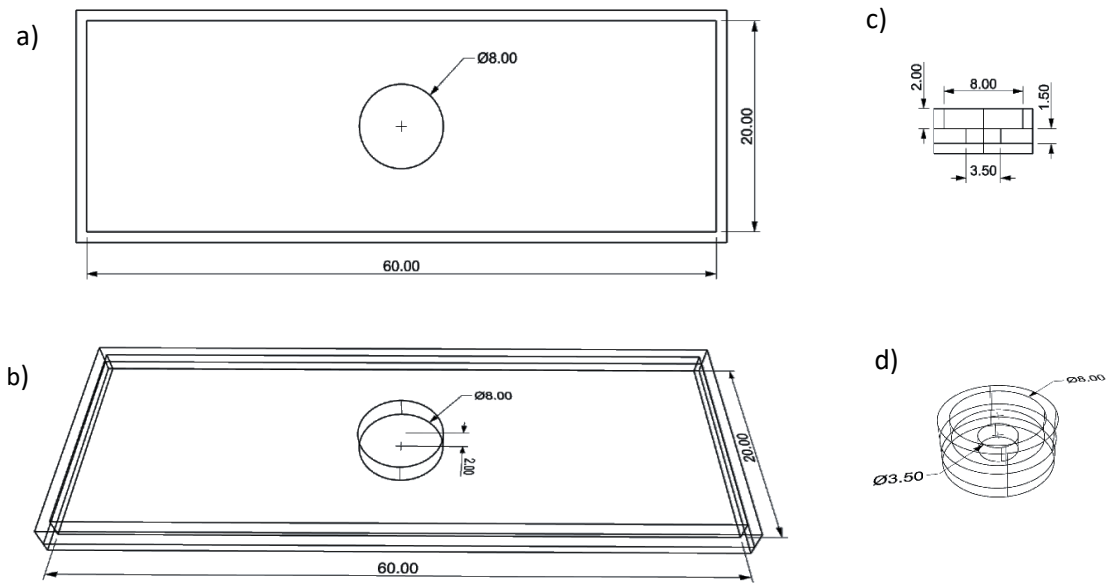


Figure 22. On the left, top view (a) and perspective view (b) of the CAD model of the reservoir master. On the right, front view (c) and perspective view (d) of the CAD model of the master of the plug for the central upper hole. Dimensions are expressed in millimeters.

The final layer acts as medium reservoir. The CAD model of the mold (figure 22, A, B) presents a 2 mm frame, just as the previous layers, and a central 2 mm extrusion with an 8 mm diameter, creating the hole in the replica that, concentric to the one in the top layer, allows the stocking of about 100 μ L of epithelial cells medium.

A mold was designed to obtain a PDMS plug able to fit the concentric holes of top layer and reservoir (figure 22, C, D): sealing the upper layers facilitates the filling process of the microfluidic channels, assisting in preserving the air-liquid interface during the experimental phase. The vertical dimensions of the plug were studied to avoid contact between the plug and the central membrane. Using a puncher to create a through-hole, the plug has also been tested for the implementation of mechanical stimulation of the membrane, inserting a tube (1.6 mm diameter) connected to a syringe in the pierced plug.

3.1.2 Mold fabrication

Among other fabrication techniques, 3D printing was chosen for the realization of the molds because of its good throughput/quality ratio: it accelerates prototyping, allows to

customize the items, which can have variable complexity without increasing their costs, and makes the redesign process easier and faster [58].

In particular, Poly-Jet 3D printing is an Additive Manufacturing process based on the layer-by-layer addition of a photopolymer resin, which is selectively jetted onto a build-tray and immediately cured with ultraviolet lamps mounted onto the 3D printing heads [59]. Starting from a CAD model of the desired geometry, the repeated process of addition and polymerization of the resin layers allows to obtain tri-dimensional items with a dimensional resolution up to 16 microns. The quality of the final product is affected by the layer thickness, the deposition mechanism dynamics (mass, velocity, viscosity of resins used), the 3D digital model shape and the finishing method [59]. The poly-jet technique produces objects with low surface roughness, making it suitable to realize masters and molds.

The poly-jet 3D printer used in this work is the OBJET30 Stratasys (figure 23), characterized by an XY Resolution of 600x600 DPI (dots per inch) and horizontal build layers range between 16 microns and 36 microns depending on the print mode [60].



Figure 23. ChiLab OBJET30 Stratasys 3D printer.

The CAD model was converted into a STL (Standard Triangulation Language) format and imported to the Objet Studio software of the printer, where the slicing algorithm splits the 3D geometry into two-dimensional slices. In a pre-processing phase, the desired object can be pre-visualized on the construction tray of the printer. The software performs an automatic placement of the items on the tray, but each of them can be oriented by the user. After choosing the desired finish (in this work, glossy and smooth surfaces were needed) of the printed objects and confirming the validity of the

geometries on the tray, the print begins. First, some layers of a sacrificial material (SUP705) are laid out as a support that will be easy to remove from the tray. Each slice constituting the geometry is then printed with the structural resin VeroWhite™ by Stratasys, a liquid photopolymer that is immediately solidified by UV exposure. The printing process has a duration of about one hour, but it may vary with the number of items and with their complexity.

At the end of the process the objects are detached from the tray with a metal spatula. The support material at the base of each piece is removed and washed off with water. At this point, the molds undergo a thermal treatment: they are placed in oven at the temperature of 110°C for one night. This step is crucial for the successful curing of the PDMS that will be poured in the 3D printed objects for the replica molding. Indeed, PDMS curing consists in the crosslinking of vinyl-terminated oligomers in presence of a catalyst, via a hydrosilylation mechanism (addition of Si-H bonds across unsaturated bonds). Molecules with strong affinity for the catalyst can inhibit the crosslinking: these inhibiting molecules (polyethylene glycols, diethyl-phthalates, unreacted monomers, phosphineoxide photoinitiators) can be released in solution by 3D-printed objects (figure 24) [61]. Thermal and UV treatments of 3D printed molds have been proved to vaporize the remaining photo-initiators out of the structures and to promote recombination reactions between the photo-initiator and residual high molecular weight species in the resin [61].

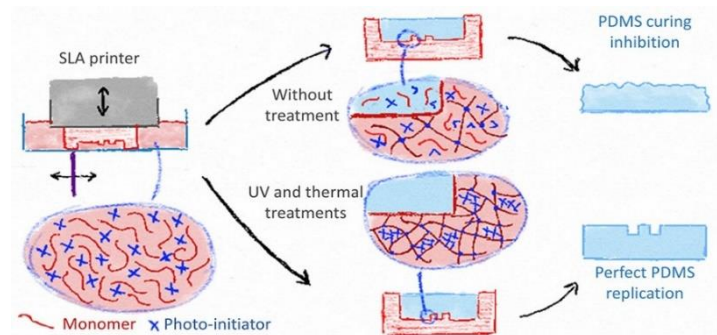


Figure 24. Free monomers and photo-initiator molecules inhibit the curing of PDMS; UV and thermal treatments of the molds avoid the interaction of these molecules with the catalyst [61].

3.2 Replica molding

The replica molding technique allows to obtain high resolution objects while being simple, rapid and versatile: the molds can be fabricated in different ways (3D printing, photolithography or laser ablation) and the viscosity of the poured solution of PDMS can be modulated, modifying the ratio between the pre-polymer and the reticulating agent. In this work, 3D printed masters were used to obtain PDMS replicas: the result is an elastic, transparent patterned layer.

3.2.1 PDMS layer fabrication

Sylgard 184 silicone elastomer was used to fabricate the layers constituting the final device.

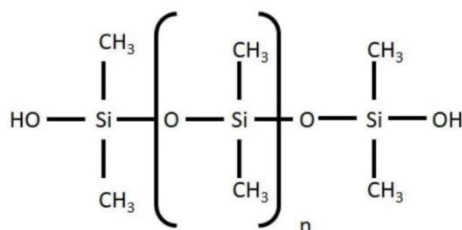


Figure 25. Chemical structure of polydimethylsiloxane.

The producer of the PDMS (figure 25) provides a polymer base and a curing agent, that were used to prepare a solution in the ratio of 10:1 weight/weight, respectively. After a manual stirring, the solution was degassed in vacuum to minimize the presence of bubbles in the molds. The viscous PDMS was poured in clean molds, that were filled avoiding the formation of a meniscus, and a new degassing step in vacuum was performed to eliminate the air trapped in the liquid layer. The molds were then placed in oven at the temperature of 90°C for 15 minutes: high temperature accelerates the reticulation of PDMS. Once removed from the oven, the replicas were ready to be peeled off their molds. After geometry check and dimensional controls, the layers were put in a falcon containing ethanol and washed in ultrasonic bath for 5 minutes, at the frequency of 49 Hz. The clean replicas were dried on hot plate at 100°C for about 10 minutes, so that the surface could be ready to undergo the plasma oxygen treatment.

3.3 Electrospinning

The last component of the chip is the scaffold: an electrospun nanofibrous mat mimicking the basement membrane of the alveolar-capillary barrier. The alveolar

basement membrane consists of elastin and collagen fibers, and it has a thickness of about 50 nm [4]: this fibrous morphology and extreme thinness can be reproduced using electrospinning, a technique suitable for the fabrication of ECM-like scaffolds characterized by fibers and pores in the sub-millimetric scale.

Electrospinning is a fiber production method based on the use of electric forces to extrude polymeric solutions (or melt polymers). After filling a syringe with the chosen material, a high voltage is applied between the nozzle of the syringe and the collector where the extruded fibers are gathered thanks to the potential difference. Different collectors can be used according to the final purpose: rotating collectors with large diameter allow to obtain aligned fibers, while small diameters are useful to create tubular fibrous scaffolds. Planar collectors give instead randomly oriented fibers, like the ones used in this work. The size and quality of the fibers depend both on the characteristics of the polymeric solutions, like viscosity, surface tension, concentration, molecular weight and structure of the polymer, evaporation rate and conductivity of the solvent, and on the process parameters, that include voltage, flow rate and distance between the needle and the collector (figure 26). Temperature and humidity of the ambient also influence the final result.

Parameter	Effect on fibre morphology
Applied voltage ↑	Fibre diameter ↓ initially, then ↑ (not monotonic)
Flow rate ↑	Fibre diameter ↑ (beaded morphologies occur if the flow rate is too high)
Distance between capillary and collector ↑	Fibre diameter ↓ (beaded morphologies occur if the distance between the capillary and collector is too short)
Polymer concentration (viscosity) ↑	Fibre diameter ↑ (within optimal range)
Solution conductivity ↑	Fibre diameter ↓ (broad diameter distribution)
Solvent volatility ↑	Fibres exhibit microtexture (pores on their surfaces, which increase surface area)

Figure 26. Influence of solution and process parameters on the morphology of the electrospun fibers [68].

The electrospinning instrument used to fabricate the membranes is the Novaspider V5 (figure 27). The machine is equipped with a syringe pump, a plane collector, electrodes, and a gear system that keeps the needle perpendicular to the plane of the collector

while moving it along the x, y and z axes. The process parameters can be monitored and controlled in real-time through an interface on a touch screen panel.



Figure 27. Novaspider V5 elettrospinning instrument in Polito^{BIO}Med Lab.

3.3.1 Membrane fabrication

The material chosen to realize the scaffold of the alveolus-on-chip is a PCL/gelatin blend. This combination of a synthetic and a natural polymer was optimized in a previous work by Giuntoli *et al.* [62]. In the thesis work by Eleonora Palumbo *et al.* [52] a comparison between PCL alone and PCL/Gel blend membranes was performed, by characterizing the morphological, mechanical and biological properties of the mats. The results showed that the blend produces fibers and pores with smaller diameter compared to PCL membranes. On the other hand, cyclic uniaxial mechanical tests highlighted that the addition of gelatin to the working solution increases the Young modulus of the fibers, reducing the elasticity of the material. Overall, the PCL/Gel blend was considered a good compromise between the bioactivity properties of gelatin and the fatigue resistance of PCL. PCL is indeed a biodegradable but hydrophobic semi-crystallin polyester, obtained by ring-opening polymerization of cyclic monomer ϵ -caprolactone. Its advantageous mechanical properties are also linked to its slow degradation process via hydrolysis, that produces biocompatible waste molecules. Instead, gelatin is a natural polymer obtained from the partial hydrolysis of collagen; its macromolecules are therefore constituted from amino acids like hydroxyproline, glycine, and proline that favour adhesion,

migration and cell proliferation. Still, gelatin is water soluble if not crosslinked. In this work, gelatin was stabilized by crosslinking using (3-Glycidyloxypropyl) trimethoxysilane (GPTMS), a silane coupling agent whose oxirane rings react with the amino groups of the gelatin, forming pendent silanol groups. During the fibers extrusion, the solvent

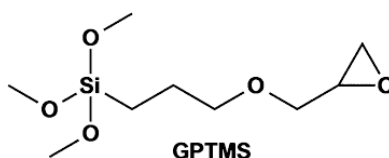


Figure 28. Chemical structure of (3-Glycidyloxypropyl) trimethoxysilane (GPTMS).

evaporates and Si-O-Si bonds between gelatin macromolecules are formed thanks to condensation reactions of two silanol groups.

In this work, PCL and gelatin were added in 80/20 weight/weight ratio in 5 mL of acetic acid and formic acid (50:50 ratio), obtaining a solution 15% w/v. After 24 h of stirring in a glass beaker at room temperature at 200 rpm, the reticulating agent GPTMS (3,68% (v/v)) (figure 28) was added to the PCL/Gel solution, that was stirred again for 30 minutes and then moved into the syringe. The 5 mL of solution were extruded under a constant flow rate of 500 $\mu\text{L}/\text{min}$, setting a 12 cm distance between the nozzle and the collector and a potential difference of 21 kV, adopting the parameters combination optimized in the work aforementioned [52].

3.3.2 Membrane characterization

The morphology of the electrospun fibers was analysed with the scanning electron microscopy (SEM, Tescan Vega) Zeiss SUPRA 40. Scanning electron microscopy is a high-resolution technique based on the emission of secondary electrons by the sample, thanks to a high energy focused electron beam. The beam is produced accelerating primary electrons produced by an electron gun with a voltage of 1-30 kV, and it is focused on the specimen in the vacuum chamber by a set of electromagnetic lenses. In order to emit secondary electrons, the samples must be conductive: they are usually sputter-coated with a thin platinum layer before the analysis.

In this study, SEM was used to evaluate the effects of thermic treatments on the morphology of the fibers of the PCL/Gel membrane. Indeed, according to literature [53],

plasma treatment and chip assembling should be followed by a brief treatment at high temperature, that consolidates the chemical bonding between the PDMS layers. Before the SEM analysis, the membrane sample was placed on a stub - codified to identify the sample - and sputter-coated with a conductive metal.

3.4 Device assembling

The electrospun membrane mats were cut with a 5 mm diameter puncher to obtain circular scaffolds of controlled dimension. Each circular membrane was handled with tweezers and placed over the culture chamber of the clean PDMS bottom layer. At this point, the plasma treatment was performed.

3.4.1 Plasma treatment

Plasma oxygen has been used to activate the surfaces generating reactive chemical groups for covalent bonding between two PDMS layers.

The terminal methyl groups ($-CH_3$) in PDMS (generally comprised of repeating units of $-O-Si(CH_3)_2-$) can be replaced by silanol groups ($Si-OH$). Being strongly polar groups, these make the surface hydrophilic and can condense with a similar silanol group on another activated surface, forming covalent siloxane bonds ($Si-O-Si$) after the loss of a water molecule [63].

The process was performed with the Atto plasma system by Diener electronic (figure 29), and it consists in four phases, whose parameters have been optimized specifically for the PDMS activation.

- After placing each PDMS replica in the chamber, exposing upwards the surface to be functionalized, the door is closed and sealed. During the pumping down, the pressure inside the chamber is lowered to 0.3 mbar.
- Oxygen is then pumped in the chamber for one minute with a pressure of 0.7 mbar.
- The actual plasma process lasts 30 seconds: the high frequency generator is activated with a power of 22%.

- During the final venting phase, the chamber is filled with air and the atmospheric pressure is restored.



Figure 29. ChiLab Atto plasma system by Diener electronic.

When the machine notifies the end of the process, the door can be opened.

The layers were assembled matching each top layer over a bottom layer hosting its membrane, and each reservoir over the top layer, applying a light pressure. The assembling was followed by a 10 minutes thermic treatment at 70°C on hot plate, in order to improve the adhesion.

3.4.2 Microfluidic tests

Once the three-layers device was completed, leakage tests were performed in static and dynamic conditions injecting a solution of water and food dye. The digital microscope Leica DVM 2500 was used to evaluate the results of the static tests and to monitor and record the dynamic tests, in which a syringe pump was set on a flux of 60 $\mu\text{L}/\text{h}$ and connected to the inlet of the chip through a tube with a 1.6 mm diameter. Both the testing conditions were useful to assess the adequacy of the shape of the inlets, the tightness of the seal between the bonded PDMS layers, the fluidic resistance of the serpentine and the effects of the fluid pressure on the nanofibrous membrane.

3.5 Cell culture

The A549 cell line (adenocarcinomic human alveolar basal epithelial cells, ATCC) was chosen to model the alveolar epithelium due to its type II alveolar epithelial cells phenotype, involving presence of polarization, tight junctions and cytoplasmatic extension [64]. In this work, cells were grown in RPMI 1640 medium (Gibco,

ThermoFisher scientific) characterized by the presence of the reducing agent glutathione and high concentrations of vitamins. The RPMI was supplemented with:

- 10 % fetal bovine serum (FBS, Gibco ThermoFisher scientific), that provides essential growth factors for cell maintenance and vitality;
- 1% L-glutamine 200 nM (Gibco, ThermoFisher scientific), an aminoacid that supports the growth of rapidly dividing cells with high energy demands and synthesizing large amounts of proteins and nucleic acids (as in the case of A549 cells) [65];
- 1% penicillin streptomycin (P/S, Gibco, ThermoFischer scientific), antibiotics used to prevent bacterial contamination.

The alveolar endothelium was modelled using immortalized neonatal lung microvascular endothelial cells (HULEC-5a). The cells were grown in MCDB 131 medium (Gibco, ThermoFisher scientific), that was supplemented with:

- 10 µg/mL epidermal growth factor (EGF);
- 1 µg/mL hydrocortisone, supporting cell growth and differentiation;
- 10 mM glutamine;
- 10% fetal bovine serum (FBS);
- 1% penicillin streptomycin (P/S);

In order to perform the co-culture, the cells were thawed and put into culture in 75 cm² flasks at 37°C in a humidifier incubator, with 5% CO₂ in air. When confluence was reached, the cells were detached from the flask: after removing the waste medium and rinsing with 5 mL of PBS (posphate-buffered saline, pH ~ 7.4), the cells were incubated for 3 minutes with 2 mL of trypsin, an enzyme promoting the detachment. At this point, the cells were checked under the microscope to confirm the success of the procedure: if floating cells were visible, trypsin was inhibited with 5 mL of culture medium. A Neubauer counting chamber was used to perform the cell count, using 10 µl of the resulting cell suspension. The sum of the number of cells counted in each square was averaged for the number of squares, multiplied by the volume of cell suspension (7 mL)

and by 10000, a constant factor. The result is an estimate of the total number of cells in the suspension. This information was used to calculate the volume of cell suspension containing the number of cells needed for the seeding. This number was obtained multiplying the wanted cell density by the available surface on the culture substrate. This area was calculated from the diameter of the membranes, which were cut out using a 5 mm diameter puncher ($A=0,196 \text{ cm}^2$).

Cell density on the membrane was optimized in the cited work by Eleonora Palumbo [52], where confluence condition and cell viability on the PCL/Gel membrane were tested at different times and with different initial cell concentration.

3.5.1 Seeding protocol

Before seeding, every microfluidic chip was sterilized by 30 minutes of UV exposure on each side and by overnight incubation with a solution of PBS, antibiotic and antifungal. The sterilizing solution was then removed and the channels were rinsed with PBS. HULEC-5a were seeded on the lower part of the electrospun membrane, with a wanted density of $16 \times 10^4 \text{ cells/cm}^2$. Using a micropipette, $10 \mu\text{L}$ of cell suspension was placed in the culture chamber of the bottom layer of the chip through the dedicated inlet channel. The chip was placed upside down, allowing gravity to favour the adhesion on the membrane. Before being placed in the humidifier incubator at 37°C , drops of PBS were added to each petri dish containing the seeded chip with the aim of preventing the untimely evaporation of the medium. The microfluidic serpentine were filled with medium 4 hours after the seeding to nourish the endothelial cells. For the adhesion phase of the HULEC-5a, two different approaches were tested: the cells were allowed to adhere for 4 hours (figure 30, test 1) or for 24 hours (figure 30, test 2 and 3) before the addition of the A549 cells.

A549 cells were seeded on the membrane to obtain a density of $14 \times 10^4 \text{ cells/cm}^2$. A drop of $10 \mu\text{L}$ of cell suspension was placed on the upper part of the membrane, and after 1 hour of adhesion in the incubator $200 \mu\text{L}$ of medium were added in the reservoir. Endothelial and epithelial cells media were changed every 24 hours, and 72 hours (figure 30, test 1 and 3) or 48 hours (figure 30, test 2) after A549 cells seeding, the medium in the top layers reservoir was removed, ending the submerged condition and exposing

the epithelial layer to air to implement the air-liquid interface (ALI) across the membrane.

Each test ended seven days after ALI implementation. In order to choose the optimal protocol for cell adhesion and long-term viability, the culture was interrupted at established time points to analyse the status of the barrier model (figure 31).

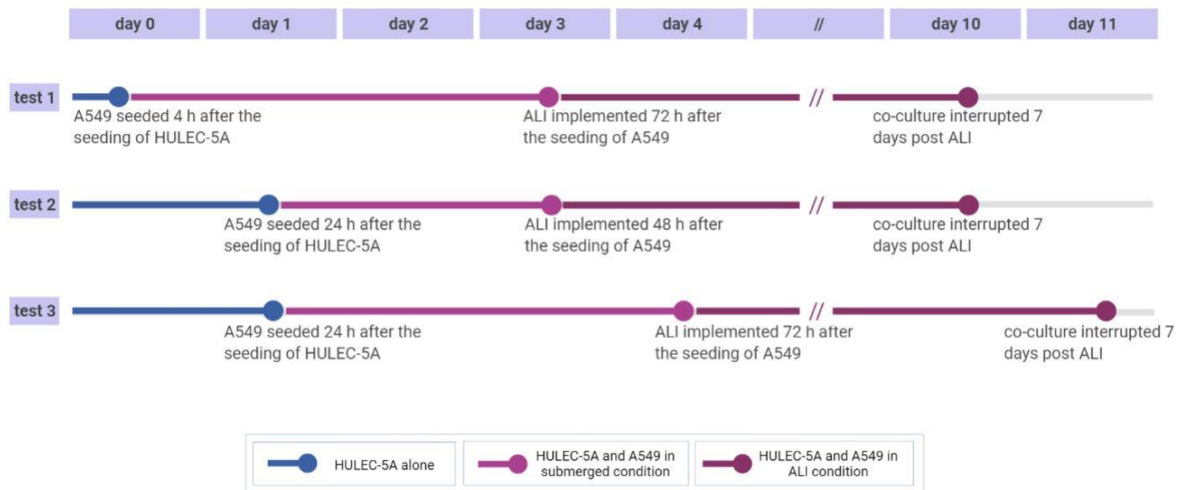


Figure 30. Timeline for the cell seeding and co-culture experiments. Created with BioRender.com

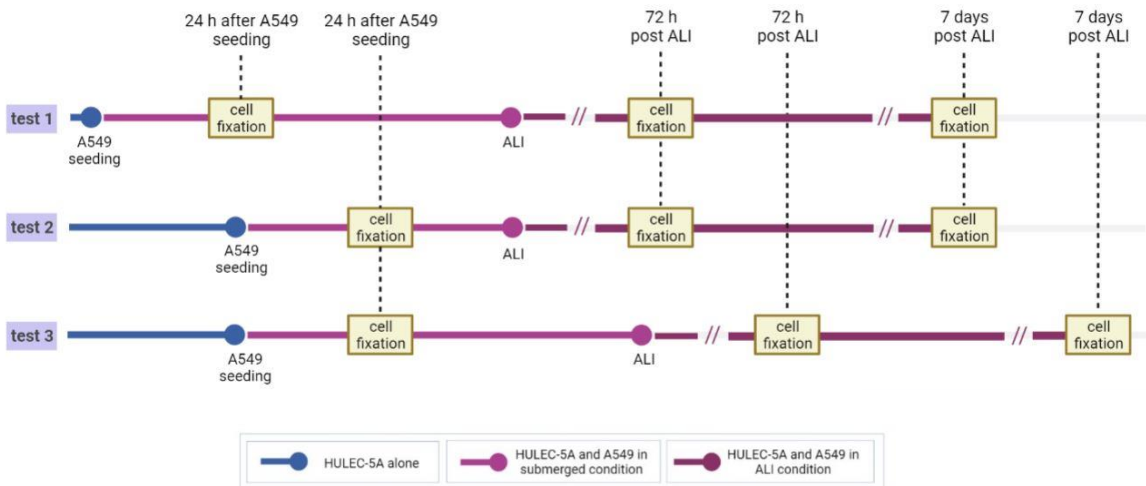


Figure 31. Time points for the cell fixation for the evaluation of the optimal co-culture protocol. Created with BioRender.com

3.5.2 Fluorescence imaging

DAPI and phalloidin staining were performed to evaluate the presence of adhered cells and their morphology on both sides of the PCL/gel membrane. To do so, after medium removal from the chip and PBS wash, the channels were filled with 4%

paraformaldehyde (PAF), which fixates the cells inducing the creation of covalent bonds between proteins, making the sample insoluble. At the end of the 40 minutes incubation time, the samples were washed in PBS. In order to allow the staining molecules to enter the cells, the cellular membranes need to be permeabilized with 0.5% TRITON-X in PBS for 5 minutes. After a PBS wash, the blocking of excess protein-binding sites was performed with 1% (w/v) bovine serum albumin (BSA, Sigma-Aldrich) in PBS for 1 hour. At the end of this phase, the channels were filled with a solution of 1% BSA and Fluorescein Isothiocyanate Labeled Phalloidin (FITC-phalloidin, ThermoFisher)(figure 32, A) – or Tetramethylrhodamine B isothiocyanate Phalloidin (TRITC-phalloidin, excitation at 540–545 nm, emission at 570–573 nm) – in the ratio of 1:60. Phalloidin selectively binds to polymeric F-actin, with low non-specific binding; the conjugated FITC provides green fluorescence allowing to evaluate the morphology of the cytoskeleton and the distribution of its actin filaments (excitation at 495 nm, emission at 513 nm). The samples were kept in the dark during the 40 minutes of incubation with the phalloidin solution. After rinsing the samples with PBS, the staining of the nuclei was performed with a solution 1:1000 of DAPI (diamidino-2-phenylindole)(figure 32, B) in PBS. DAPI is a blue fluorescent probe that, when selectively bound to AT sequences of DNA, shows a fluorescence approximately 20-fold greater than in the non-bound state. The samples were incubated in the dark with the stain for 5 minutes, and then washed with PBS.

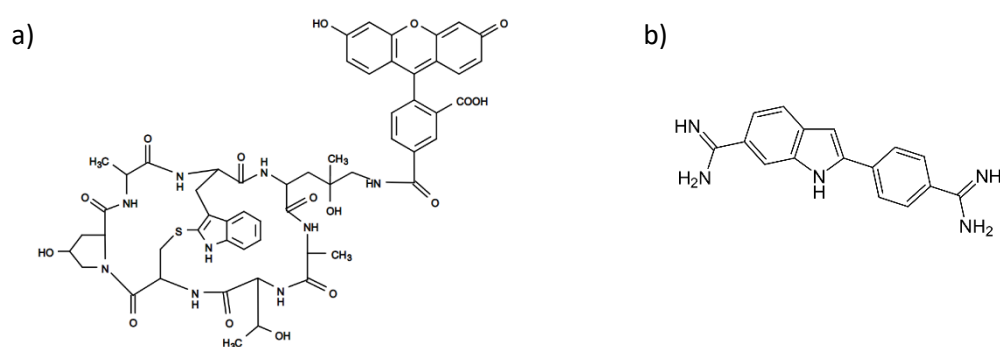


Figure 32. Chemical structure of (a) FITC-phalloidin and (b) DAPI.

At this point, the PDMS devices were disassembled to harvest the fixed membranes. Each membrane was placed between two thin glass slides with a drop of mounting media for fixed-cell imaging, that helps preserving the samples for long-term storage,

and labelled to identify the cell type on the two sides of the slides and the fixation time point.

The samples were observed with the Bio-Rad ZOE Fluorescent Cell Imager and, for higher resolution images, with the Nikon eclipse Ti2 confocal laser scanning. These equipments allow to obtain images isolating a fluorophore by using light at a specific wavelength, and the resulting different colour channels were later merged using the software ImageJ.

3.5.3 Immunostaining

To evaluate the barrier function of the multi-layered model, immunofluorescence staining was performed with the aim of detecting the expression of E-cadherin (epithelial cadherin), VE-cadherin (vascular endothelial cadherin) and ZO-1. Cadherins are calcium-dependent transmembrane proteins that contribute to the formation and maintaining of adherens junctions, with the role of stabilizing cell-cell contact. Zonula occludens-1 ZO-1 (Tight junction protein-1) is a scaffolding protein whose role is fundamental in the formation of tight junctions, which mediate the paracellular passage of ions and solutes between cells [66].

The staining protocol started with cell fixation (PBS wash of the samples, 40 minutes incubation in 4% PAF, PBS wash). After permeabilization with 0.2% v/v TRITON-X in PBS for 5 minutes, the unspecific binding sites were blocked with 2% BSA solution in PBS for an hour. At this point, the samples were ready for overnight incubation at 4°C with solutions of primary antibodies in PBS, 1% v/v BSA and 0.1 % v/v Tween 20. The same solution was used to wash the samples the following day, and to dilute the secondary antibodies for 1 h incubation at room temperature.

3.5.4 Permeability test

The apparent permeability of the barrier model was attested using FITC-dextran (Appendix II), which is a diffusible molecule (a polymer of anhydroglucose) useful to create concentration gradients and to perform fluorescence imaging for barrier function analysis, thanks the conjugated FITC molecule.

A solution of 2 ml of HULEC-5a medium and FITC-dextran was prepared with a concentration of 1 mg/ml, and filtered. At 7 days post ALI, three cultured devices were

removed from the incubator and rinsed with PBS++; 100 μL of HULEC-5a medium were refilled in the bottom layer, and 30 μL of FITC-dextran solution were placed on the upper part of the membrane in the top layer's central hole. The same procedure was performed on three sterilized devices that weren't subjected to cell culture, acting as acellularized membrane controls. After 1 hour of incubation, the FITC-dextran solution was removed from the apical side. The 100 μL of medium were then removed from the bottom channels, and a sample of 2 μL was placed on a microvolume plate. The microplate reader BioTek Synergy HTX Multimode Reader was used to obtain fluorescence values of the samples. Using a calibration curve, obtained from 5 standard FITC-dextran solutions' concentrations and their correspondent fluorescence values, the molecule concentration in each sample was calculated. The apparent permeability was obtained multiplying the concentration for the volume of harvested medium (0.1 mL) and then dividing for the product of 3600, the membrane area (0.196 cm^2), and the initial concentration of the FITC-dextran solution (1 mg/ml), and ultimately mediating the three values for the samples with the co-culture and for the controls.

4. Results and discussion

4.1 Design-experiment cycle: the iterative process towards the final device

The process of optimization and adjustment that led to the final device (that, in the following paragraphs, will be referred to as ‘Tesla valve-design’) was based on the evaluation of the results of 3D printing tests, leakage tests and cellular tests, that were reiterated after every design modification (figure 33). The baseline for the device design was the alveolus-on-chip by Eleonora Palumbo [52]. This platform was characterized by a central channel for medium flow, accessible from the top layer, with a culture chamber in which 10 micropillars supported the electrospun membrane. As mentioned in the 2nd chapter, this configuration resulted problematic during the cellular tests, and was therefore modified in the present work, starting from the position of the inlets and the channels geometry.

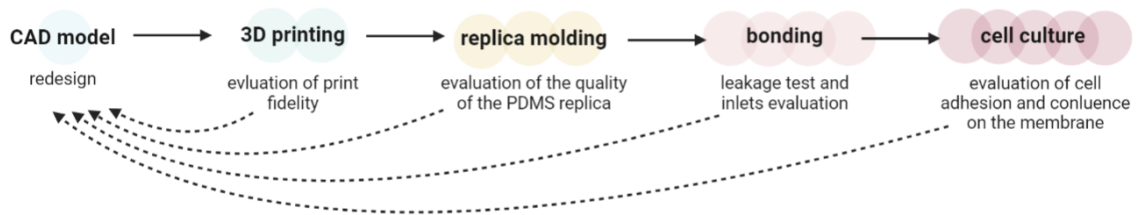


Figure 33. The work cycle, from design to cells experiments, whose reiteration led to the final device configuration. Created in BioRender.com

4.1.1 From 10 to 4 pillars

The first CAD model realized in the present study included two lateral serpentines and a culture chamber hosting 10 micropillars, having the same nominal dimensions of the pillars of the former device: a diameter of 200 μm and height of 350 μm (figure 34).

The 3D printing of this CAD model revealed that the aspect ratio wasn't adequate for the chosen fabrication technique: during the printing, the 10 micro-holes that would have originated the PDMS pillars were obstructed by the liquid resin, causing the PDMS replica resulting from the 3D printed mold to present a nearly flat surface or bumps not suitable for membrane support (figure 34).

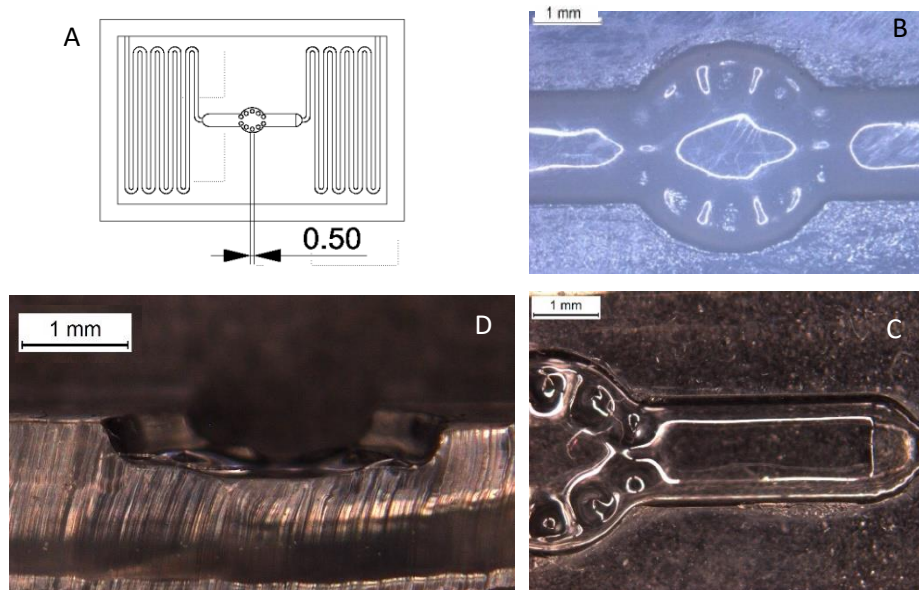


Figure 34. CAD model (a), detail of the culture chamber of the 3D-printed mold (b) and the resulting replica (c, d) of the first design of the bottom layer realized in this work, whose lack of functional pillars led to dimensional modifications.

In the subsequent printing tests the nominal diameter of the holes and their reciprocal distance were progressively increased, but without significant progress in the results.

The design was ultimately modified following two approaches: the first option consisted in substituting the pillars with two arched supports (Appendix III, B), the second one consisted in reducing the number of pillars to 4, placing them at the corners of the channels affluent to the chamber (Appendix III, C). At the same time, the microfluidic serpentes were arranged to maximize the volume of fluid that the chip could host during the static condition of the cell culture. The printing tests helped to define a minimum distance between the elements of the pattern in order to obtain defined edges (about 50 μm). A short channel connecting the culture chamber to an additional inlet was implemented with the aim of bypassing the long serpentes, and it was designed as a direct access to the membrane for endothelial cells seeding, requiring a

smaller volume of cell suspension compared to the volume needed to fill the serpentine.

The 3D printed molds and the PDMS replicas obtained from them were checked under the microscope to evaluate the fidelity to the nominal dimensions: tendentially, the solid elements of the molds pattern resulted some tens of μm bigger than the CAD model quote, probably due to the small delay between the liquid resin layer deposition and its UV curing and reticulation; as a consequence, the voids in the pattern of the replicas resulted some tens of micrometres bigger than the nominal dimensions (figure 35).

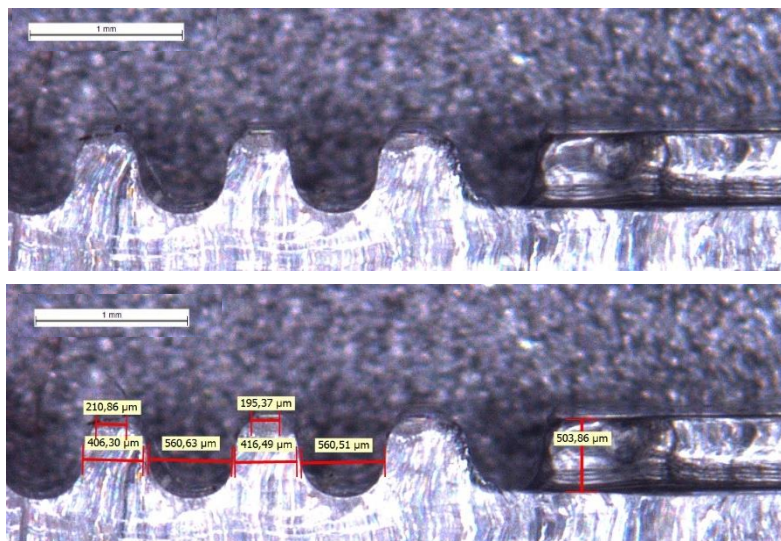


Figure 35. Section of the microfluidic serpentine of a PDMS replica obtained from a mold of the first design, having nominal dimensions of width, height and reciprocal distance of $500 \mu\text{m}$.

Leakage tests were performed to evaluate the quality of the sealing after the plasma bonding process. The injection of coloured water, through tubes having diameter of 1.6 mm, at different flow rates controlled by a syringe pump, highlighted that a successful bonding required a frame a few millimetres wide of plain PDMS surrounding the microfluidic pattern, in order to provide enough surface to secure the sealing.

At this point, the device was tested with the cell co-culture. This experimental phase allowed to identify three main problems: the culture medium passage was made difficult by the serpentine microfluidic resistance; the cylindrical geometry of the inlets wasn't optimal for the use of a micropipette; the electrospun membrane resulted too thin to be handled without being disrupted after the disassembling of the device for microscopy analysis.

4.1.2 Inlets geometry optimization

Given the issues highlighted during the latest test, the design was modified reducing the total length of the microfluidic channels, increasing the width of the serpentine by 100 μm , increasing their depth from 350 μm to 500 μm and their reciprocal distance from 500 μm to 700 μm , with the aim of reducing the microfluidic resistance (Appendix III, E). For the same reason, the 4 pillars were preferred to the two arches as membrane supports, since this last option could have contributed to obstruct the fluid flow and was not pursued in further tests.

The inlets were shaped to fit the conic format of the micropipette tips used during cell cultures. After some prints and microfluidic tests, the inlet dedicated to endothelial cells seeding was ultimately dimensioned according to the size of 20 μL tips, and the inlets accessing to the lateral serpentine were dimensioned according to the size of 200 μL tips (Appendix III, E). Custom plugs were designed to fit the inlets and seal the channels when needed (figure 20).

Also, different thickness values for the PDMS layers were subjected to tests: the optimal value was attested to be 2 mm, since thinner layers happened to break during the disassembling, making the harvesting of the membrane problematic in view of microscopy analysis. At this point, new nanofibrous mats were electrospun, increasing the spinning time from 20 minutes to 30 minutes, in order to obtain membranes thick enough to stay integer during the procedure of harvesting from the device after cell culture.

During the following cellular tests, the conic inlets and the thicker membrane were validated and their functionality was confirmed. The HULEC-5a seeding method on the lower part of the membrane was set comparing the results of adhered cells staining, with DAPI, on the membranes seeded through the lateral channels (figure 36, A) and through the central inlet (figure 36, B). Microscopy images show that cells tended to distribute more uniformly when smaller suspension volumes through the central inlet were used. In the following experimental phases, the microfluidic channels still showed resistance and resulted difficult to fill. Indeed, once flowing through the first set of serpentine, the cell medium filled the culture chamber and the central hole of the top layer, but didn't move to the second set of channels. This forced the endothelial cells to

medium shortage during the culture period, and the results of the fluorescence imaging gave no evidence of presence of endothelial cells at 7 days post ALI.

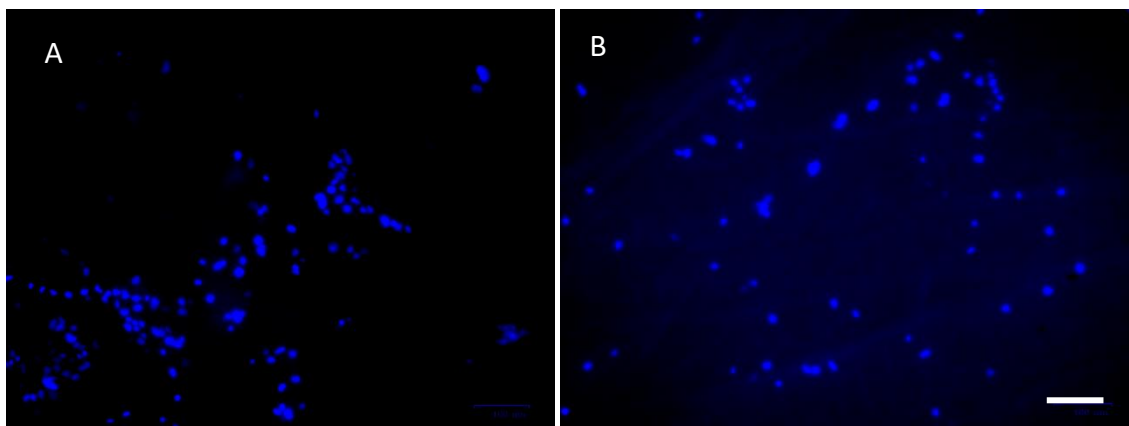


Figure 36. Staining with DAPI of HULEC-5a. Evaluation of cell adhesion on the electrospun membrane 4 hours after seeding, using two different seeding approaches. a) Seeding performed introducing 100 μL of cell suspension in the microfluidic channels through the lateral inlet. b) Seeding performed introducing 10 μL of cell suspension in the culture chamber through the central inlet directing accessing the membrane. Scale bar is 100 μm .

4.1.3 Culture chamber's depth increment

The device was once again redesigned, this time starting from the culture chamber configuration. In the attempt of ensuring the retaining of culture medium beneath the membrane to nourish the endothelial layer, the depth of the circular culture chamber was increased to 1 mm, surrounded by the 600 μm deep affluent channels. This modification in culture chamber depth required an increase in the pillars' diameter to 700 μm in order to obtain well defined and high enough membrane supports.

At the same time, addressing the problems experienced with the medium flow, the microfluidic channels were rearranged eliminating the second set of serpentine: the culture chamber was moved on the side of the pattern, reducing the inlets from 3 to 2 (Appendix IV).

After verifying cell adhesion on the membrane through staining with DAPI 72 hours after seeding (Appendix V), the co-culture performed on the described design was stopped and fixed at 7 days post ALI. The staining with DAPI and rhodamine showed the presence of only a few cells, demonstrating that the endothelial cells did not reach the confluence condition (Appendix V).

4.1.4 Pillars diameter optimization

The hypothesis that guided the final redesign was that, given the results of the latest cellular experiments, the PDMS membrane-support pillars influenced cell migration and survival, hindering the reach of a confluent endothelial layer. However, it was previously demonstrated that, in absence of support structures in the culture chamber of the bottom layer, the wet electrospun membrane distinctly bends and curves under its own weight, as shown in the microscopy image of the section of a test-device (figure 37, A), obtained from a mold in which the 3D printer failed to create holes defined enough to produce pillars in the PDMS bottom layer. This was considered suboptimal, and the presence of pillars was attested as necessary.

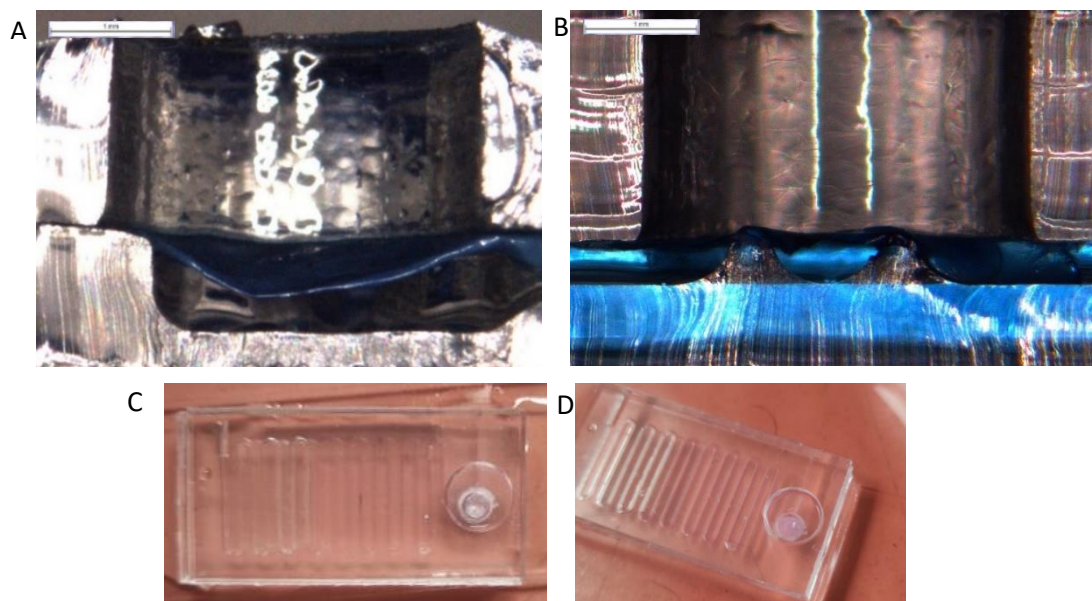


Figure 37. a, b) Section of complete PDMS devices in correspondence to their culture chamber and suspended membrane, in absence (a) and presence (b) of support pillars, after a microfluidic test with blue food dye. c, d) One of the devices subjected to the microfluidic test, before (a) and after (b) the 24 hours incubation. Scale bar is 1 mm.

In light of these evaluations, new print tests were performed to reduce the diameter of the pillars and to separate them from the center of the membrane, with the aim of decreasing their impact on cell activity. After failing to print 500 μm holes, the optimal nominal diameter to obtain well defined and space-saving supports was found to be 600 μm .

The modified layout (Appendix III, F), that will be referred to as “one-serpentine-design”, characterized by two inlets, a single set of serpentines, 1 mm deep culture chamber and 4 pillars with the optimized nominal diameter of 600 μm in the bottom layer, was tested with cell medium, before cell seeding, to evaluate the quality of the sealing and the microfluidic resistance of its channels (figure 37, C, D). The samples, placed in a petri

dish containing PBS, were easily filled with medium and incubated in an oven at 37°C to simulate the temperature condition of a cell incubator. After 24 hours, the presence of liquid in the serpentine confirmed the ability of the device to preserve the medium without drying out or affecting the bonding. However, the samples showed medium rising on the upper side of the membrane (figure 37, D).

The following cell culture on the one-serpentine-devices showed, as expected in light of the previous microfluidic test, that ALI was affected by liquid level rising in the top layer hole. However, the experiment was useful to validate the new configuration of the support pillars.

HULEC-5a on the lower part of the membrane showed presence of adhered cells on the most part of the membrane and cytoskeletons spread morphology (figure 38, A-F). However, the endothelial layer did not reach complete confluence, differently with respect to the epithelial layer (figure 38, G-I).

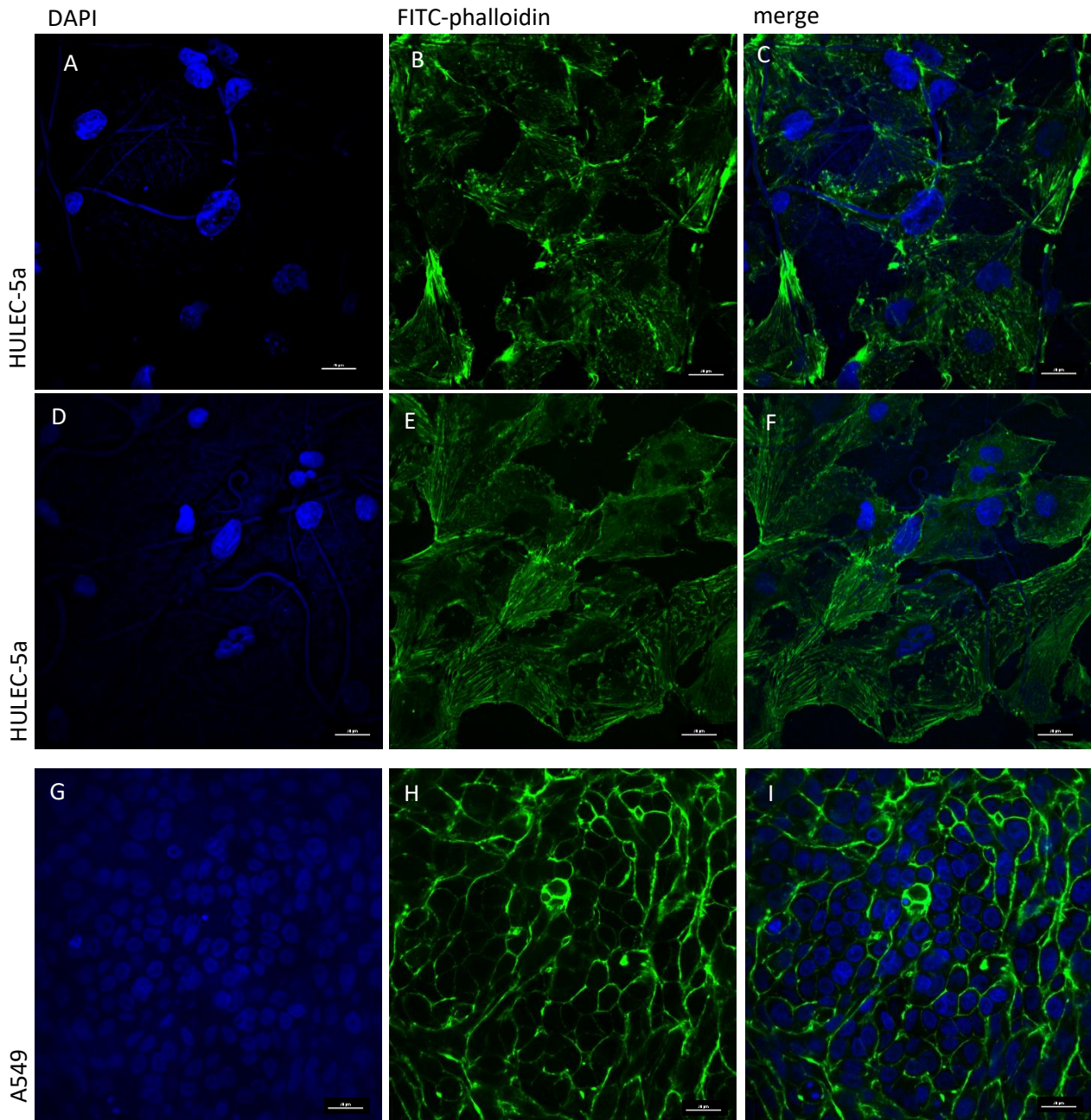


Figure 38. Confocal laser scanning images of HULEC-5a (A-F) and A549 (G-I), in one-serpentine-device, after fixation and staining with DAPI (A, D, G) and phalloidin (B, E, H). The images of both color channels and their merge (C, F, I) is shown. Scale bar is 20 μm .

4.1.5 Tesla valve implementation

While optimizing the features of the membrane supports, a new strategy for the microfluidic channels' geometry was evaluated. Using Rhinoceros, on the basis of

literature works [55] [57], a one-way passive valve inspired to Tesla’s original patent [54] was designed to be included in the device, for the purpose of facilitating the medium flow through the channels, taking advantage of its direction-dependent fluidic resistance. A valvular conduit was inserted before and after the culture chamber in the bottom layer and connected with two sets of serpentine, on the left and on the right side of the center respectively (figure 20) (Appendix III, G). The culture chamber was designed including the previous modifications that were proved to improve the results of cell cultures (1 mm depth, distanced and thinner support pillars).

4.2 Tesla valve-design validation

4.2.1 Device characterization

Adopting the functional features and the aspect ratio optimized during the testing of the above-mentioned device’s preliminary versions, the Tesla valve-design (figure 20, 21, 22) didn’t present issues during the printing phase (Appendix VI).

Microscopy images of the PDMS replicas resulting from the bottom layer mold show that, as expected, the measures differ from the nominal dimensions of the CAD model of some tens of micrometers: the PDMS pillars diameter results smaller than 600 μm (figure 39, A).

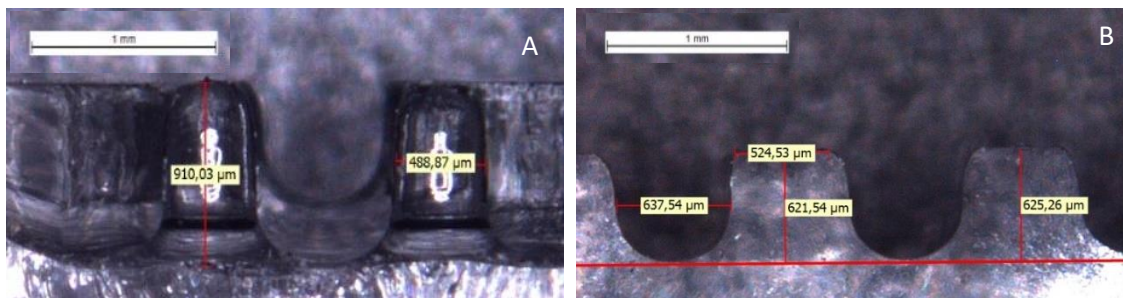


Figure 39. a) Section of the bottom layer replica in correspondence to its culture chamber, showing two of the four support pillars. b) Section of the bottom layer replica in correspondence to the microfluidic serpentine, having nominal dimensions of 600 μm width, 600 μm height and reciprocal distance of 700 μm .

Microfluidic tests (figure 40) validated the bonding process, showing no leaking or layers separation. The function of the PDMS plugs was attested as well, and the liquid injection displayed a promising functioning of the pattern and good fluid flow through the channels, with lower tendency to be subjected to liquid level rising above the central membrane compared to the previous layouts.

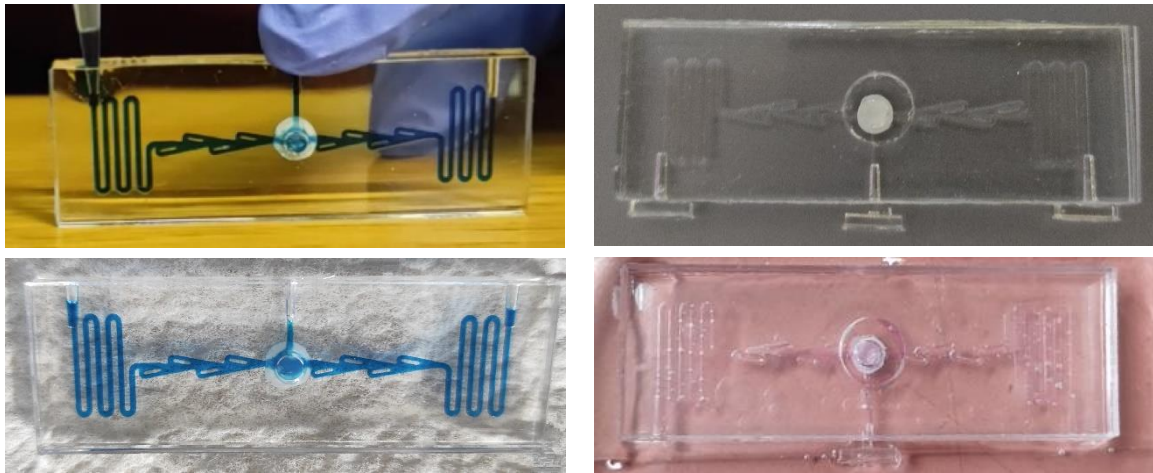


Figure 40. On the left: evaluation of the quality of the plasma-bonding between bottom and top layer, using a micropipette and food dye diluted in water. On the right: a complete device (bottom, top and reservoir layers) with its sealing plugs inserted in the inlets, before (upper image) and after (lower image) a 24 hours incubation with cell medium, in an oven at 37°C.

To evaluate the effects of the thermal treatment at 70°C on the electrospun membranes, to which the devices were subjected after plasma-bonding in order to consolidate the interlayer adhesion, samples of membrane were taken from the chips after the process and analysed through SEM. The images (figure 41) showed that, overall, the membrane presents some defects (a few beads and micrometric filaments) generated during the electrospinning process, but the morphology of the fibers wasn't affected by the high temperature treatment.

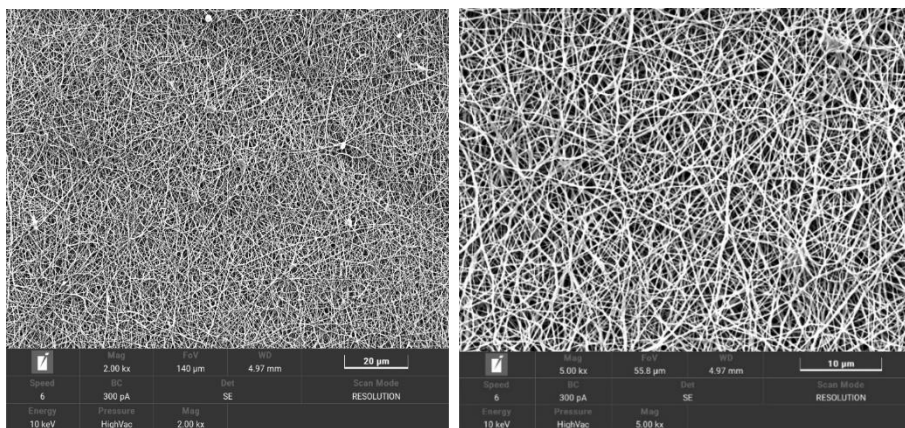


Figure 41. SEM images of a sample of membrane treated at 70°C for 10 minutes after the plasma-bonding.

4.2.2 Cellular tests

In the cellular experiments that followed, the Tesla valve-design performed better than one-serpentine-devices and appeared to be less subjected to medium rising in the upper part of the membrane compared to the previous designs.

A volume of 10 μL of HULEC-5a and cell medium was inserted in the culture chamber of the bottom layer via central inlet, to obtain a cell density of $16 \times 10^4 \text{ cell/cm}^2$ on the membrane. The same volume of cell suspension was used to seed A549 on the apical part of the membrane with a density of $14 \times 10^4 \text{ cell/cm}^2$ [52]. For the realization of the co-culture, two approaches were applied: in half of the prepared devices, HULEC-5a were allowed to adhere for 4 hours in the incubator before the seeding of A549 on the opposite side of the membrane; in the other half of the devices, HULEC-5a were allowed a 24 hour-incubation time before the seeding of the epithelial cells. Results show that 24 hours-adhesion time allows the endothelial cells to colonize the membrane homogeneously and to reach confluence at 7 days post ALI (figure 42, D-F), whereas the 4 hours-adhesion time results in a more inhomogeneous colonization of the membrane, as demonstrated by the presence of acellularized spots (figure 42, A-C) (Appendix VII). However, the A549 subjected to only 48 hours of submerged culture after seeding

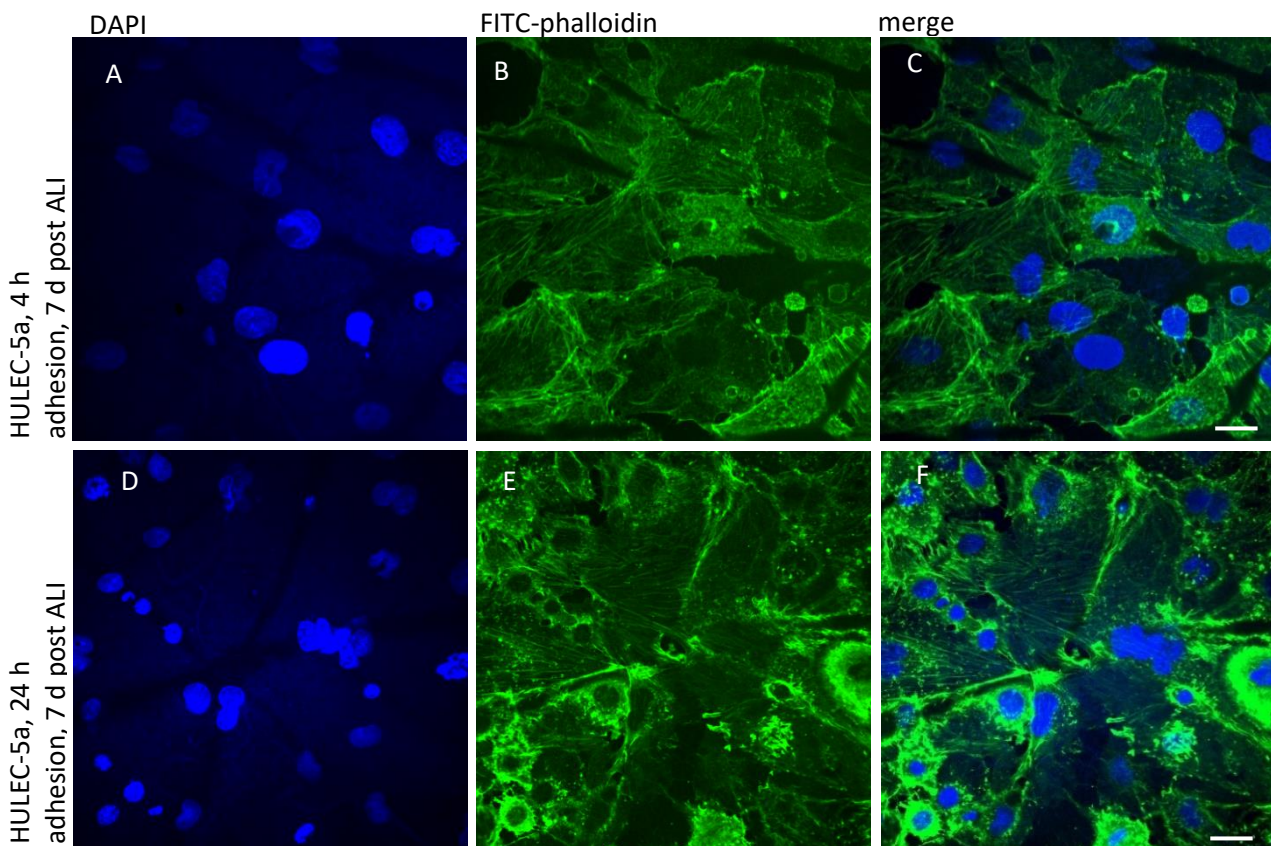


Figure 42. Confocal laser scanning images of HULEC-5a (A-F), in Tesla valve-devices, after fixation and staining with DAPI (A, D) and phalloidin (B, E). The images of both color channels and their merge (C, F) are shown. Scale bar is 20 μm .

appeared to form a less confluent layer, 3 days after ALI, than the A549 in which ALI was implemented 72 hours after seeding (figure 43). Therefore, it was attested that the optimal protocol included 24 hours-adhesion time for HULEC-5a, and, after that, 72 hours of submerged co-culture before exposing A549 to air.

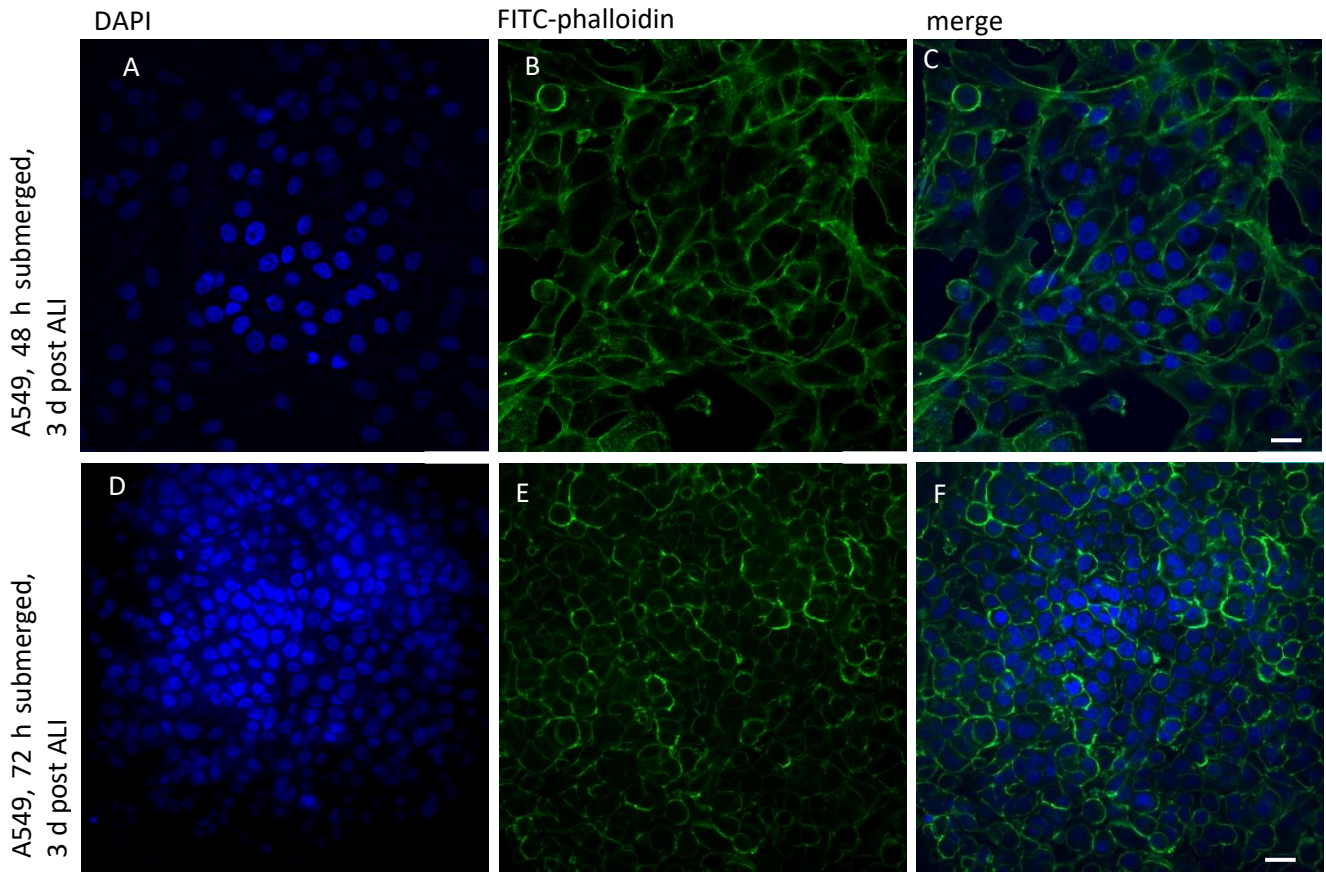


Figure 43. Confocal laser scanning images of A549 (A-F), in Tesla valve-devices, after fixation and staining with DAPI (A, D) and phalloidin (B, E). The images of both color channels and their merge (C, F) are shown. Scale bar is 20 μm .

4.2.3 Permeability test

Barrier function of the multi-layered model was evaluated comparing the permeability of 7 days-post-ALI co-cultures and acellularized control membranes. After 1 hour incubation with FITC-dextran, placed in the apical part of the devices, the cell medium was taken from the microfluidic channels of the bottom layer and a sample of 2 μL was placed in the plate for fluorescence reading. Apparent permeability resulted to be higher in the no-cells-controls, and lower in the samples from the cellularized devices (figure 44): the presence of the cellular layers on the two sides of the membrane reduces the

permeability of the interface. The junctions between the cells reduce the ability of solutes and small molecules to cross the membrane, increasing the barrier function.

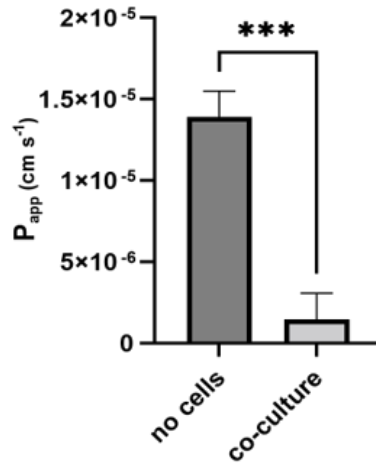


Figure 44. Comparison between apparent permeability (cm/s) of A549 cells and HULEC-5a cells co-cultures and PCL/Gel (no cells) after 7 days at ALI.

4.2.4 Immunofluorescence

For the detection of the expression of E-cadherin (epithelial cadherin), VE-cadherin (vascular endothelial cadherin) and ZO-1, cells were fixated and permeabilized. After blocking unspecific binding sites, the samples were incubated overnight at 4°C with solutions of primary antibodies: ZO-1 antibodies were produced in rabbit, cadherins antibodies were obtained from mouse. To evaluate the expression of Zonula-occludins, goat anti-rabbit antibodies conjugated with Tetramethylrhodamine (TRITC), emitting in red, were used. Goat anti-mouse antibodies conjugated with cyanine were incubated with the samples for the detection of the cadherins.

Confocal laser scanning images show the expression of adherens junctions-forming E-cadherins in A549 cells after 7 days of co-culture at ALI (figure 45, A). E-cadherins appear to be localized along the membrane, between the cells. A549 cells and HULEC-5a cells resulted stained for ZO-1 expression as well, which appears to be more diffused in the cytoplasmic region (figure 45, B, C).

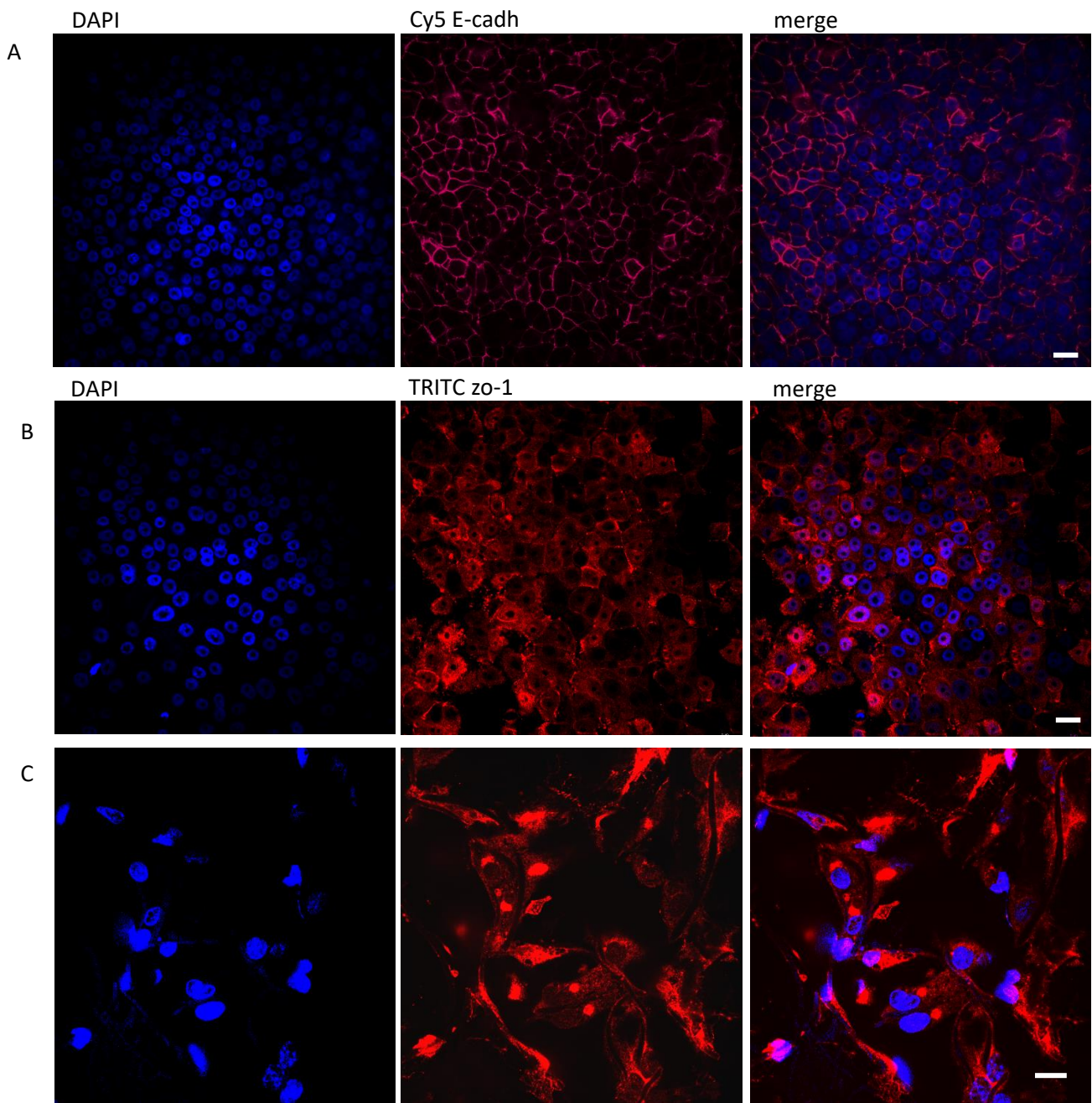


Figure 45. Immunofluorescence staining for E-cadherin in A549 cells (a) and ZO-1 in A549 cells (b) and in HULEC-5a after (c) 7 days at ALI in co-culture. Scale bar is 20 μ m.

5. Conclusions

The alveolar-capillary barrier represents the functional gas-exchange interface between air and blood: its thin and multi-layered structure, constituted by epithelial and endothelial continuum divided by a fibrous basement membrane, contributes to maximize the efficiency of the exchange, while playing its defence barrier role [3] [4]. The respiratory system is indeed constantly exposed to potentially harmful factors that reach the alveoli through the inhaled air, that carries xenobiotics and toxins of the external environment. Alveolar-capillary barrier dysfunctions are associated with diseases like asthma, idiopathic pulmonary fibrosis and COVID-19, characterized by increased epithelial and endothelial alveolar permeability and consequent intra-alveolar haemorrhages [7] [10]. Studying the role and the functions of the alveolar-capillary barrier may help understanding the pathophysiology of diseases and investigating therapeutic targets. For this purpose, the need for reduction and replacement of animal models (due to ethical concerns, high costs and problematic species-specific differences) calls for the advancement of *in vitro* models. Among these, Organs-on-Chip are high-throughput microfluidic devices, where channels that range in size from tens to hundreds of microns allow to process fluids acting primarily as a laminar flow [45]. Thanks to the ability to miniaturize physiological complex processes, mimicking their functionality and biophysical cues at a smaller scale, they allow the use of low volumes of reagents, reducing costs, making the experiments easier to control and increasing the velocity of the responses [45]. In this work, starting from a study performed in the same research group that supervised this thesis project [52], a microfluidic alveolus-on-chip was optimized to host a nanofibrous cellularized membrane, with the aim of recapitulating the characteristics of the alveolar-capillary barrier.

Addressing the issues reported in the cited literature work, the device was designed with lateral inlets and valvular conduits, with the aim of discouraging the phenomenon of liquid level rising above the membrane during air-liquid interface phase. Two sets of serpentines were included to maximize the volume of cell medium that can be stocked in the channels, compensating the absence of endothelial cell medium reservoirs in the upper layers. The CAD models of the masters of the 3 layers constituting the device were designed using Rhinoceros, testing out different possible layouts (Appendix III). The STL

files were printed using a Poly-Jet 3D-printer, that selectively deposits, layer-by-layer, a liquid photopolymer resin that is immediately cured by UV lamps. After a high temperature treatment, PDMS was poured in the molds, that were filled with a solution of pre-polymer and curing agent. The resulting transparent, elastomeric replicas showed the desired microfluidic pattern. The layers were subjected to Plasma-Oxygen treatment, to activate the surfaces and realize the bonding. Before the surface functionalization, a nanofibrous membrane, with a diameter of 5 mm, was placed on the bottom layer, in order to be included between bottom and top layer after the assembly of the two replicas. The membrane was obtained through the electrospinning of a blend solution of 80/20 w/w PCL/gelatin in 50:50 v/v acetic acid and formic acid. The complete device was subjected to microfluidic tests to evaluate the sealing quality, the shape of the inlets and the possibility of implementing the air-liquid interface condition. Before the cellular tests, the final microfluidic platforms were sterilized. The central side-inlet was used to seed HULEC-5a cells in the basal part of the membrane, injecting 10 μL of cell suspension in the culture chamber to obtain a cell density of 16×10^4 cell/cm². After 24 hours, the lateral side-inlet was used to fill the microfluidic channels with HULEC-5a cell medium, and 10 μL of A549 cells suspension were placed on the apical part of the membrane to obtain a cell density of 14×10^4 cell/cm². For 72 hours the co-culture was maintained in submerged condition, and then the A549 cells medium was removed to expose the epithelial layer to air. Performing medium change every 24 hours, the co-culture was interrupted 7 days after ALI implementation. The resulting model was validated through fluorescence imaging, immunostaining and permeability assay. DAPI/phalloidin staining showed that the adopted co-culture protocol allows the cells on both sides of the nanofibrous membrane to reach confluence, showing close cell-cell contact and a spread morphology (figure 42, 43). Immunostaining highlighted the expression of adherens junctions' proteins in the epithelial layer, as well as the expression of ZO-1, fundamental in the formation of tight junctions [66], both in the A549 and HULEC-5a cells after 7 days of co-culture at ALI (figure 45). The expression of these proteins is significant for the evaluation of the barrier function of the model, which should emulate the *in vivo* paracellular transport mechanism and its role in the control of solutes and molecules exchange, controlled by the presence of adherens and tight

junctions. The permeability assay confirmed that the co-cultured membranes are characterized by lower apparent permeability than the acellularized controls (figure 44).

Ultimately, the developed alveolus-on-chip recapitulates some of the major aspects that characterize the physiological alveolar-capillary barrier. The multi-layered structure of the barrier was mimicked co-culturing the electrospun membrane with A549 cells, chosen for their type II alveolar epithelial cells-like phenotype [64], and HULEC-5a cells, for the mimicking of the endothelial layer. The nanofibrous scaffold models the physiological collagen/elastin basement membrane. It was obtained electrospinning a blend solution of PCL and gelatin, as in previous literature works [53] [52], to combine PCL mechanical resistance with the bioactive properties of gelatin [53] [52]. The air-liquid interface that characterizes the physiological barrier, exposed to air in the alveolar lumen and to blood on the other side of the alveolar wall, was implemented in the chip 4 days after the seeding of the HULEC-5a cells, that is 72 hours after the seeding of the A549 cells, removing the epithelial cell medium from the apical side of the device. Air-liquid interface condition was maintained for 7 days. The valvular conduits designed for the bottom layer and the use of the central upper plug allow to reduce the phenomenon of liquid level rising above the membrane, although without constant reproducibility. The device allows to stock endothelial cell medium in its microfluidic channels, providing enough nourishment for 24 hours during the static phase of the cell culture. The design has been optimized to be open to future improving developments. Two types of plugs were designed to set up the device for the mechanical stimulation: sealing the inlets would allow the implementation of a cyclic pressure stimulus over the apical side of the cellularized membrane, mimicking the respiratory cycle that causes, *in vivo*, the iterated expansion and elastic recoil of the alveolar wall. Also, adopting a micro-peristaltic pump, the shear stress caused *in vivo* by the blood stream over the endothelial layer could be reproduced implementing a dynamic flow phase, perfusing the microfluidic channels. The final device supports the application of cell fixation and staining protocols, which require the interruption of the co-culture at the established time point. An alternative method is represented by the evaluation of the transepithelial electrical resistance (TEER), a real time non-invasive technique used in literature [67] to evaluate barrier integrity, based on the use of excitation signals and current measurement through a pair of electrodes placed in the apical and basal compartments. The barrier model could be

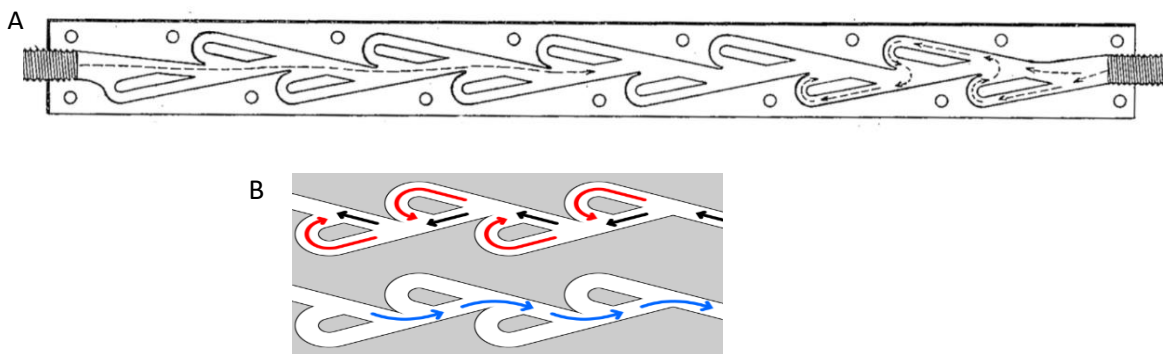
improved including a thin layer of collagen and fibroblasts between the endothelial and epithelial layers, to mimic the interstitial space of the physiological alveolus. The optimization of the culture protocols could allow the replacement of cell lines with primary cells, a powerful resource for the ambitious goal of personalized medicine. Ultimately, the alveolus-on-chip could be included in a body-on-chip system, where the common cell medium circuit allows the involved organs-on-chip to be interconnected and influence each other's responses, modelling the *in vivo* mechanism of constant crosstalk between the physiological systems.

6. Appendix

This section comprises additional figures and schemes that support the information and the comments reported in the previous chapters.

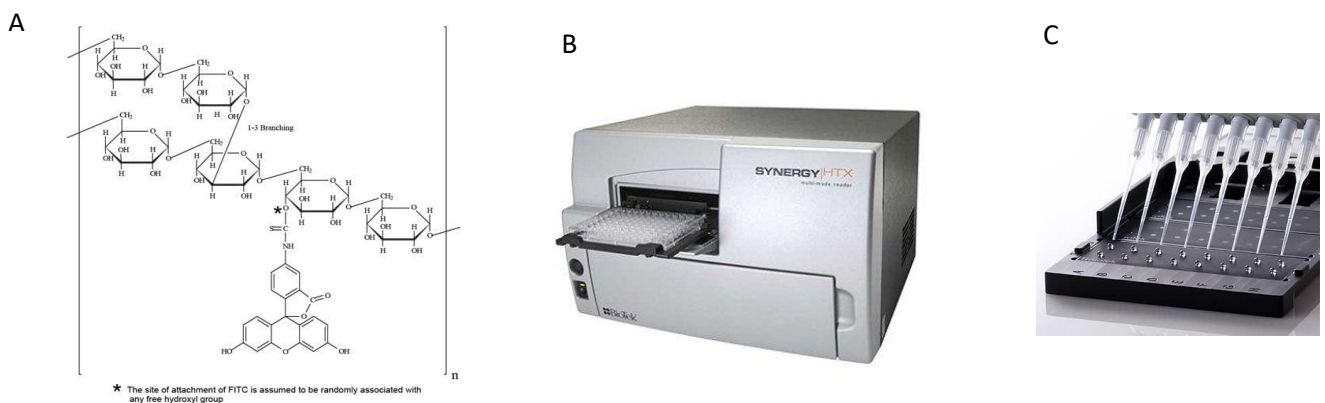
Appendix I

a) Schematic representation of Tesla's patented 'valvular conduit' and (b) its functioning principle: when following the reverse direction (right to left), the flow divides and enters the lateral convoluted channels, opposing its own advancement. The forward direction (left to right) allows fluids to flow 2 to 4 times faster [55] thanks to the central unimpeded corridor. The net result is an asymmetric behaviour in terms of fluidic resistance.



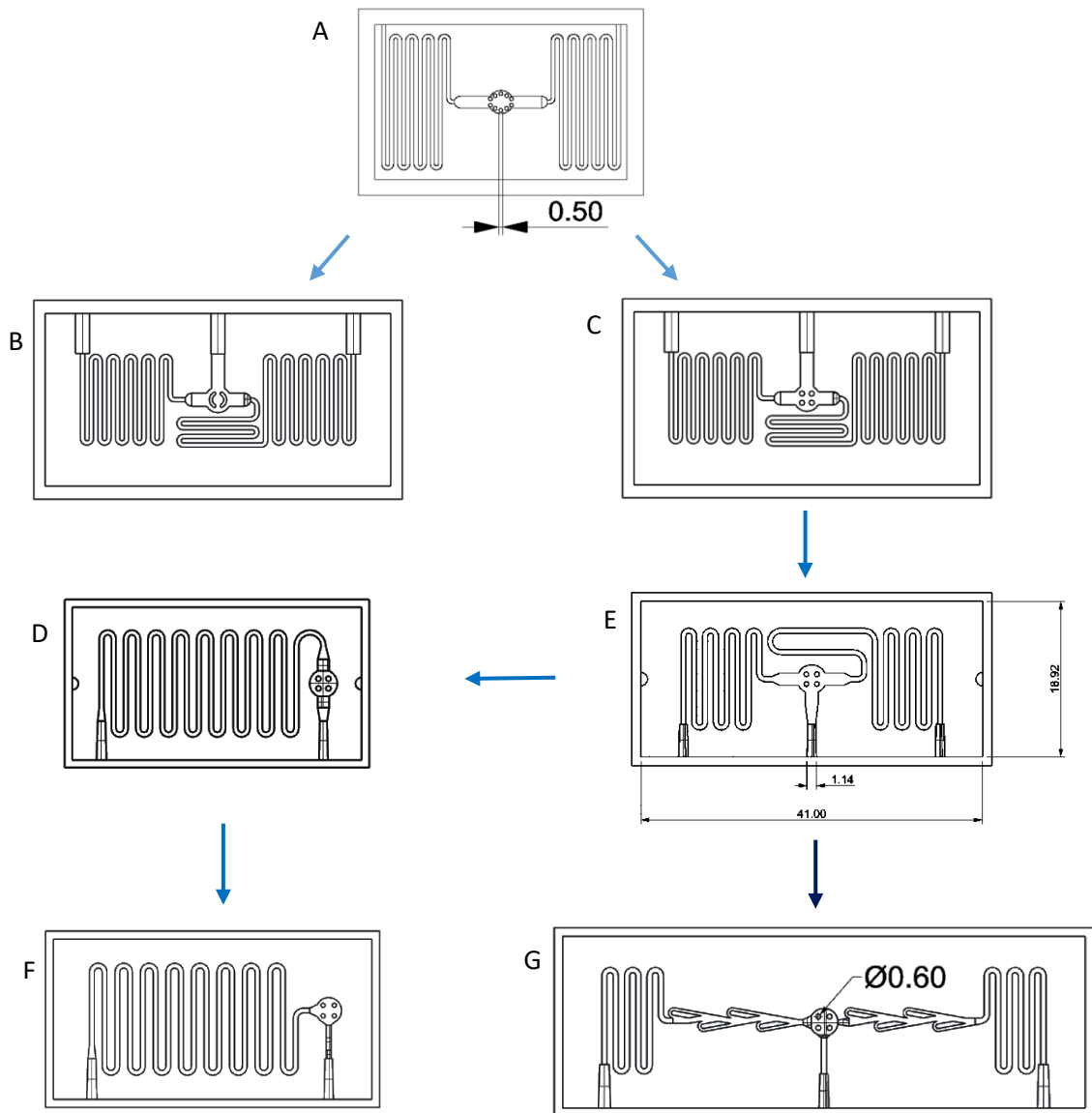
Appendix II

a) Molecular structure of FITC-dextran. b) BioMedLAB multimode plate reader and c) the plate used for the permeability test.



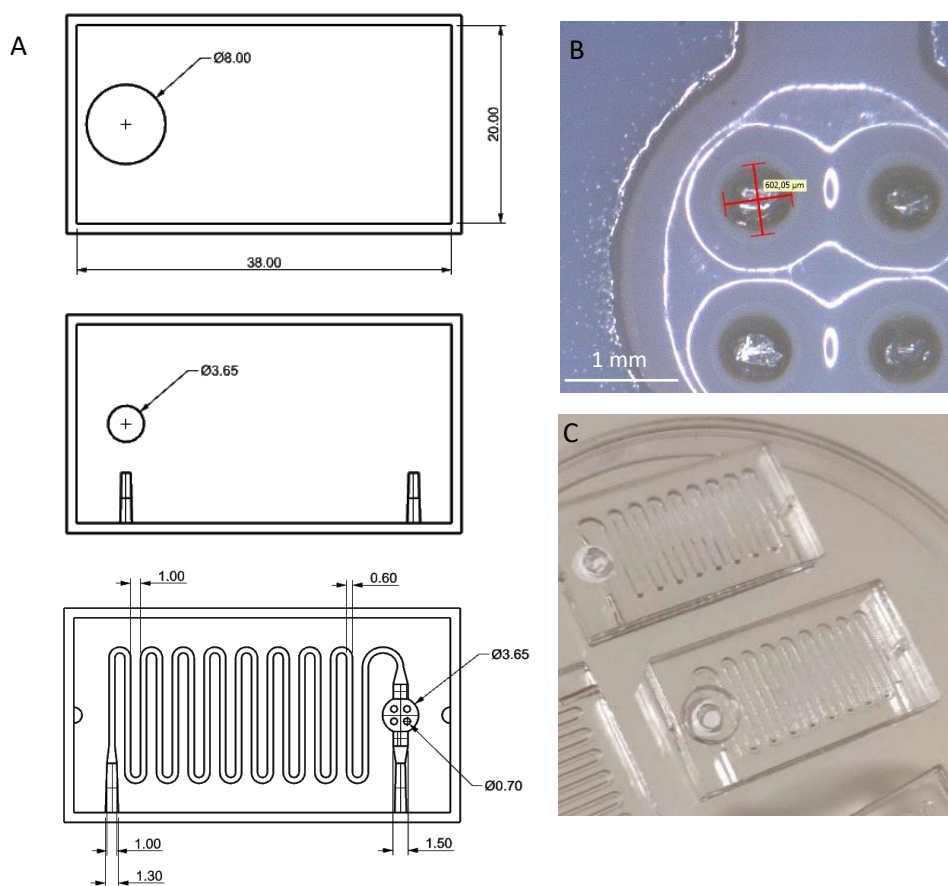
Appendix III

Design evolution of the master of the bottom layer, from the first layout (A) to the definitive version (G).



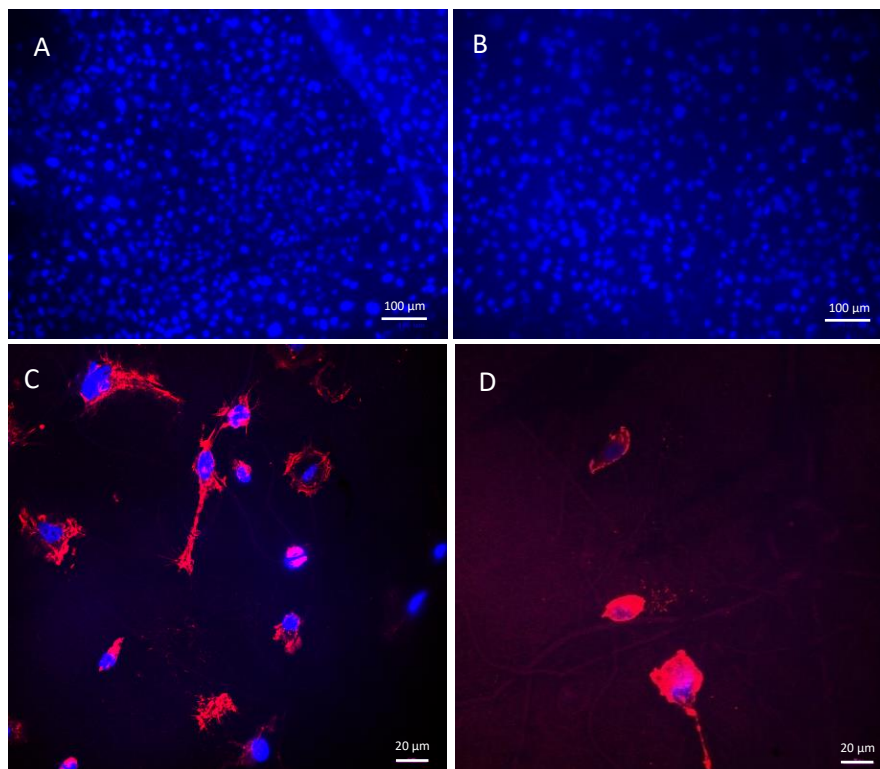
Appendix IV

A) CAD model of the one-serpentine-device's master (from the top: reservoir, top layer and bottom layer), with nominal diameter of the culture chamber's holes in the bottom layer of $700\ \mu\text{m}$ and culture chamber's depth of $1\ \text{mm}$. The length unit of the dimensions is the millimetre. B) Microscopy image of the culture chamber of the bottom layer's mold resulting from the 3D printing of the design in A). C) Two complete PDMS devices in a petri dish.



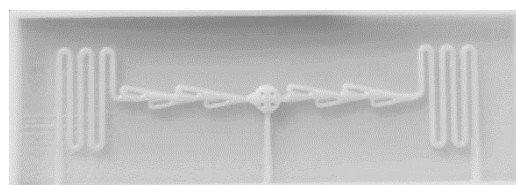
Appendix V

A, B) Microscopy images of the endothelial cells on the lower part of a membrane collected from the devices in Appendix IV, 72 hours after seeding, stained with DAPI (blue nuclei). Scale bar is 100 μm . C, D) Confocal microscopy images of the endothelial cells on the lower part of a membrane collected from the devices in Appendix IV, after 10 days of culture, stained with DAPI (blue nuclei) and rhodamine (red cytoskeleton), in a corner (C) and in the central part of the membrane (D). Scale bar is 20 μm .



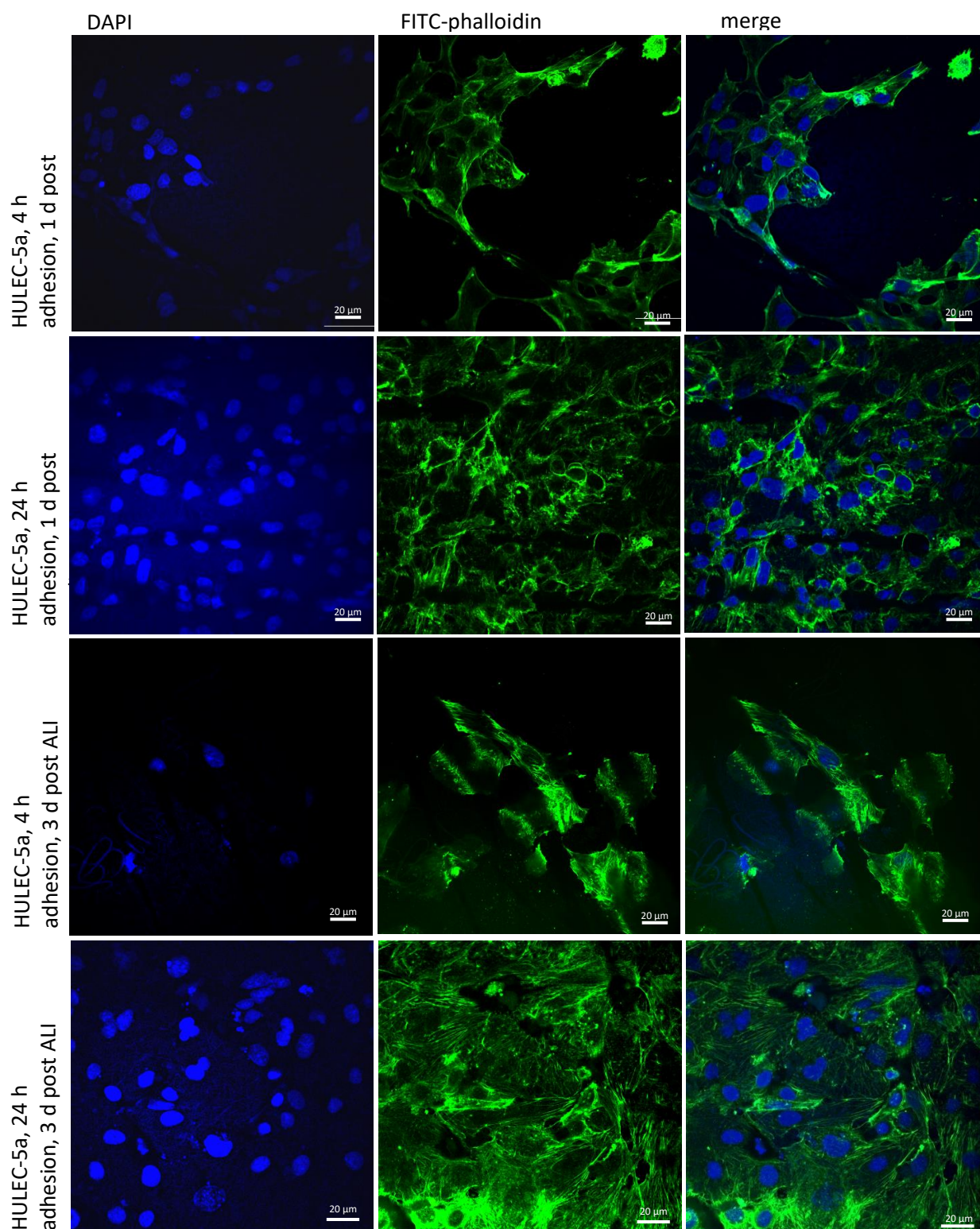
Appendix VI

3D printed mold of the bottom layer of the Tesla valve-design.



Appendix VII

Confocal laser scanning images of HULEC-5a, in Tesla valve-devices, after fixation at different time points and staining with DAPI and phalloidin. The images of both color channels and their merge are shown. Scale bar is 20 μm .



7. Bibliography

- [1] A. Patwa and A. Shah, "Anatomy and physiology of respiratory system relevant to anaesthesia," *Indian Journal of Anaesthesia*, vol. 59, no. 9, 2015, [Online]. Available: https://journals.lww.com/ijaweb/Fulltext/2015/59090/Anatomy_and_physiology_of_respiratory_system.1.aspx
- [2] A. Gillich *et al.*, "Capillary cell-type specialization in the alveolus," *Nature*, vol. 586, no. 7831, pp. 785–789, 2020, doi: 10.1038/s41586-020-2822-7.
- [3] L. Guillot *et al.*, "Alveolar epithelial cells: Master regulators of lung homeostasis," *The International Journal of Biochemistry & Cell Biology*, vol. 45, no. 11, pp. 2568–2573, 2013, doi: <https://doi.org/10.1016/j.biocel.2013.08.009>.
- [4] A. Doryab *et al.*, "Evolution of Bioengineered Lung Models: Recent Advances and Challenges in Tissue Mimicry for Studying the Role of Mechanical Forces in Cell Biology," *Advanced Functional Materials*, vol. 29, no. 39, p. 1903114, Sep. 2019, doi: <https://doi.org/10.1002/adfm.201903114>.
- [5] Tim Taylor, "Respiratory system," Nov. 23, 2020. <https://www.innerbody.com/anatomy/respiratory> (accessed May 03, 2022).
- [6] L. Knudsen and M. Ochs, "The micromechanics of lung alveoli: structure and function of surfactant and tissue components," *Histochemistry and Cell Biology*, vol. 150, no. 6, pp. 661–676, 2018, doi: 10.1007/s00418-018-1747-9.
- [7] E. Dimbath *et al.*, "Implications of microscale lung damage for COVID-19 pulmonary ventilation dynamics: A narrative review," *Life Sciences*, vol. 274, p. 119341, 2021, doi: <https://doi.org/10.1016/j.lfs.2021.119341>.
- [8] N. F. Jufri, A. Mohamedali, A. Avolio, and M. S. Baker, "Mechanical stretch: physiological and pathological implications for human vascular endothelial cells," *Vasc Cell*, vol. 7, p. 8, Sep. 2015, doi: 10.1186/s13221-015-0033-z.
- [9] K. Diem *et al.*, "Mechanical stretch activates piezo1 in caveolae of alveolar type I cells to trigger ATP release and paracrine stimulation of surfactant secretion from alveolar type II cells," *The FASEB Journal*, vol. 34, no. 9, pp. 12785–12804, 2020, doi: <https://doi.org/10.1096/fj.202000613RRR>.
- [10] Z. Nova, H. Skovierova, and A. Calkovska, "Alveolar-Capillary Membrane-Related Pulmonary Cells as a Target in Endotoxin-Induced Acute Lung Injury," *International Journal of Molecular Sciences*, vol. 20, no. 4, 2019, doi: 10.3390/ijms20040831.
- [11] D. M. Smadja *et al.*, "COVID-19 is a systemic vascular hemopathy: insight for mechanistic and clinical aspects," *Angiogenesis*, vol. 24, no. 4, pp. 755–788, 2021, doi: 10.1007/s10456-021-09805-6.
- [12] N. K. Altorki *et al.*, "The lung microenvironment: an important regulator of tumour growth and metastasis," *Nature Reviews Cancer*, vol. 19, no. 1, pp. 9–31, 2019, doi: 10.1038/s41568-018-0081-9.
- [13] D. L. Hickman, J. Johnson, T. H. Vemulapalli, J. R. Crisler, and R. Shepherd, "Commonly Used Animal Models," *Principles of Animal Research for Graduate and Undergraduate Students*, pp. 117–175, 2017, doi: 10.1016/B978-0-12-802151-4.00007-4.
- [14] V. Poli, "'Animal models and their applications in biomedical research', New advances in alternative preclinical trials, PowerPoint presentation," 2020.
- [15] G. Matute-Bello, C. W. Frevert, and T. R. Martin, "Animal models of acute lung injury," *American Journal of Physiology-Lung Cellular and Molecular Physiology*, vol. 295, no. 3, pp. L379–L399, Sep. 2008, doi: 10.1152/ajplung.00010.2008.

- [16] R. Rathnasinghe *et al.*, “Comparison of transgenic and adenovirus hACE2 mouse models for SARS-CoV-2 infection,” *Emerging Microbes & Infections*, vol. 9, no. 1, pp. 2433–2445, Jan. 2020, doi: 10.1080/22221751.2020.1838955.
- [17] S.-H. Sun *et al.*, “A Mouse Model of SARS-CoV-2 Infection and Pathogenesis,” *Cell Host & Microbe*, vol. 28, no. 1, pp. 124–133.e4, Jul. 2020, doi: 10.1016/j.chom.2020.05.020.
- [18] A. Ravizza, “‘3r methods: challenges in bioengineering’, New advances in alternative preclinical trials, PowerPoint presentation,” 2019.
- [19] J. Grune, N. Beyhoff, N. Hegemann, J. H. Lauryn, and W. M. Kuebler, “From bedside to bench: lung ultrasound for the assessment of pulmonary edema in animal models,” *Cell and Tissue Research*, vol. 380, no. 2, pp. 379–392, 2020, doi: 10.1007/s00441-020-03172-2.
- [20] B. L. M. Hogan *et al.*, “Repair and Regeneration of the Respiratory System: Complexity, Plasticity, and Mechanisms of Lung Stem Cell Function,” *Cell Stem Cell*, vol. 15, no. 2, pp. 123–138, Aug. 2014, doi: 10.1016/j.stem.2014.07.012.
- [21] K. Gkatzis, S. Taghizadeh, D. Huh, D. Y. R. Stainier, and S. Bellusci, “Use of three-dimensional organoids and lung-on-a-chip methods to study lung development, regeneration and disease,” *European Respiratory Journal*, vol. 52, no. 5, 2018, doi: 10.1183/13993003.00876-2018.
- [22] A. J. Miller and J. R. Spence, “In Vitro Models to Study Human Lung Development, Disease and Homeostasis,” *Physiology*, vol. 32, no. 3, pp. 246–260, Apr. 2017, doi: 10.1152/physiol.00041.2016.
- [23] D. Gallo, “‘In silico medicine’, New advances in alternative preclinical trials, PowerPoint presentation,” 2020.
- [24] A. v Kolanjiyil and C. Kleinstreuer, “Modeling Airflow and Particle Deposition in a Human Acinar Region,” *Computational and Mathematical Methods in Medicine*, vol. 2019, p. 5952941, 2019, doi: 10.1155/2019/5952941.
- [25] R. Agujetas, R. Barrio-Perotti, C. Ferrera, A. Pandal-Blanco, D. K. Walters, and A. Fernández-Tena, “Construction of a hybrid lung model by combining a real geometry of the upper airways and an idealized geometry of the lower airways,” *Computer Methods and Programs in Biomedicine*, vol. 196, p. 105613, 2020, doi: <https://doi.org/10.1016/j.cmpb.2020.105613>.
- [26] “Modelling and simulation as a transformative tool for medical devices: the transatlantic regulatory landscape.” [Online]. Available: www.avicenna-alliance.com
- [27] N. Heinen, M. Klöhn, E. Steinmann, and S. Pfaender, “In Vitro Lung Models and Their Application to Study SARS-CoV-2 Pathogenesis and Disease,” *Viruses*, vol. 13, no. 5, 2021, doi: 10.3390/v13050792.
- [28] J. Wu *et al.*, “Characterization of air-liquid interface culture of A549 alveolar epithelial cells,” *Brazilian journal of medical and biological research = Revista brasileira de pesquisas medicas e biologicas*, vol. 51, no. 2, pp. e6950–e6950, Dec. 2017, doi: 10.1590/1414-431X20176950.
- [29] S. Upadhyay and L. Palmberg, “Air-Liquid Interface: Relevant In Vitro Models for Investigating Air Pollutant-Induced Pulmonary Toxicity,” *Toxicological Sciences*, vol. 164, no. 1, pp. 21–30, Jul. 2018, doi: 10.1093/toxsci/kfy053.
- [30] T. Pasma *et al.*, “Development of an In Vitro Airway Epithelial–Endothelial Cell Culture Model on a Flexible Porous Poly(Trimethylene Carbonate) Membrane Based on Calu-3 Airway Epithelial Cells and Lung Microvascular Endothelial Cells,” *Membranes (Basel)*, vol. 11, no. 3, 2021, doi: 10.3390/membranes11030197.
- [31] S. Wang Lefeng and Taneja, “Human Alveolar Epithelial Cells Attenuate Pulmonary Microvascular Endothelial Cell Permeability under Septic Conditions,” *PLOS ONE*, vol. 8, no. 2, pp. 1–11, May 2013, doi: 10.1371/journal.pone.0055311.

- [32] S. Kim *et al.*, “Comparison of Cell and Organoid-Level Analysis of Patient-Derived 3D Organoids to Evaluate Tumor Cell Growth Dynamics and Drug Response,” *SLAS Discovery*, vol. 25, no. 7, pp. 744–754, Aug. 2020, doi: 10.1177/2472555220915827.
- [33] J. M. Rozenberg *et al.*, “Biomedical Applications of Non-Small Cell Lung Cancer Spheroids,” *Frontiers in Oncology*, vol. 11, 2021, doi: 10.3389/fonc.2021.791069.
- [34] K. Han *et al.*, “CRISPR screens in cancer spheroids identify 3D growth-specific vulnerabilities,” *Nature*, vol. 580, no. 7801, pp. 136–141, 2020, doi: 10.1038/s41586-020-2099-x.
- [35] Y. Han *et al.*, “Identification of SARS-CoV-2 inhibitors using lung and colonic organoids,” *Nature*, vol. 589, no. 7841, pp. 270–275, 2021, doi: 10.1038/s41586-020-2901-9.
- [36] L. Wang *et al.*, “A human three-dimensional neural-perivascular ‘assembloid’ promotes astrocytic development and enables modeling of SARS-CoV-2 neuropathology,” *Nature Medicine*, vol. 27, no. 9, pp. 1600–1606, 2021, doi: 10.1038/s41591-021-01443-1.
- [37] J.-H. Ng, A. Sun, H. S. Je, and E.-K. Tan, “Unravelling Pathophysiology of Neurological and Psychiatric Complications of COVID-19 Using Brain Organoids,” *The Neuroscientist*, p. 10738584211015136, May 2021, doi: 10.1177/10738584211015136.
- [38] G. Ciardelli, “‘Organ and tumor models’, Frontiers in Bioengineering enabling nanotechnologies, PowerPoint presentation,” 2020.
- [39] M. Barreiro Carpio, M. Dabaghi, J. Ungureanu, M. R. Kolb, J. A. Hirota, and J. M. Moran-Mirabal, “3D Bioprinting Strategies, Challenges, and Opportunities to Model the Lung Tissue Microenvironment and Its Function,” *Frontiers in Bioengineering and Biotechnology*, vol. 9, 2021, doi: 10.3389/fbioe.2021.773511.
- [40] P. Jain *et al.*, “Reconstruction of Ultra-thin Alveolar-capillary Basement Membrane Mimics,” *Advanced Biology*, vol. 5, no. 8, p. 2000427, 2021, doi: <https://doi.org/10.1002/adbi.202000427>.
- [41] D. Dhamecha, D. Le, R. Movsas, A. Gonsalves, and J. U. Menon, “Porous Polymeric Microspheres With Controllable Pore Diameters for Tissue Engineered Lung Tumor Model Development,” *Frontiers in Bioengineering and Biotechnology*, vol. 8, 2020, doi: 10.3389/fbioe.2020.00799.
- [42] S. E. Gilpin and D. E. Wagner, “Acellular human lung scaffolds to model lung disease and tissue regeneration,” *European Respiratory Review*, vol. 27, no. 148, 2018, doi: 10.1183/16000617.0021-2018.
- [43] M. E. Scarritt *et al.*, “Re-endothelialization of rat lung scaffolds through passive, gravity-driven seeding of segment-specific pulmonary endothelial cells,” *Journal of Tissue Engineering and Regenerative Medicine*, vol. 12, no. 2, pp. e786–e806, 2018, doi: <https://doi.org/10.1002/term.2382>.
- [44] D. Kang *et al.*, “All-Inkjet-Printed 3D Alveolar Barrier Model with Physiologically Relevant Microarchitecture,” *Advanced Science*, vol. 8, no. 10, May 2021, doi: 10.1002/advs.202004990.
- [45] C. Ma, Y. Peng, H. Li, and W. Chen, “Organ-on-a-Chip: A New Paradigm for Drug Development,” *Trends in Pharmacological Sciences*, vol. 42, no. 2, pp. 119–133, Feb. 2021, doi: 10.1016/j.tips.2020.11.009.
- [46] Q. Wu *et al.*, “Organ-on-a-chip: recent breakthroughs and future prospects,” *BioMedical Engineering OnLine*, vol. 19, no. 1, p. 9, 2020, doi: 10.1186/s12938-020-0752-0.
- [47] A. Skardal *et al.*, “Multi-tissue interactions in an integrated three-tissue organ-on-a-chip platform,” *Scientific Reports*, vol. 7, no. 1, p. 8837, 2017, doi: 10.1038/s41598-017-08879-x.
- [48] M. Zhang *et al.*, “Biomimetic Human Disease Model of SARS-CoV-2 Induced Lung Injury and Immune Responses on Organ Chip System,” *Advanced science (Weinheim, Baden-Wuerttemberg, Germany)*, vol. 8, no. 3, p. 2002928, Oct. 2020, doi: 10.1002/advs.202002928.

- [49] J. D. Stucki *et al.*, “Medium throughput breathing human primary cell alveolus-on-chip model,” *Scientific Reports*, vol. 8, no. 1, p. 14359, 2018, doi: 10.1038/s41598-018-32523-x.
- [50] D. Huh, B. D. Matthews, A. Mammoto, M. Montoya-Zavala, H. Y. Hsin, and D. E. Ingber, “Reconstituting Organ-Level Lung Functions on a Chip,” *Science (1979)*, vol. 328, no. 5986, pp. 1662–1668, 2010, doi: 10.1126/science.1188302.
- [51] M. Radiom, Y. He, J. Peng-Wang, A. Baeza-Squiban, J.-F. Berret, and Y. Chen, “Alveolar mimics with periodic strain and its effect on the cell layer formation,” *Biotechnology and Bioengineering*, vol. 117, no. 9, pp. 2827–2841, 2020, doi: <https://doi.org/10.1002/bit.27458>.
- [52] Eleonora Palumbo, “The alveolus-on-a-chip: a biomimetic, microfluidic in vitro model of the alveolar-capillary barrier,” Politecnico di Torino, Torino, 2021.
- [53] N. Higueta-Castro *et al.*, “Using a Novel Microfabricated Model of the Alveolar-Capillary Barrier to Investigate the Effect of Matrix Structure on Atelectrauma,” *Sci Rep*, vol. 7, no. 1, p. 11623, Sep. 2017, doi: 10.1038/s41598-017-12044-9.
- [54] Nikola Tesla, “Valvular conduit” 1,329,559, 1920
- [55] Q. M. Nguyen, J. Abouezzi, and L. Ristroph, “Early turbulence and pulsatile flows enhance diodicity of Tesla’s macrofluidic valve,” *Nature Communications*, vol. 12, no. 1, p. 2884, 2021, doi: 10.1038/s41467-021-23009-y.
- [56] M.-B. Habhab, T. Ismail, and J. F. Lo, “A Laminar Flow-Based Microfluidic Tesla Pump via Lithography Enabled 3D Printing,” *Sensors*, vol. 16, no. 11, 2016, doi: 10.3390/s16111970.
- [57] C.-C. Hong, J.-W. Choi, and C. H. Ahn, “A novel in-plane passive microfluidic mixer with modified Tesla structures,” *Lab Chip*, vol. 4, no. 2, pp. 109–113, 2004, doi: 10.1039/B305892A.
- [58] M. Attaran, “The rise of 3-D printing: The advantages of additive manufacturing over traditional manufacturing,” *Business Horizons*, vol. 60, no. 5, pp. 677–688, 2017, doi: <https://doi.org/10.1016/j.bushor.2017.05.011>.
- [59] N. Vidakis, M. Petousis, N. Vaxevanidis, and J. Kechagias, “Surface Roughness Investigation of Poly-Jet 3D Printing,” *Mathematics*, vol. 8, no. 10, 2020, doi: 10.3390/math8101758.
- [60] Stratasys, “Desktop 3D printer PolyJet Objet30.” <https://www.stratasys.com/it/3d-printers/objet30> (accessed May 17, 2022).
- [61] B. Venzac *et al.*, “PDMS Curing Inhibition on 3D-Printed Molds: Why? Also, How to Avoid It?,” *Analytical Chemistry*, vol. 93, no. 19, pp. 7180–7187, May 2021, doi: 10.1021/acs.analchem.0c04944.
- [62] G. Giuntoli *et al.*, “In-vitro Characterization of a Hernia Mesh Featuring a Nanostructured Coating,” *Frontiers in Bioengineering and Biotechnology*, vol. 8, 2021, doi: 10.3389/fbioe.2020.589223.
- [63] A. Borók, K. Laboda, and A. Bonyár, “PDMS Bonding Technologies for Microfluidic Applications: A Review,” *Biosensors (Basel)*, vol. 11, no. 8, p. 292, Aug. 2021, doi: 10.3390/bios11080292.
- [64] K. A. Foster, C. G. Oster, M. M. Mayer, M. L. Avery, and K. L. Audus, “Characterization of the A549 Cell Line as a Type II Pulmonary Epithelial Cell Model for Drug Metabolism,” *Experimental Cell Research*, vol. 243, no. 2, pp. 359–366, 1998, doi: <https://doi.org/10.1006/excr.1998.4172>.
- [65] Merck KGaA, “L-Glutamine in Cell Culture,” 2022. <https://www.sigmaaldrich.com/IT/it/technical-documents/technical-article/cell-culture-and-cell-culture-analysis/mammalian-cell-culture/glutamine> (accessed May 17, 2022).
- [66] A. Hartsock and W. J. Nelson, “Adherens and tight junctions: Structure, function and connections to the actin cytoskeleton,” *Biochimica et Biophysica Acta (BBA) - Biomembranes*, vol. 1778, no. 3, pp. 660–669, 2008, doi: <https://doi.org/10.1016/j.bbamem.2007.07.012>.

- [67] B. Srinivasan, A. R. Kolli, M. B. Esch, H. E. Abaci, M. L. Shuler, and J. J. Hickman, "TEER Measurement Techniques for In Vitro Barrier Model Systems," *Journal of Laboratory Automation*, vol. 20, no. 2, pp. 107–126, Jan. 2015, doi: 10.1177/2211068214561025.
- [68] S. M. Moghadam *et al.*, "Electrospinning: Current Status and Future Trends," 2016, pp. 89–154. doi: 10.1007/978-3-319-39715-3_4.